Max-Planck-Institut für Plasmaphysik

Validation of theory based transport models in tokamak plasmas

Giovanni Tardini

Technische Universität München

2003

Technische Universität München

Validation of theory based transport models in tokamak plasmas

Giovanni Tardini

Vollständiger Abdruck der von der Fakultät für Physik der Technischen Universität München zur Erlangung des akademischen Grades eines Doktors der Naturwissenschaften (Dr. rer. nat.) genehmigten Dissertation.

Vorsitzender:	Univ.-Prof. Ph. D. F. Koch
Prüfer der Dissertation:	1. Hon.-Prof. Dr. R. Wilhelm
	2. Univ.-Prof. Dr. H. Friedrich

Die Dissertation wurde am 19. 02. 2003 bei der Technischen Universität München eingereicht und durch die Fakultät für Physik am 27. 05. 03 angenommen.

Abstract

Heat transport in tokamaks is several orders of magnitude higher than predicted by the collisional theory. A physical understanding of the phenomena limiting energy confinement is a basic requirement in order to make reliable predictions about the fusion gain of the future tokamak reactor ITER and to investigate new scenarios and plasma regimes.

Since decades anomalous transport has been addressed by means of empirical and semi-empirical models. The theoretical research assumes that micro-instabilities driven by plasma turbulence are responsible for the confinement degradation, but the full simulations with the comprehensive theoretical codes require far too long computing time to afford a validation against an extensive experimental database.
Only in the early nineties one dimensional, theory based models have been developed, relying on the fluid approach. These models allow comparisons with the experimental results without any *ad hoc* adjustment of empirical fitting parameters and, on the other hand, without too long computing time.

In the present work the most commonly accepted models are validated against a large database of selected ASDEX Upgrade discharges. Important results from JET, the largest tokamak built so far, are included as well, to test the models on a different sized device and to increase confidence in transport predictions and in extrapolations to ITER.

As a result of the systematic comparison with the available data, qualitative as well as quantitative evaluations of the predicting capability of the models are presented. A physics interpretation of the heat transport phenomenology in the conventional scenario is proposed and discussed.

Danksagung

Ich möchte mich zuerst bei Prof. Wilhelm für seine akademische Betreuung bedanken.
Mein Dank gilt vor allem an Dr. Arthur Peeters, dessen Zusammenarbeit stets wertvoll und ermutigend gewesen ist. Unsere *Transport analysis* Gruppe hat nicht nur eine bekanntlich *einfache Struktur*, sondern auch ein schön umgängliches Arbeitsklima. Physik zu lernen, zur Fusionsforscung beizutragen und dabei noch Spass zu haben ist bei mir Grund der Dankbarkeit.
Ich danke Dr. Grigory Pereverzev, der den grossen Verdienst hat, den ASTRA Code geschrieben zu haben und immer wieder zu aktualisieren. Seine Hilfsbereitschaft bei den vielen meinen Fragen und ASTRA-Wünschen ist beeindruckend. Danke für das "physikalischste" IPP-Kolloquium, das ich bisher gehört habe.
Der Austausch mit Dr. Clemente Angioni war besonders hilfsreich. Von ihm habe ich gelernt, wie weit man eine "black box" aufmachen und untersuchen kann. Es ist viel interessanter, eine Forschung zu zweit zu verfolgen.
Der ganzen Tokamakabteilung danke ich herzlich für die Gesellschaft und die interessanten physikalischen Diskussionen. Prof. Lackner hat wesentlich zu meiner Entscheidung für diese Themenstellung beigetragen.
Besonders verpflichtet fühle ich mich Herrn Dr. Francois Ryter: ohne ihn würden die bedeutsamsten experimentellen Befunde für meine Doktorarbeit nicht existieren. Diese Zusammenarbeit mit alten Wurzeln und immer fruchtbarem Meinungsaustausch ist im Rahmen der unofiziellen Task-Force "GME" (Gemeinsam MittagEssen) zustandegekommen.
An dieser Stelle muss ich mich noch bei den übrigen "GME"-Mitgliedern bedanken, für die gemütliche Unterhaltung und die physikalische Bereicherung: Dr. Emanuele Poli, Dr. Fritz Leuterer, Stefano Riondato, Dr. Dietmar Wagner, Dr. Adriano Manini und Dr. Krassimir Kirov.
Das ganze ASDEX Upgrade TEAM verdient mehr als ein Dankwort für die Durchführung der Experimente sowie für die sorgfältige Diagnostikverwaltung, durch die mir umfangreiche Daten zur Verfügung gestellt wurden. Die Theorie ist zwar nicht grau, wie man sie bezeichnet, aber erst ein stetiger Vergleich mit dem Experiment verleiht ihr Bestand und Zuverlässigkeit.
Zum Schluss möchte ich mich bei allen Freunden bedanken, denn ohne Freundschaft überlebe ich keine drei Wochen, umsoweniger drei Jahre.
Die grösste Dankbarkeit gilt Lucia, meiner Frau, die die Laune und die Witze eines Physikers schon lange erträgt. Durch ihre Gegenwart werde ich immer wieder in der Wirklichkeit festgehalten.

Zusammenfassung

Die Kernfusion ist eine viel versprechende Lösung für den weltweit steigenden Energiebedarf, die die Umwelt weniger belastet und im Vergleich zu Kernspaltung ein deutlich geringeres radiologisches Problem darstellt. Die Reaktion erfolgt sich durch die Verschmelzung zwei leichter Nuklide zu einem schwereren Atomkern. Der Massendefekt sorgt um Energiegewinn, aber die Coulomb-Barriere zwischen den positiv geladenen Nukliden muss erst überwunden werden. Die für einen Reaktor notwendige Fusionsrate ist durch hohe Temperatur und Teilchendichte bedingt; bei den in Frage kommenden Temperaturen ist die Materie voll ionisiert und befindet sich somit im Plasmazustand.
Die erfolgreichste Anlage für den Einschluss hochenergetischer geladener Teilchen ist der Tokamak, der das Plasma in einer günstigen Magnetfeldkonfiguration einschliesst. Trotzdem sind Energieverluste mehrere Grösseordnungen höher als die kollisionale Theorie vorhersagt. In Hinblick auf einen Fusionsreaktor ist das Verständnis der den Energieinschluss begrenzenden Phänomene eine unabdingbare Voraussetzung, die seit Jahrzehnten die Fusionsforschung mit höchstem Vorrang beschäftigt. Eine bessere thermische Isolierung würde zu einem kleineren Tokamakreaktor mit dem gleichen Fusionsgewinn führen, was bedeutende technische und ökonomische Vorteile mit sich bringen würde.
Jahrzehntelang hat man den Wärmetransport in Tokamaks mittels empirischer bzw. halbempirischer Modelle interpretiert. Das hat immer wieder neue Experimente stimuliert. Dennoch kann eine physikalische Erklärung der beobachteten Transporteigenschaften auf dieser Weise nur nahegelegt, nicht bewiesen werden, weil viele unterschiedliche Ansätze zum gleichen Ergebnis führen. Insbesondere sind die Vorhersagen für einen künftigen Tokamak oder für ein neues Szenario nur dann zuverlässig, wenn ein Modell kein *ad hoc* Parameter enthält, das sich zugunsten der neuen experimentellen Situation eichen lässt. Die Extrapolationen für den "International Tokamak Experimental Reactor" (ITER) gewinnen weder eine Bestätigung noch eine vertauenswürdige Korrektur von solchen empirischen Modellen.
Seit etwa 30 Jahren geht die theoretische Forschung davon aus, dass Mikroinstäbilitäten im Plasma für den anomalen Wärmetransport verantwortlich sind, indem sie Turbulenz erzeugen, die eine Wellenlänge im Bereich des Gyrationsradius der Ionen um das Magnetfeld besitzt. Aber erst die Entwicklung von vereinfachten, aber theoretisch begründeten 1D-Modellen hat es Anfang der 90er Jahre ermöglicht, einen quantitativen Vergleich zwischen Experimenten und theoretischen Vorhersagen ohne jegliche Anpassung an die experimentellen Befunde und ohne zu lange Rechenzeit durchzuführen. Diese Möglichkeit wurde jedoch bisher nur begrenzt genutzt.
Ziel dieser Dissertation ist, mit Hilfe der umfangreichen ASDEX Upgrade Datenbasis und ducrh Einbeziehung wichtiger Ergebnisse von der weltweit grössten Tokamakanlage "Joint European Torus" (JET) zu einer systematischen Validierung der existierenden thereotis-

chen Transportmodelle zu gelangen. Als Ergebnis der Arbeit wurden wichtige Erkentnisse zum anomalen Transport erzielt, die zur Fusionsforschung insbesondere in Hinblick auf einen künftigen Tokamakreaktor wesentlich voranbringen könnten.
Dazu wurde eine umfassende und gezielte Datenbank zusammengestellt, die es erlaubt, die Eigenschaften der Modelle im Detail zu überprüfen. Durch Hinzunahme von Entladungen mit "verbessertem Randeinschluss" (H-mode) im sogenannten "konventionellen Szenario", sowie über Experimente mit vorwiegender Elektronenheizung (über Hochfrequenzverfahren) andererseits werden getrennte Aussagen über Ionen- und Elektronenwärmetransport möglich.
Für die genauere Analyse wurden die Modelle in einen flexiblen Transport Code eingebaut und auf die ausgewählten Entladungen angewandt. Analysismitteln zur qualitativen sowie quantitativen Auswertung der Vorhersagefähigkeit der jeweiligen Modelle sind eingeführt. Somit ergänzen sich verschiedene Beiträge zum Verständnis vom anomalen Transport.
Die Begrenzungen der Anwendbarkeit der Modelle werden vorgestellt und die Hauptabhängigkeiten hervorgehoben. Die physikalischen Effekte, welche durch die Variation von wichtigen Plasmaparametern zustandekommen, sind sorgfältig durch gezielte *Parameter scans* untersucht.
Im Ergebnis führt dieser systematische Vergleich zwischen Theorie und Experiment zu wichtigen Aussagen in Bezug auf Ionen- sowie Elektronenwärmetransport. Die physikalischen Annahmen der Modelle werden anhand der experimentellen Ergebnisse beurteilt. Die resultierenden Schlussfolgerungen auf die den Transport erhöhendenden Turbulenzphänomene werden aufgeführt und im Detail diskutiert. Insbesondere stellt sich die durch den Ionentemperaturgradienten getriebene Mode als die dominierende Instabilität für den vergleichsweise starken Ionentransport in H-mode Entladungen heraus. Die Kombination dieser Mode mit der für den Elektronentransport massgebenden "Trapped Electron Mode" (durch gefangene Elektronen verursachte Instabilität) erklärt ohne weitere Annahmen die ganze Vielfalt der experimentellen Ergebnisse. Beide Turbulenzphänomenen zusammengenommen geben eine Zuverlässige Interpretation für den anomalen Wärmetransport in Tokamaks.

Io veggio ben, che giammai non si sazia
nostro intelletto, se 'l ver non lo illustra,
di fuor dal qual nessun vero si spazia.
Posasi in esso come fera in lustra
tosto che giunto l'ha, e giugner pollo,
se non, ogni disio sarebbe frustra;
nasce per quello, a guisa di rampollo,
a pié del vero il dubbio, ed è natura
ch'al sommo pinge noi di collo in collo.

(Dante, Commedia, Paradiso IV, vv. 124-132)

Well I perceive that never sated is
Our intellect unless the Truth illume it,
Beyond which nothing true expands itself.
It rests therein, as wild beast in his lair,
When it attains it;and it can attain it;
If not, then each desire would frustrate be.
Therefore springs up, in fashion of a shoot,
Doubt at the foot of truth; and this is nature,
Which to the top from height to height impels us

Contents

Chapter 1

Introduction

The paradox is only a conflict between reality and your feeling of what reality ought to be (R. Feynmann)

1.1 Controlled thermonuclear fusion

The increasing worldwide energy demand stimulates the development of alternative energy sources. Most power plants nowadays produce electricity by burning gasoline and carbon but, whereas the amount of fossil fuel is expected to cover the energy needs for the intermediate time, serious questions have been raised about the impact on the ecosystem and the climate.
Nuclear power as well as renewable energy sources are seen as valid alternatives for a long term strategy. Energy can be gained from the mass loss after a nuclear reaction, such as the splitting of a heavy nucleus into two lighter ones, or the fusion of hydrogen isotopes to give helium. Nuclear fission is developed enough to deliver already a significant amount of energy in the industrialised countries. However, radioactive waste with an extremely long lifetime cannot be avoided, and its safe storing is a major concern today. Besides, fission reactors work near criticality, which can be prevented only by means of an artificial regulation. Nuclear fusion would have also waste, since the inner walls of a reactor would be activated by neutrons. However, a substantial improvement is achieved by the choice of appropriate wall and structure materials of low activation. In addition, an accident would not trigger an uncontrolled energy emission, because the fusion reactor contains only a little amount of fuel.
To produce energy through thermonuclear controlled fusion is still a challenging goal. The main hurdle on the way towards an economically attractive fusion power plant is the very low cross section of the reaction, due to the Coulombian barrier between charged nuclei. To overcome this inhibition it is necessary to increase the average kinetic energy

of the reacting nuclei up to values of several keV (see Fig. 1.1). A kinetic energy of 1 keV

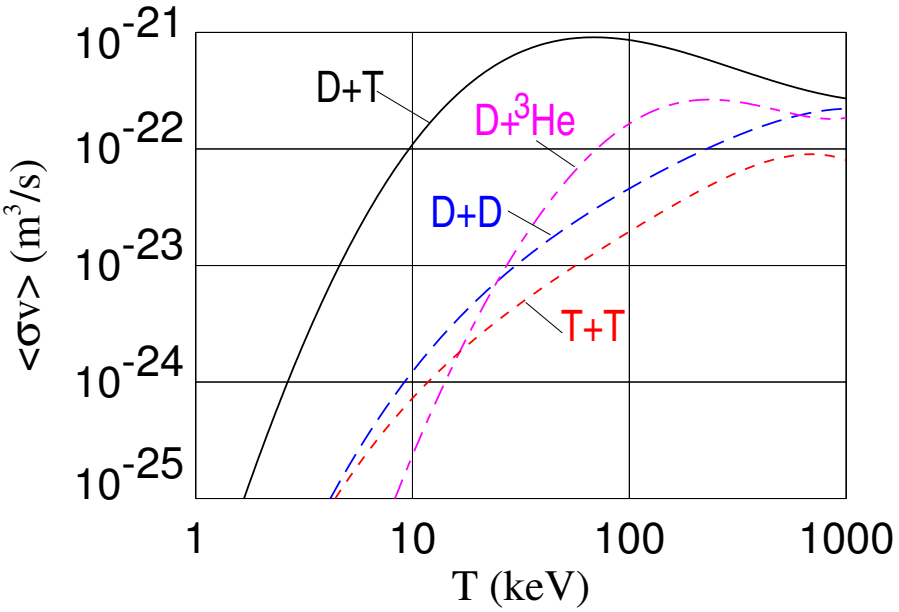

Figure 1.1: Reaction parameter $< \sigma v >$ as a function of T_i for different fusion reactions

corresponds roughly to a temperature of 10 millions K. At such temperatures matter is fully ionised and the mixture of electrons and ions is called plasma. On earth, the most feasible fusion reactions are listed in Table 1.1.

For temperatures below 500 keV the D-T reaction exhibits the highest cross section

$$\begin{gathered}
\mathrm{D} + \mathrm{D} \rightarrow \mathrm{n}\ (2.45\ \mathrm{MeV}) + {}^3\mathrm{He}\ (0.82\ \mathrm{MeV})\ [50\ \%] \\
\mathrm{D} + \mathrm{D} \rightarrow \mathrm{p}\ (3.02\ \mathrm{MeV}) + \mathrm{T}\ (1.01\ \mathrm{MeV})\ [50\ \%] \\
\mathrm{D} + \mathrm{T} \rightarrow \mathrm{n}\ (14.04\ \mathrm{MeV}) + {}^4\mathrm{He}\ \ (3.54\ \mathrm{MeV}) \\
\mathrm{D} + {}^3\mathrm{He} \rightarrow \mathrm{p}\ (14.64\ \mathrm{MeV}) + {}^4\mathrm{He}\ (3.71\ \mathrm{MeV})
\end{gathered}$$

Table 1.1: Most relevant fusion reactions with deuterium. The particle energy after the reaction is reported in the round brackets.

and a very good energy production rate (17 MeV per reaction). Therefore, it is the best candidate for a fusion reactor, in spite of the unavailability of tritium in nature. The later problem can be solved using the neutrons produced in the D-T reaction. Surrounding the plasma with Lithium, a second reaction can produce Tritium which can be gathered and used for plasma fuelling. The D-T reaction rate starts to be relevant at particle energies

of 10 keV or more. The aim is to have a self-sustained reaction, where the fusion energy is enough to induce the next reactions, compensating the heat losses due to radiation and transport phenomena: this condition is called ignition in the literature.
Fusion is the energy source of all stars. In this case, the confinement of the plasma is ensured by the gravitational force. To obtain ignition on earth, two approaches have been developed: "inertial fusion" creates very dense plasmas for a short time, "magnetic fusion" confines a relatively rarefied, hot plasma for a long time through the use of a magnetic field.
In the present fusion experiments ignition has not yet been reached: it is necessary to supply power to obtain the desired high temperature. One of the main problems is the relatively fast transport of the heat out of the plasma. The most successful configuration for magnetic plasma confinement is the Tokamak, realised for the first time by L. Artsimovich in 1952. The name comes from the Russian acronym *TOroidalnaya KAmera MAgnitnymi Katushkami*, toroidal chamber with magnetic coils. The tokamak configuration is illustrated in Fig. 1.2. The dominant magnetic field component is the toroidal one, produced by external coils. A poloidal field is created mainly by a transformer induced toroidal current in the plasma, with varying contribution from non inductive current drive. This ensures the plasma equilibrium and improves confinement. The current induced is at the same time a tool to ionise the gas generating the plasma through ohmic heating. The resulting field lines in the ideal tokamak configuration are helical and lie on nested toroidal magnetic surfaces (see Fig. 1.2); the safety factor $q(r)$ is a measure of the number of toroidal windings of a field line required to complete one poloidal loop on a given cross section.

1.2 Transport in tokamaks

One of the main problems in fusion research is the understanding of the mechanisms governing heat transport in the direction perpendicular to the magnetic surfaces. A better energy confinement would allow for the same fusion gain in a smaller sized reactor, with all the economical and technical benefits which this implies. In particular, it is expensive to supply a strong enough magnetic field over a large volume; besides, the mechanical stresses due to a sudden loss of the plasma caused by instabilities increase with growing machine size. A large device is also less flexible, leading for instance to long shutdowns to substitute a component of the reactor.

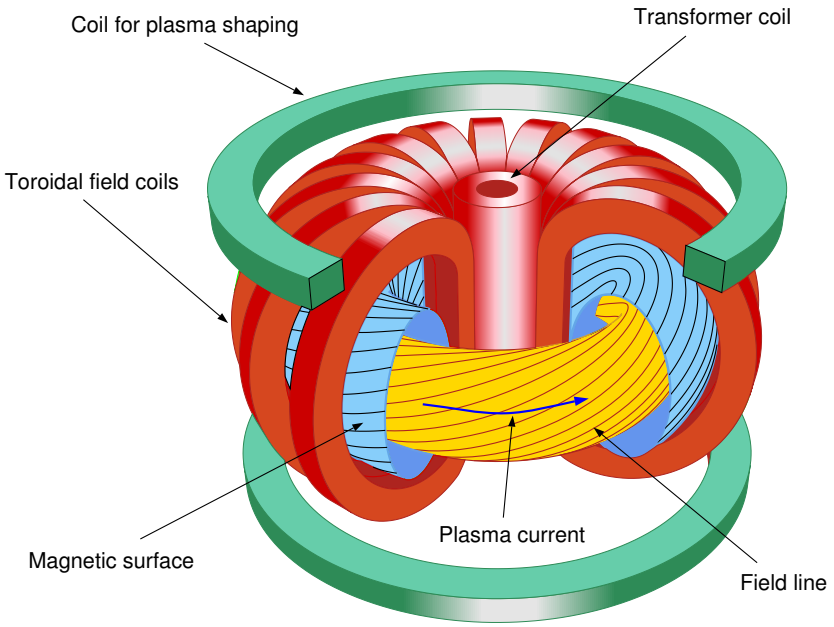

Figure 1.2: Tokamak configuration: the innermost cylinder is the transformer coil to induce the toroidal current and thus the poloidal magnetic field. The ring of D-shaped coils creates the toroidal magnetic field. The resulting field lines run helicoidally on the nested toroidal surfaces. The two horizontal coils generate a vertical field for the radial plasma equilibrium as well as for plasma shaping.

1.2.1 Confinement and ignition

The thermal energy stored in a plasma (see [1]) is

$$W = \frac{3}{2} \int_V k_B \left(n_e T_e + n_i T_i \right) dV \ ,$$

where the labels refer to electrons and ions, n_j and T_j represent the particle density and temperature, respectively. In the following, the Boltzmann constant k_B will be omitted for simplicity. In the steady state, the energy losses P_{out} are equal to the input power P_{in}, supplied by different heating mechanisms. A measure of the thermal isolation capability of a plasma is its confinement time τ_E, which corresponds to the heat recycling rate:

$$\tau_E = \frac{W}{P_{out}} \ .$$

The reaction rate is proportional to the plasma density, and the so called *triple product* $n_e T_i \tau_E$ is a figure of merit for the fusion efficiency; it has been shown [1] that ignition is reached when the following relation is fulfilled:

$$n_e T_i \tau_E > 3 \times 10^{21} \text{ m}^{-3} \text{ keV s} \quad .$$

Without loss of generality we can introduce the so called power balance transport coefficient of the species j:

$$\chi_j^{PB} = -\frac{q_j}{n_j \nabla T_i} \ , \tag{1.1}$$

where q_j is the absolute value of the heat flux $\mathbf{q}_j$, i. e. the amount of energy flowing through a magnetic surface in the unit time per unit surface. The relation between the confinement time and the heat transport coefficient is simply:

$$\tau_{Ej} \propto \frac{n_j T_j V}{q_j S} \propto \frac{n_j \nabla T_j a V}{n_j \chi_j^{PB} \nabla T_j S} \ , \propto \frac{a^2}{\chi_j^{PB}}$$

being a is the minor radius of the tokamak. Therefore, χ_j^{PB} provides a measure of the effective perpendicular heat transport, regardless of its physical meaning and of the mechanism governing transport.

1.2.2 Particle orbits

Before we can discuss different transport mechanisms we must first look at the particle orbits in a tokamak reactor. A tokamak is a device for magnetic confinement of plasma. The principle is simple: charged particles in a uniform magnetic field gyrate around the magnetic field direction with a fixed radius, called Larmor radius and given by

$$\rho_j = \sqrt{\frac{T_j}{2 m_j \Omega_{cj}^2}} \ , \tag{1.2}$$

where $\Omega_{cj} = e_j B / m_j$ is the gyration frequency of the particle species j in presence of a magnetic field B; e_j is the particle electric charge and m_j its relativistic mass. If $\rho_j \ll a$ particle are confined. They can then only leave the plasma through Coulombian collisions (classic and neoclassic transport) or through fluctuating electromagnetic fields.

Particle drifts

Actually, in a tokamak the magnetic field strength is not homogeneous and in addition the field lines are not straight. Both the curvature radius as well as the gradient length L_B are of the order of the major radius R and therefore much larger than ρ_j. However, every force in the plasma is associated with a particle drift. We try to give a simple physical picture of the drift associated with ∇B. For simplicity we assume that $\mathbf{B} = B\hat{z}$ and that the gradient is perpendicular to the field lines, $B = B(x)$ (see Fig. 1.3). The particle in its gyration orbit experiences different magnetic fields and correspondingly its Larmor radius will be smaller (closer orbit) where the field is higher, broader where B

gets smaller. At the end of a gyration the particle is displaced perpendicularly to the field and to its gradient, so that the orbit is not closed. As Fig. 1.3 shows, the "center" of the gyration (the guide center) drifts from the ideal field-line following trajectory. Note that electrons and ions drift in opposite directions because the gyration motion around **B** is anticlockwise for ions and clockwise for electrons.

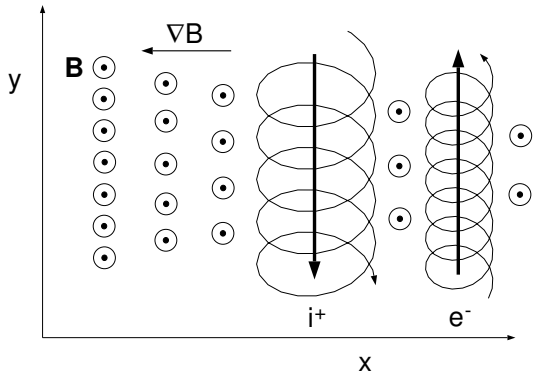

Figure 1.3: Particle drift due to ∇B.

Particle trapping

Another important effect of the magnetic field inhomogeneity is particle trapping. The magnetic field strength increases towards the tokamak axis. Since the field line is twisted around a toroidal surface, the particle experiences different magnetic field strength during its motion along the field line (see Fig. 1.4). This implies that particles with high $v_\perp$ and low $v_\parallel$ are reflected when reaching a critical value B_{ref} of the magnetic field; this is known as "mirror effect". Making use of the conservation of the kinetic energy ($E = mv^2/2$) and of the magnetic moment ($\mu = mv_\perp^2/2B$), which is an adiabatic invariant, the trapping condition reads

$$\frac{1}{2}mv_{\parallel 0}^2 < \mu B_{max} - \mu B_{min} \ ,$$

where B_{max} is the maximum field seen by a passing particle and $v_{\parallel 0}$ is the parallel velocity at the place where $B = B_{min}$. For an isotropic distribution function, in a tokamak we have:

$$\frac{v_{\parallel 0}^2}{v_0^2 - v_{\parallel 0}^2} = \frac{v_{\parallel 0}^2}{v_{\perp 0}^2} < \frac{B_{max} - B_{min}}{B_{min}} \approx \frac{2r}{R_o - r} = \frac{2\epsilon}{1 - \epsilon} \ ,$$

where $\epsilon = r/R_o$ is the local inverse aspect ratio of the tokamak at the radial position r. The trapped particles fraction is

$$f_t = \frac{n_t}{n} \approx \arcsin\left(\frac{v_{\|0}}{v_0}\right)_{limit} \approx \frac{v_{\|0}}{v_0}|_{limit} \approx \sqrt{\frac{2\epsilon}{1+\epsilon}}\ .$$

The projection of a trapped particle trajectory on a poloidal cross section is plotted in Fig. 1.4. Actually, if particle drifts were not present, the orbit would be aligned to the field line

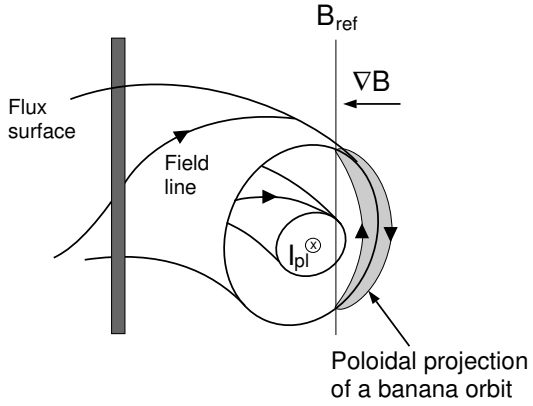

Figure 1.4: Trapped particles run along

and would have zero width. But since B increases towards the torus axis, both species drift in the vertical direction, as mentioned in the previous paragraph. As shown in Fig. 1.3 ions drift upwards. Above the equatorial plane (the plane in which the magnetic axis lies) they drift in the positive radial direction, below the equatorial plane they drift in the opposite direction. This makes that the poloidal projection of the orbit is closed but has a finite width, taking the characteristic banana shape, as shown in Fig. 1.4.

1.2.3 Neoclassic transport

The first attempts to estimate heat transport in plasmas perpendicular to the magnetic surfaces were based on Coulomb collisions, which scatter particles from their trajectory close to the field lines. Energy is transferred from one magnetic surfaces to a near one with an average displacement Δx in the perpendicular direction every τ_j^{coll} seconds. Here, τ_j^{coll} is the inverse of the 90^o scattering frequencies ν_{jj}, resulting from many small angle scattering. The typical radial step for ions' and electrons' random walk are assumed of the order of the respective Larmor radii. Heat diffusivities are derived from a "random walk" *Ansatz*:

$$\chi_i^{cl} \approx \rho_i^2 \nu_{ii} \approx \sqrt{\frac{m_i}{m_e}} \rho_e^2 \nu_{ee} \approx \sqrt{\frac{m_i}{m_e}} \chi_e^{cl}$$

and are predicted to be of the order 10^{-3} m^2/s and 10^{-4}-10^{-5} m^2/s for ions and electrons, respectively.

However, the assumption of uniform magnetic field does not hold for tokamaks. A more comprehensive theory has been developed [2], which takes into account the effects of tokamak geometry. This is the so called called neoclassic theory. The main new ingredient is the treatment of the banana orbits. Defining the thermal velocity as $v_j^{th} = \sqrt{T_j/m_j}$, the banana frequency results to be $\nu_b \approx v_j^{th}/qR$. If ν_b is larger than the effective collision frequency $\nu_{eff,j} \approx \nu_{ej}/2\epsilon$, trapped particles run several times on their banana orbits before they are scattered, so that the banana width can be taken as random walk step and the collision frequency is still the inverse time constant. The radial step is much larger than the Larmor radius and hence transport is increased:

$$\Delta x \approx r_b \approx \frac{q\rho_j}{\sqrt{\epsilon}}$$

$$\chi_e^{neo} \approx f_t r_b^2 \nu_{eff} \sim \frac{q^2\rho_e^2\nu_{ee}}{\epsilon^{3/2}} \approx \chi_e^{cl}\frac{q^2}{\epsilon^{3/2}}$$

For instance, $\epsilon = 1/4$ and $q = 3$ yield $\chi_e^{neo} \approx 70\chi_e^{cl}$. The heat conductivities are predicted to be:

$$\chi_e^{neo} \approx 0.005 \text{ m}^2/\text{s}$$
$$\chi_i^{neo} \approx \chi_e^{neo}\sqrt{m_i/m_e} \approx 0.2 \text{ m}^2/\text{s}$$

1.2.4 Anomalous transport

Although neoclassical transport coefficients are considerably higher than those predicted by the classical theory alone, the experimental values are still much higher:

$$\chi_e^{exp} \approx \chi_i^{exp} \approx 1 - 5 \text{ m}^2/\text{s}$$

The neoclassical prediction fails quantitatively, underestimating transport by one to several orders of magnitude. In other words, confinement is in real plasmas much worse than according to this theory. Also qualitatively the neoclassical prediction is not in agreement with the experimental measurements, which exhibit a ratio χ_i/χ_e close to one instead of the predicted square root of the mass ratio. This means that particularly for electrons other transport phenomena deteriorate dramatically the energy confinement time, while ion transport is less affected.

Scaling laws have been extracted from the experimental databases of different tokamaks [3] but their understanding in terms of physics is still being investigated. In particular the power degradation of confinement (the decrease of confinement with increasing heating power) cannot be explained by means of neoclassical theory. The additional transport has been called *anomalous* and has always been investigated by the fusion community

with particular interest.
Recent studies have shown that the ion thermal diffusivity can be reduced to neoclassical values at least in a narrow plasma region, the so called Internal Transport Barrier (ITB) [4]. However, this suppression of anomalous transport can so far be produced for a limited duration only. Electrons ITB have also been demonstrated [5], with temperature profiles as steep as in the ion barriers, but the neoclassical value is much lower than for ions and has not yet been reached.
Nowadays it is commonly believed that turbulence due to micro-instabilities causes anomalous transport: fluctuations in temperature and density combined with plasma drifts would carry a net heat flux which is considerably larger than neoclassical. In the last decade theory based transport models have been developed based on plasma turbulence, leading to confinement predictions. There is agreement that the main candidate to explain ion transport is the Ion Temperature Gradient (ITG) driven turbulence, possibly coupled to the Trapped Electron Mode (TEM). The stabilising contribution of the sheared plasma rotation $\omega_{E\times B}$ [6] is also commonly accepted. A physical picture of the toroidal ITG instability mechanism is given in section 2.2. However, different models based on the same basic modes yield different predictions, depending on the closure of the set of equations, on the stabilising and destabilising terms included and on the approximations made.
For electron transport until a few years ago most of the modelling attempts relied on empirical and semi-empirical models.

1.3 Steady state: power balance analysis

The goal of the steady state transport analysis is to investigate the amount of heat flux crossing the different magnetic surfaces when the plasma has reached the steady state. This can be done by measuring the effective heat diffusivity χ^{PB}, which provides a direct measure of the energy confinement performance of a tokamak, as mentioned in section 1.2.
The energy equation in its simplest form reads

$$n_j \frac{\partial T_j}{\partial t} = -\nabla \cdot \mathbf{q}_j + S_j = \nabla \left(n_j \chi_j^{PB} \nabla T_j \right) + S_j \ . \tag{1.3}$$

Therefore, χ_j^{PB} is also called "effective heat diffusivity", where "effective" refers to the fact that χ_j^{PB} might still depend on plasma parameters, thus making equation 1.3 not purely diffusive.
In the steady state, energy conservation 1.3 yields:

$$\nabla \cdot \mathbf{q}_j = S_{Qj}^{in} - S_{Qj}^{out} \ , \tag{1.4}$$

where S_{Qj}^{in} summarises the positive power sources and S_{Qj}^{out} the negative. To reconstruct the experimental heat flux, the power density profile of the auxiliary heating has to be known.
To input realistic power sources in the transport equation, further measured or reconstructed profiles are required, such as the plasma current density, the magnetic field strength, plasma density and both temperature profiles. The Ohmic heating is a power source depending on the electron temperature profile. Radiation (Bremsstrahlung) is a typical heat sink; but the warmer species has another heat loss due to collisions with the colder species. For high density discharges this is an important uncertainty source in the power balance analysis.
Integrating the steady state transport equation 1.4 over a magnetic surface labelled by the radius r, we obtain the local heat flux as:

$$q_j(r) = |\mathbf{q}_j|(r) = \frac{\int_0^r dr' \frac{dV}{dr'} \left[S_{Qj}^{in}(r') - S_{Qj}^{out}(r') \right]}{4\pi^2 R_o r} ,$$

where we have considered a circular plasma cross section for the sake of simplicity.
In the literature χ^{PB} is often referred to as power balance diffusivity. However, it is in principle a function of local plasma parameters as ∇n_j, ∇T_j, T_j, the safety factor q, Z^{eff}, the magnetic shear $\hat{s}$, the plasma collisionality, the ratio T_e/T_i. Therefore, the simple proportionality between heat flux and the product $n_e \nabla T_e$ may not hold. If, for instance, significant contributions to the heat flux are driven by the local temperature (and not by its gradient), χ^{PB} does not represent anymore the thermal diffusivity and exhibits a complicated dependence on the temperature gradient. The same difficulty occurs if transport is triggered by temperature gradients but only above a certain threshold (see Fig. 1.5). While it is easy to measure χ^{PB}, in reality

- there are large uncertainties under circumstances
- it is quite complicated to interprete its behaviour and improve our understanding of transport phenomenology.

1.4 Transient state: heat pulse analysis

Since several years a different kind of experimental approach has been developed to gain more information about heat transport. The idea is to perturb the plasma temperature profile and to measure the heat flux variation. The main quantity for this analysis is the perturbative transport coefficient, defined by the relation (see [7])

$$\tilde{\mathbf{q}}_j = -n_j \chi_j^{pert} \nabla \tilde{T}_j , \tag{1.5}$$

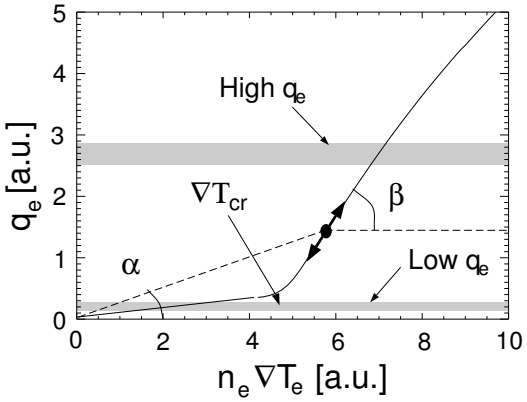

Figure 1.5: Example of transport model with critical temperature gradient; $\chi_e^{PB} = \tan(\alpha)$, $\chi_e^{pert} = \tan(\beta)$. Below the critical threshold ∇T_{cr}, i. e. for low q_e, $\chi_e^{PB} \approx \chi_e^{pert}$. Above ∇T_{cr} (high q_e) $\chi_e^{PB} < \chi_e^{pert}$

where the tilde indicates the perturbed quantities and j the plasma species. It is always possible to close the energy equation, without loss of generality, with

$$\mathbf{q} = -n\chi^{PB}\left(\nabla T, \alpha\right)\nabla T$$

if one allows χ^{PB} to depend on ∇T and on an arbitrary plasma parameter α. The species label has been dropped for simplicity. Linearising this closure yields the relation between χ^{PB} and χ^{pert}:

$$\chi^{pert} = \chi^{PB} + \frac{\partial \chi^{PB}}{\partial\left(\nabla T\right)}\nabla T + \frac{\partial \chi^{PB}}{\partial \alpha}\frac{\tilde{\alpha}}{\nabla \tilde{T}}\nabla T \ .$$

The last term is often assumed to be negligible because the temperature gradient is the quantity with the strongest variations when a temperature perturbation propagates in the plasma.

So far, the perturbative transport coefficient has been measured only for electrons. A possible perturbation arises from the propagation of a sawtooth crash, or can be induced artificially heating the plasma with a radio-frequency source [7]. However, it is difficult to measure the small increments because the experimental error bars are quite large, getting dramatic if one wants to diagnose variations of the temperature gradient. In order to reduce the experimental uncertainties and have a reliable measurement of χ_j^{pert}, it is useful to deal with periodic perturbations and perform a Fourier analysis of the propagating heat pulse [8]. Actually, the incremental transport coefficient is related to the propagation velocity of the heat wave, as we show in the following.

We can linearise the transport equation 1.3:

$$\frac{3}{2}n_o\frac{\partial \tilde{T}}{\partial t} = -\nabla \cdot \tilde{\mathbf{q}} + \tilde{S} \ . \tag{1.6}$$

Splitting the power terms into sources and sinks, the latter turn out to be proportional to $\tilde{T}$ if we assume collisional energy transfer as main sink. For homogeneous χ^{pert} the equation 1.6 becomes:

$$\frac{3}{2}\frac{\partial \tilde{T}}{\partial t} = \chi^{pert}\nabla^2\tilde{T} - \frac{\tilde{T}}{\tau_{eff}} + \tilde{S}' \ . \tag{1.7}$$

A wave solution of the form $\tilde{T} = T_\omega e^{i\omega t}$ must therefore fulfil

$$\left(\frac{3}{2}i\omega + \frac{1}{\tau}\right) T_\omega - \chi^{pert}\triangle T_\omega = S_\omega \ . \tag{1.8}$$

If the periodic sources are spatially localised, one can restrict the analysis to a region of source free plasma. This is well satisfied in the case of Electron Cyclotron Heating (ECH) (see section 5.1). The Fourier coefficient T_ω has a spatial dependence, due to the pulse propagation and damping. In an infinite slab geometry the wave is assumed to propagate in just one direction x with no boundary effects, so that we can write the perturbed temperature in polar notation as $T_\omega(x) = A(x)e^{i\varphi(x)}$ with $A \in \Re^+$ and $\varphi \in \Re$. The exponential form $T_\omega(x) = e^{zx}$ $z \in \mathbf{C}$ reduces 1.8 to an algebraic equation with solution

$$z = \pm\sqrt{\frac{3\omega}{4\chi^{pert}}}\left[\left(\sqrt{1+\Delta^2}+\Delta\right)^{1/2} + i\left(\sqrt{1+\Delta^2}-\Delta\right)^{1/2}\right] \ ,$$

where $\Delta := 2/(3\omega\tau)$ is the damping strength. Solving for χ^{pert} the real and imaginary part of

$$z = \frac{T'_\omega}{T_\omega} = \frac{A'}{A} + i\varphi'$$

yields the following relations:

$$\chi^{pert} = \frac{3\omega}{4\left(A'/A\right)^2}\left(\sqrt{1+\Delta^2}+\Delta\right) = \frac{3\omega}{4\varphi'^2}\left(\sqrt{1+\Delta^2}-\Delta\right) = \frac{3\omega}{4\varphi' A'/A} \ . \tag{1.9}$$

The details of the solution of equation 1.8 and the corrections due to the toroidal geometry and boundary effects are treated in [8]. In the rest of this thesis we adopt the most usual convention to plot as phase profile the quantity $\phi = -\varphi$ so that positive phase differences correspond to a delay.

Since both the amplitude and phase profiles of the temperature perturbation can be measured, the relation 1.9 provides an experimental estimate for the perturbative heat conductivity. Although this result is approximate and makes use of several assumptions, it allows to relate a fast wave propagation (flat phase and amplitude profiles) with a high incremental diffusivity. As shown in Fig. 1.5, χ^{pert} might deviate from χ^{PB}, indicating that heat transport is not simply diffusive. And actually in the experiment they are observed to be different and their ratio is power dependent [14], providing information about the transport mechanism. In the frame of this work, the estimate 1.9 has not been

applied to evaluate the coefficients quantitatively, but the heat wave propagation has been predicted by means of theory based models, with all their intrinsic dependences of χ on plasma parameters. Nevertheless, the graphical representations of A and φ allow a direct interpretation.

1.5 Content of this thesis

To understand anomalous transport in tokamaks remains a primary challenge in fusion oriented plasma research. Recent progresses in the development of turbulence codes and increasing knowledge of the experimental behaviour of heat transport encourage a quantitative comparison between theory and measurements. In this thesis several theory based models tested for the ITER (International Thermonuclear Experimental Reactor) confinement database are applied to different experimental situations.
In Chapter 2, a simple physics picture of the toroidal ITG instability is presented, together with an overview of the main ingredients of the theory contained in the models considered in the frame of this thesis.
A detailed derivation of the Weiland model's dispersion relation and transport coefficients follows in Chapter 3. This is meant as an example of how a fluid model is built, from the basic Braginskii equations [9] up to transport estimates, going through the details and the approximations of one of the most used 1D transport models.
Chapter 4 contains the simulation results obtained for standard H-mode discharges. Ion and electron heat transport is discussed with particular attention to profile stiffness, and the models are compared with the experiment qualitatively and quantitatively.
Theory based models have now been implemented into codes which are able to deliver predictions on T_e profiles [10] [11] [12] [13]. Recent progresses on the experimental side [14] as well as the development of these theoretical models have brought some clarifications and proposed physical explanations of electron transport. In several machines a threshold behaviour of electron transport is observed [14] [15] [16], and to the actual knowledge the underlying plasma instabilities could be either the Electron Temperature Gradient driven mode (ETG) or the TEM. In Chapter 5 the TEM based Weiland and GLF23 models are applied to electron cyclotron heated discharges, both for the steady state temperature profile as well as to the heat pulse propagation.
Preliminary modelling of discharges performed on the "Joint European Torus" (JET) is presented in Chapter 6 with particular focusing on the variation of the core heat flux and of the ratio T_e/T_i. This is the beginning of an inter-machine comparison between ASDEX Upgrade and JET with respect to profiles stiffness and validation of theoretical models.
Finally, the results are summarised and their impact on transport research is discussed. Further developments of the present work are proposed at the conclusion of this manuscript.

Chapter 2

Transport models

2.1 The ion temperature gradient driven instability

The heat losses in tokamaks largely exceed the predictions from the neoclassical theory. Plasma fluctuations have been observed [17] and made responsible for enhanced transport. Since a few decades it is commonly believed that this turbulent behaviour arises from micro-instabilities driven by the background density and temperature gradients. For a tokamak reactor, to understand low frequency micro-instabilities as the ITG mode is important, because they limit considerably the confinement performance of the device and thus its fusion efficiency.
In the quasi-linear theory one assumes that transport is determined by the fastest growing mode, and neglects the mutual interactions of the modes. A simple *Ansatz* for the transport coefficient is then provided by the mixing length estimate, which leads to the scaling

$$\chi \sim \frac{\Delta x^2}{\Delta t} \sim \frac{\gamma}{k_\perp^2} \ ,$$

where γ is the linear growth rate of the instability. With respect to confinement, the worst instabilities are those with long wavelength and high growth rate. This is of course a simplified model. The theoretical limits and inconsistencies of this approach are discussed in detail in the introduction of [18].

2.2 Simple picture of the toroidal ITG instability

The ITG driven instability is commonly believed to be the most significant mechanism limiting ion energy confinement in present tokamaks as well as in proposed larger fusion devices such as ITER.
Typically, the fastest growing ITG driven modes exhibit a perpendicular scale of the order

of the ion Larmor radius, satisfying $k_\perp^2 \rho_i^2 \approx 0.1$. This means that the ITG spatial scale is small compared to the tokamak minor radius, but much larger than the Debye length. Frequencies are in the range of the diamagnetic drift frequency $\omega_\star$, therefore much lower than the plasma frequency.

The toroidal version of this mode is basically due to the combination of the curvature and ∇B ion drifts on the one hand and the $E \times B$ drift on the other. Drift velocities and frequencies are defined in Table 2.1. A simplified picture of the instability in toroidal geometry can be given assuming a local approximation, where each Fourier component of the perturbation is considered independent, thus neglecting the possible coupling effect of plasma inhomogeneities [18]. The instability grows in the unfavourable curvature region, where ∇T_i and ∇B are parallel; this is the case in the low field side of tokamaks. A magnetic surface has constant T_i, unless a perturbation occurs for some reason (see Fig. 2.1). The poloidal ion drift, due to both ∇B as well as magnetic field curvature, is

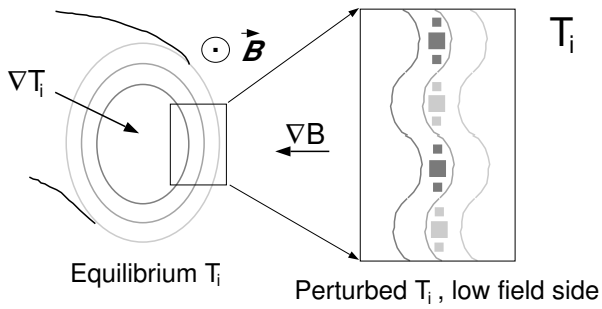

Figure 2.1: T_i perturbation in the low field side of a tokamak: $\nabla B \parallel \nabla T_i$

proportional to T_i. Therefore, if T_i is perturbed, this drift leads to a compression of ion density in the poloidal direction, with queues where the poloidal velocity gradient is negative and rarefaction in the zones with positive velocity gradient (see Fig. 2.2). Quasi-neutrality forces a corresponding electron density perturbation which is equal and hence also in phase with the ion density perturbation. Neglecting electron trapping for simplicity, the electrons can assumed to be adiabatic because of their fast dynamics, yielding an electrostatic potential proportional to the density perturbation and with the same phase:

$$\tilde{n}_e = n_e - n_{eo} \approx n_{eo} \left(\exp\left\{ \frac{e\phi}{T_e} \right\} - 1 \right) \approx n_{eo} \frac{e\phi}{T_e} \ . \tag{2.2}$$

The density perturbation is, therefore, associated with a poloidal variation of ϕ, which gives rise to a radial electrostatic drift (see Fig. 2.3). This perpendicular ion fluid motion carries plasma from the side with lower B to the cold spot and from the higher B region to the warm spot. If the background ∇T_i is parallel to ∇B, cold plasma is carried to the

Quantity	*Definition*	*Drift type*
$\mathbf{v}_E$	$\frac{\mathbf{e}_\parallel \times \nabla\phi}{B}, \frac{\mathbf{E}\times\mathbf{B}}{B^2}$	$E \times B$ *or electrostatic*
$\mathbf{v}_{pj}$	$\frac{1}{B_0\Omega_{cj}}\left[\frac{\partial \mathbf{E}}{\partial t} + (\mathbf{v}\cdot\nabla)\,\mathbf{E}\right]$	*Polarisation*
$\mathbf{v}_{\pi j}$	$\frac{\mathbf{e}_\parallel \times \nabla\cdot\pi_j}{e_j n_j B_0}$	*Stress tensor or anisotropy*
$\mathbf{v}_{\star j}$	$\frac{\mathbf{B}\times\nabla p_j}{e_j n_j B^2}$	*Diamagnetic*
$\mathbf{v}_{curv}$	$\frac{m_j < v_\parallel^2 >}{e_j B}\frac{\mathbf{B}\times\nabla B}{B^2}$	*Curvature*
$\mathbf{v}_{\nabla B}$	$\frac{m_j < v_\perp^2 >}{2e_j B}\frac{\mathbf{B}\times\nabla B}{B^2}$	∇B
$\mathbf{v}_{Dj}$	$\frac{2T_j}{e_j B}\frac{\mathbf{B}\times\nabla B}{B^2}$	$\mathbf{v}_{curv} + \mathbf{v}_{\nabla B}$
$\omega_{\star j}$	$\frac{k_\perp T_j \nabla n_j}{e_j n_j B}$	*Diamagnetic frequency*
ω_{Dj}	$2\frac{k_\perp T_j}{eB}\frac{\nabla B}{B}$	*Curvature and* ∇B *frequency*

(2.1)

Table 2.1: Definition of the drift velocities and frequencies. The subscript j labels the plasma species.

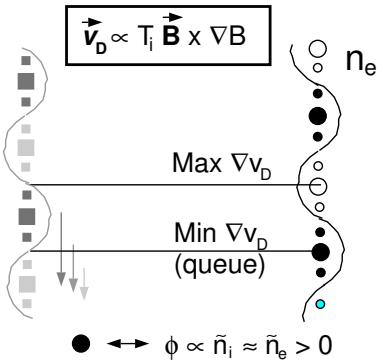

Figure 2.2: n_i compression due to magnetic curvature and ∇B drifts

cold region, thus amplifying the perturbation and driving the instability, as shown in Fig. 2.3. A net amount of heat is transported as to flatten the background ion temperature

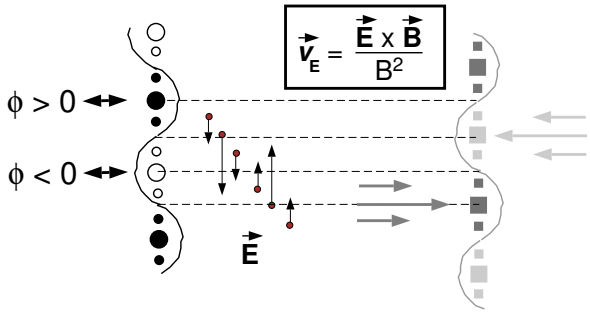

Figure 2.3: Amplification of the T_i perturbation through the electrostatic drift, last step of the $n_i - T_i$ instability loop

gradient: in Fig. 2.3, the heat flows towards the right hand side. We notice that, since v_E and $\tilde{n}_e$ are phase shifted by $\pi/2$, there is no net particle transport according to this simplified model.

2.3 ITG instability and profile stiffness

According to the ITG models, turbulent transport is excited when the inverse gradient length $1/L_{T_i} = -\nabla ln T_i$ exceeds a certain critical value $1/L_{T_{cr}}$. A similar threshold mechanism can be invoked to explain electron transport, for instance through the so called Trapped Electron Mode (TEM). Chapter 3 provides an example of how a critical

threshold eventually arises according to the theory, with a prediction for ITG and TEM combined.

If the increase of transport above the turbulence onset is strong enough, a clearly over-critical temperature gradient can be induced only by a large heat flux. Since the heating power is limited, the logarithmic temperature gradient tends not too exceed significantly the critical value. On the other hand, if the gradient is under-critical, no anomalous transport occurs, and the remaining neoclassic contribution is small and allows ∇T to steepen, until $1/L_{T_{cr}}$ is reached. This means that temperature profiles tend to be "stiff", keeping more or less bound to the critical $\nabla T/T$ profile, almost independent of the amount of heat deposited and of the shape of the power density profile. The ITG and TEM physics do not apply in the pedestal region, where other modes determine the density and temperature profiles. Therefore, even in a scenario with strong profile stiffness the boundary temperature has freedom to vary. However, if the critical gradient length does not depend strongly on plasma parameters, in the core plasma the temperature profile is fixed:

$$T(r) = T(ped) \exp\left\{\int_{ped}^{r} \left[-\frac{1}{L_{T_{cr}}}(r')\right] dr'\right\} = \alpha\,(r)\, T(ped)\ . \tag{2.3}$$

Gradients can be steepened just by enhancing the pedestal temperature, regardless whether the input power is increased or not. On the other hand, a heat flux variation does not affect the temperature gradient; in terms of χ, this leads to a strong power degradation of the effective heat diffusivity: $\chi \propto P_{Heat}^{-1}$. This behaviour is quite different from the prediction relying on a simple diffusive model, where χ is constant and transport is determined by the Fourier's law

$$q = -n\chi\nabla T \tag{2.4}$$

In this case, the temperature gradient is proportional to the local heat flux and does not depend at all on the pedestal temperature value. The different behaviours are illustrated in Fig. 2.4. As equation 2.3 shows, if the critical threshold does not change too much from discharge to discharge, then the ratio of core to pedestal temperature remains fairly constant throughout the database. This is an experimental evidence of profile stiffness, although it is not a proof: in the experiment it is not always easy to decouple the situations a) and b) of Fig. 2.4, in particular when performing a power scan, because the pedestal temperature increases with the heating power. It is easier to distinguish between a) and b) by means of a density scan, where the boundary temperature is changed by factors of 3-4 without affecting the total amount of heat deposited.

A measure of the tendency of $\nabla T/T$ to stay close to the critical inverse gradient length is how steeply χ increases after R/L_T exceeds its critical value, i. e. the quantity $\partial\chi/\partial\,(R/L_T)$, which is closely related to the definition of incremental transport in equation 1.5. This quantity can be measured for electrons by means of heat waves, as discussed in section 1.4, providing direct information about eventual profile stiffness.

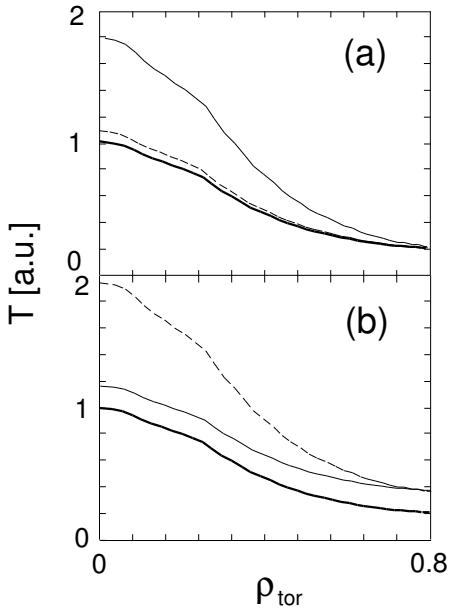

Figure 2.4: Example of temperature profile (thick solid line) and its modifications according to a constant χ model (thin solid line) and to a stiffness-model (dashed line) when: (a) Fixed the boundary T, increasing the heating power. (b) Fixed the input power, changing the pedestal T.

2.4 Theory based transport models

In the ITER confinement database several 1D transport models are employed to give predictions about the performances of the next generation fusion device [19]. Some of them are classified as semi-empirical, others are derived from first principles. We have studied the latter, in order to improve the physics understanding and to validate the underlying physics against ASDEX Upgrade and JET data. In the following paragraphs we provide a general overview on the four models employed for our transport studies: three of them are based on the physics of the ITG driven turbulence coupled to the TEM, namely the IFS/PPPL [20], Weiland [12] and GLF23 [13] model, whereas the fourth relies on a different physics, i. e. the self-sustained turbulence driven by the Current Diffusive Ballooning Mode (CDBM) [21].
Only the Multi-Mode Model (MMM) [22] has not been applied so far, since it has been implemented only recently into the ASTRA transport code. However, we focused our studies in the core plasma and in that region the multi-mode model includes a version of the Weiland model for the ITG and TEM instabilities.
None of the models considered here, in the versions used for our studies, has adjustable

parameters or *ad hoc* assumptions for a particular tokamak.
The stabilising contribution of the $\omega_{E\times B}$ shear is included in all models following different implementations (see Section 4.4.1).

2.4.1 The IFS/PPPL model

The model has been developed in the early nineties. Its name is related to the institutes where it was developed: Institute for Fusion Studies (Austin, Texas) and Princeton Plasma Physics Laboratory (Princeton, New Jersey) [20].
The model relies on first principles non linear fluid simulations, corrected and completed by a comprehensive linear gyrokinetic code [23]. Analytic expressions for the transport coefficients are derived by fitting the theoretical simulations:

- the formula for χ_i is given by gyrofluid simulations with corrections from the quasi-linear gyrokinetic estimate, in order to reduce the large amount of non-linear gyrofluid runs, which require a long computing time.
- "The electron χ_e is obtained from the ratio of the quasi-linear electron and ion heat fluxes found with the comprehensive linear code" ([20], pag. 2383); the ratio is found to be a weak function of plasma parameters, so that ion and electron transport scale similarly.
- Anomalous transport due to ITG is triggered only if the ion temperature gradients exceed a certain threshold. The threshold is obtained from the linear gyrokinetic code.
- Beside the ion temperature gradient, the threshold depends on the density gradient, the magnetic shear, the safety factor, collisionality, the ratio T_e/T_i and the effective ion charge Z_{eff}.
- Profile stiffness can be measured by the high increase of χ_i above the critical gradient; the coefficient before the Heaviside function has an important $T_i^{3/2}$ dependence, the so called Gyro-Bohm factor.

2.4.2 The Weiland model

This is a fluid model based on ITG and TEM coupling [12]. The derivation of the model's equations and of the quasi-linear transport coefficients is presented in Chapter 3. Now we shortly summarise the most relevant approximations:

- There are thresholds in both ion and electron temperature gradient lengths; if the gradients are below the critical value, transport is neoclassic.

- The closure is obtained taking the heat flux as the diamagnetic heat flux with isotropic temperature.
- In the version considered here (7 equations), electromagnetic effects are neglected, although more recent versions of the model do consider them too. The ion parallel motion and shear effects are included, but their description is simplified.
- The background electrostatic field is assumed to be zero, except when considering the stabilising term $\omega_{E\times B}$.

2.4.3 The GLF23 model

The GLF23 (Gyro-Landau Fluid) model is also based on the fluid equations [13]. However:

- The closure is different from that of the Weiland model. "The complex coefficients of these linear combinations [of the lower moments] are chosen to best fit the general kinetic plasma response function over the full range from small and large values in all the kinetic parameters: the gyroradius parameter $\left(k_\perp \rho\right)^2/2$; the parallel motion parameter $k_\parallel v_{th}/\omega$; and the curvature drift parameter ω_D/Ω." ([24], pag. 3138).
- "The toroidal ion temperature gradient (ITG) mode, the collisionless to dissipative trapped electron drift modes, and the ideal magnetohydrodynamic (MHD) ballooning modes, as well as the edge resistive wall modes, are included" ([13], pag. 2482).
- The model assumes a magnetic shear ($\hat{s}$) - Shafranov shift (α) stabilisation. Landau damping is taken into account.

2.4.4 The CDBM model

The Current Diffusive Ballooning Mode model is based on different physics than the previous three models [21].

- The nonlinear instabilities generate anomalous transport. "In this new theoretical approach, instabilities are caused by anomalous transport itself" ([21], pag. 1743), i. e. turbulence is self-sustained. "In this non-linear destabilisation mechanism, the role of the current diffusivity is essential" (*ibidem*).
- The model has in principle no threshold in the ion temperature gradient.
- Electron and ion heat diffusivities are assumed to be equal.

2.4.5 Main dependences within the models

A quantitative comparison between the transport models and the experiments might not be conclusive to judge which physics underlies the experimental phenomenology; it is much more reliable to observe a correct dependence on the relevant physical parameters. In addition, some models are constructed or tested only for certain parameters ranges and it is important to check to which extent each model is applicable to simulate the experiments. For this reason we address now to the investigation of the models' reaction to the physical quantities without caring about the reproduction of the experimental profiles, in that we run the models stand-alone. The only link to the experiment is that we choose as background parameters the values at half radius of a typical case of NBI heated H-mode discharge as well as one on-axis ECH discharge. Each parameter is then varied separately, although in concrete experimental situations it is not always possible to scan a single quantity, since other parameters might be coupled and change as well. The two

Discharge	R/L_{T_i}	R/L_{T_e}	R/L_{n_e}	q	$\hat{s}$	Z_{eff}	T_i	T_e	T_e/T_i	n_e
13042	7.4	5.3	3.2	1.8	0.9	1.1	3.4	2.8	0.8	3.7
13558	*2*	9.1	0.4	1.7	0.9	1.1	*0.7*	2.4	3.2	2.0

Table 2.2: Background parameters for the stand-alone runs of the models. T_i is not measured for # 13558. The arbitrary values $T_i = 0.7$, $R/L_{T_i} = 2$ are taken.

standard sets of background parameters are presented in Table 2.2. Given the respective values of n_e and T_e, the collisionality in the two discharges is roughly the same and fairly low.

We split the exercise for the ITG/TEM models on one hand and for the CDBM model on the other hand, since they contain different dependences.

Although the IFS/PPPL, GLF23 and Weiland models are based on the same instability mechanisms, they yield different transport predictions, also qualitatively, due to the different approaches and approximations. In the Weiland model, the collisions on trapped electrons are switched off, in agreement with the standard setup assumed in this thesis (see Section 4.4.1) and most common in the literature. The stabilising effect of $\omega_{E\times B}$ has been neglected for all models, in order to distinguish more clearly the physics effects within the models. The ITG/TEM models are primarily sensitive to R/L_{T_i}, R/L_{T_e}, R/L_{n_e}, the safety factor q, $\hat{s}$, the effective ion charge Z_{eff}, the ratio T_e/T_i and the temperature values. The scanned quantity can vary the transport level for two contributions which are not easy to decouple:

- increasing that parameter enhances the turbulent heat flux

- the critical gradient length is shifted because it depends on the scanned parameter

So as a first step we analyse the threshold behaviour of the models with respect to the temperature gradients. This investigation is also a direct test to determine how "stiff" are the temperature profiles according to the ITG/TEM models, in the spirit of the explanation in Section 2.3. Profile stiffness is actually a crucial question in transport research nowadays. Figure 2.5 (a) illustrates the different behaviours of the ITG turbulence: the

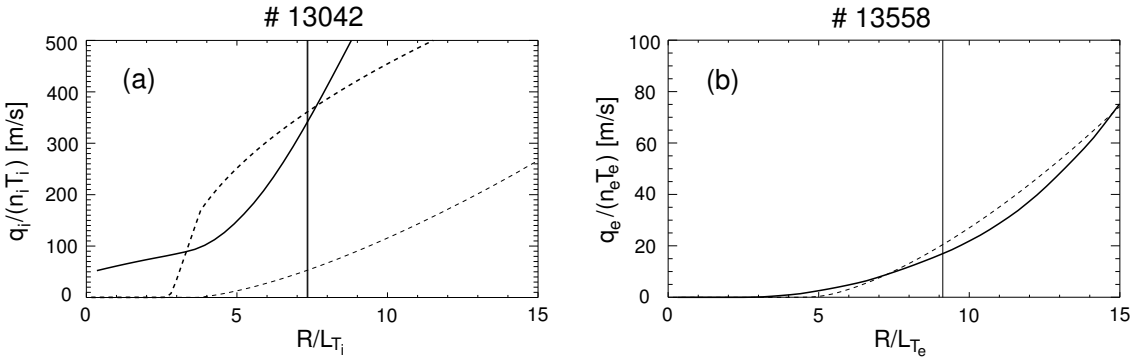

Figure 2.5: Dependence of the heat fluxes on the inverse temperature gradient lengths according to the GLF23 (solid line), Weiland (thin dashed line) and IFS/PPPL (thick dashed line) models. (a) Ion heat flux versus ion temperature gradient, background parameters from Table 2.2, first row. (b) Electron heat flux versus electron temperature gradient, background parameters from Table 2.2, second row. The vertical line represents the experimental value of the scanned quantity as reported in Table 2.2. The IFS/PPPL model is not plotted in (b) because it does not depend on R/L_{T_e}.

Weiland and GLF23 models have a similar ITG stability threshold around $R/L_{T_i} = 4$, IFS/PPPL somewhat lower. However, the GLF23 model has significant residual transport even for flat T_i profiles, due to the high density gradient (see also Fig. 2.6). The GLF23 and IFS/PPPL models exhibit a steep increase of transport above the threshold, whereas the Weiland model returns a smoother growth. In other words, T_i profiles are predicted to be "stiffer" for IFS/PPPL, less for Weiland; GLF23 has not a clear threshold behaviour under circumstances (e. g. high ∇n_i), being the residual transport already quite high. The absolute values of the ion heat flux are much higher for GLF23 and IFS/PPPL than for Weiland, at least for the background parameters as in Table 2.2. However, this is not so significant because a slightly lower input gradient reduces the transport level considerably: running the models in predictive mode, the calculated profiles can still be within the experimental uncertainty. For this reason, in the frame of an ITG dominated transport it is not useful to perform a local analysis in terms of χ's, being $R/L_{T_{cr}}$ the determining

quantity.
In Fig. 2.5 (b) the IFS/PPPL model is not shown since it has no explicit dependence on R/L_{T_e}. The GLF23 and Weiland model exhibit similar behaviour and do not predict a strong T_e profile stiffness, as the heat flux increases smoothly above the critical threshold. However, there are significant differences between the models which will be discussed in detail in Section 5.8.
In the theory the density gradients are closely related to R/L_{T_i} and R/L_{T_e}, which enter the equations almost always in the combination $\eta_i = L_{n_i}/L_{T_i}$ and $\eta_e = L_{n_e}/L_{T_e}$. Also the TEM stability threshold is influenced by the density gradient, as it will be clarified in Equation 3.19 and Fig. 3.1. In addition, since the experimental uncertainties on the experimental profiles can lead to large errors in the density gradient, it is necessary to evaluate the sensitivity of each model to this parameter. Figure 2.6 illustrates its impact on transport. Both the ion as well as the electron density gradient length are varied, keeping $L_{n_i} = L_{n_e}$ in order to preserve quasi-neutrality. While the IFS/PPPL and Wei-

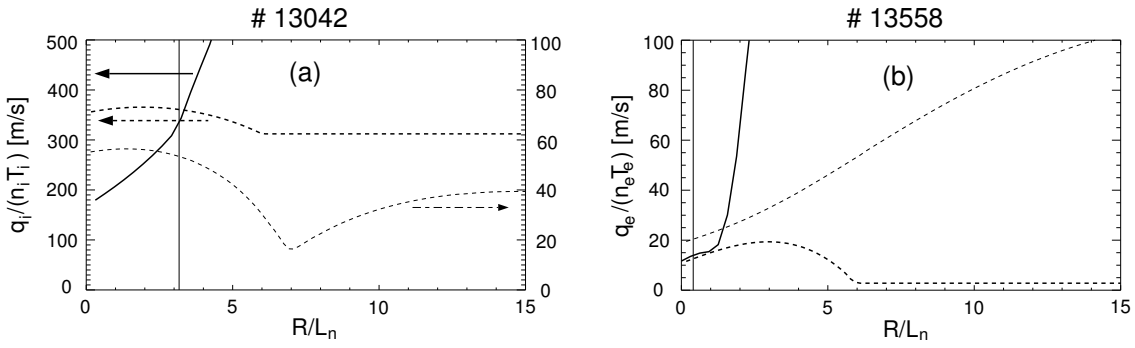

Figure 2.6: Ion (a) and electron (b) heat flux versus the density gradient length. Lines and background parameters as in Fig. 2.5. Notice the different scale for the Weiland model output.

land models react weakly to density gradient changes, GLF23 is affected dramatically in both cases. This particular sensitivity is well known and will be discussed in detail when evaluating the actual simulation results, in Section 4.4.2. We only remark that the local analysis may yield large errors because we use the experimental density profiles. Therefore, the modelling must take place over the entire core plasma region, in order to reduce on average the error due to the density gradient.
For the Weiland model, the TEM (dominating transport in Fig. 2.6 (b)) should be stabilised by a high electron density gradient; this is observed if one varies only R/L_{n_e}. However, since in Fig. 2.6 also R/L_{n_i} is varied for consistency, other modes driven by the ion density gradient couple to the pure TEM and increase the turbulent heat flux.

The IFS/PPPL formulas for χ's are not constructed for $R/L_{n_e} > 6$, therefore for steeper density gradients no influence on heat transport is assumed and the model is not expected to reproduce the temperature profiles.

Another important parameter for the ITG turbulence is the ratio $\tau = T_e/T_i$; its direct

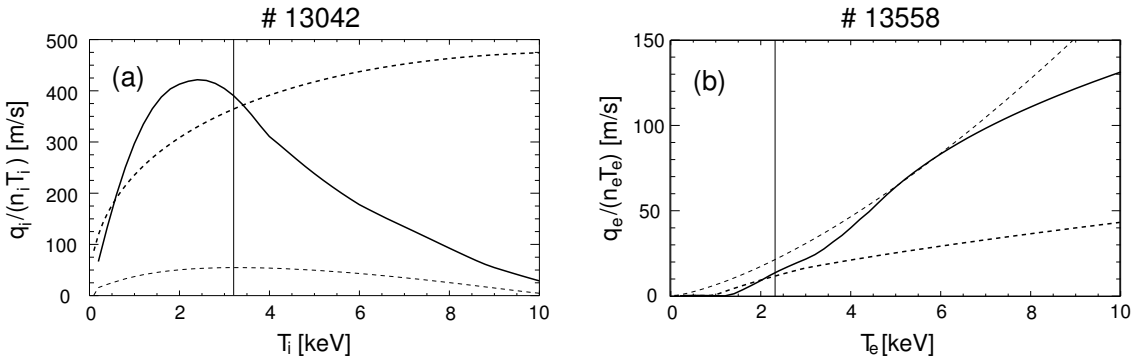

Figure 2.7: Dependence of the ITG models on the temperature. (a) Ion heat flux versus T_i (b) Electron heat flux versus T_e. Lines and background parameters as in Fig. 2.5.

impact on transport can be investigated varying it artificially, keeping constant both T_i and T_e. Instead, we report in Fig. 2.7 the experiment-relevant scans, where either T_i (a) or T_e (b) are varied. Actually the temperature values strongly affect transport, determining to which extent the temperature profiles are expected to be stiff, as the models contain a $T^{1.5}$ dependence before the transport coefficients - the so called Gyro-Bohm factor. Notice that the temperature gradient lengths are kept fixed to the value reported in Table 2.2. For the ion case, both the Weiland and GLF23 models reach a maximum destabilisation of the mode when T_i equals T_e and then bend to a lower transport level; the IFS/PPPL model predicts the turbulent flux to increase monotonically with T_i. Hot electron temperatures enhance the TEM turbulence according to all models.

Impurities are treated differently by the models as illustrated in Fig. 2.8. In (a) it appears that the IFS/PPPL and Weiland model describe also impurity transport, whereas GLF23 in the version we have used takes simply a dilution approximation which causes Z_{eff} to always moderate the ITG. In the IFS/PPPL model the ITG carbon branch becomes overwhelming for $Z_{eff} > 4$. For the TEM mode (see Fig. 2.8 (b)) Z_{eff} has nearly no effect - we remind that within the IFS/PPPL model χ_e is taken as roughly proportional to χ_i.

Finally we report the dependences on the safety factor q (Fig. 2.9) and the magnetic shear (Fig. 2.10). The Weiland model depends very weakly on q, which in the core plasma ranges between 1 and 4; most probably the assumption for the q-dependence is too simplified. In general, q is observed to raise the turbulence level.

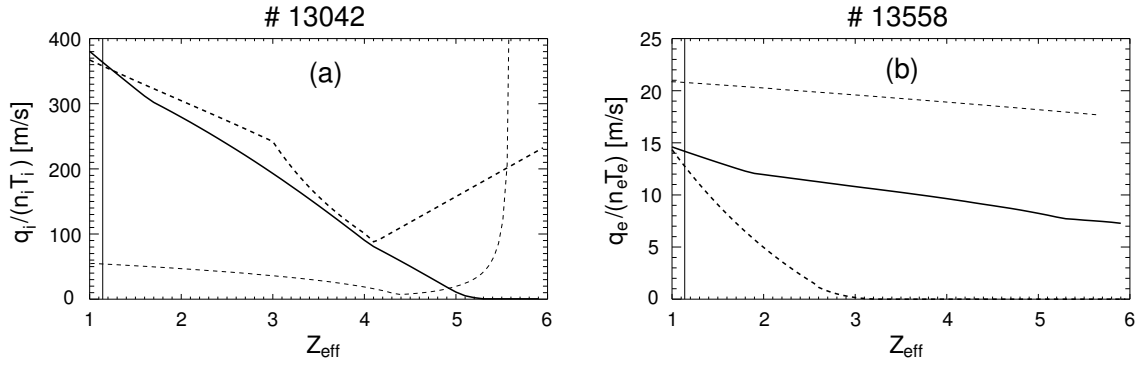

Figure 2.8: Ion (a) and electron (b) heat flux versus the effective ion charge. Lines and background parameters as in Fig. 2.5.

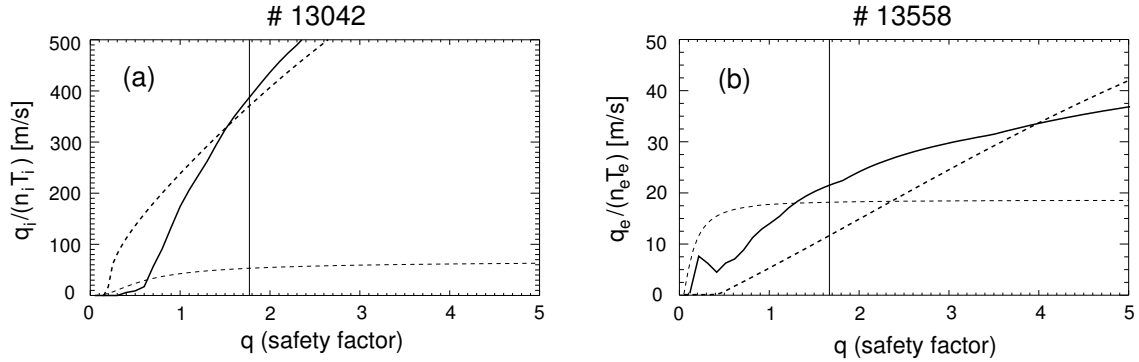

Figure 2.9: Ion (a) and electron (b) heat flux versus the safety factor q. Lines and background parameters as in Fig. 2.5.

The IFS/PPPL formulas for χ's are not tested for low and negative shear, below 0.5, as reported by the authors [20]. The Weiland model assumes a dependence only on $|\hat{s}|$, a strong approximation which makes the model inadequate to describe negative shear scenarios. In addition, the dependence on $\hat{s}$ is observed to be linear. The GLF23 model has a more accurate description, with good overlapping with the IFS/PPPL model in the validity range of the latter. The magnetic shear is found to stabilise the turbulence for high as well as negative values.
The CDBM model depends mainly on q, $\hat{s}$ and collisionality. In the version available, ion and electron heat transport are assumed to be equal. The maximum destabilisation for ion heated discharges (see Fig. 2.11 (a)) is obtained for $1.5 < q < 2$, but transport remains high over the whole plasma core. For electron heating dominated discharges, the

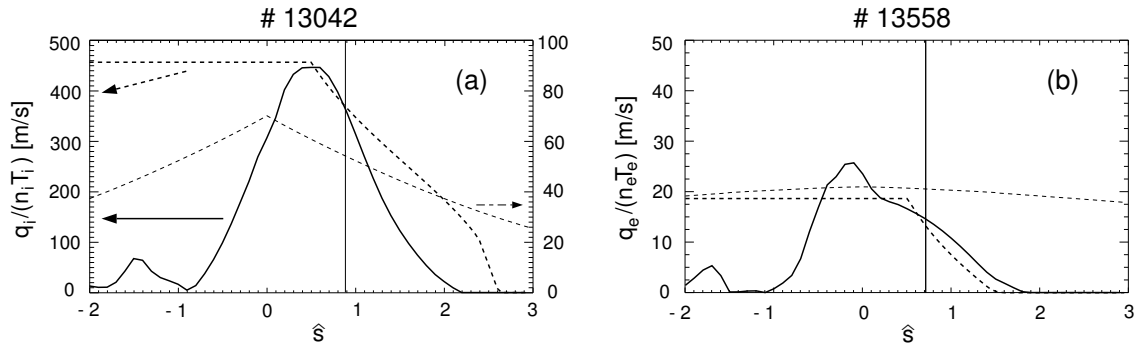

Figure 2.10: Ion (a) and electron (b) heat flux versus the magnetic shear $\hat{s}$. Lines and background parameters as in Fig. 2.5.

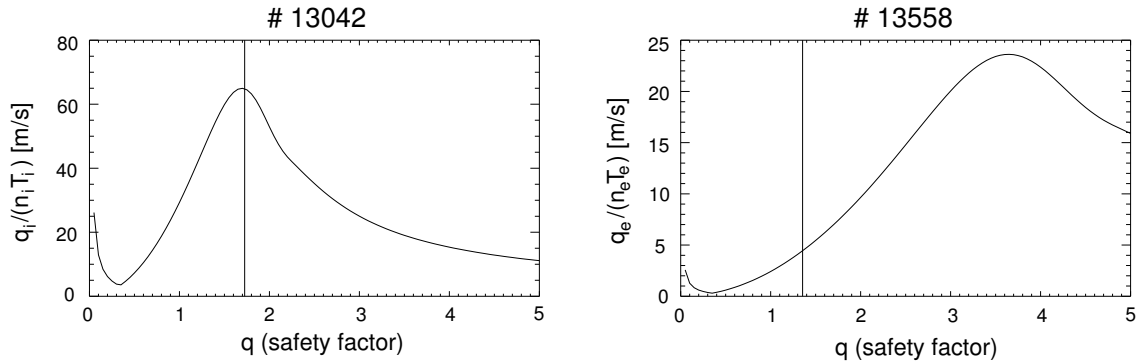

Figure 2.11: Dependence of the CDBM model on the safety factor q.

turbulent flux driven by the CDBM is lower and reaches its maximum around $q = 4$, which belongs to the pedestal region for typical ASDEX Upgrade discharges.
The dependence on the magnetic shear is shown in Fig. 2.12 and has a quite different shape. The mode is stabilised for low and negative $\hat{s}$, then transport experiences a step-like increase; this is, however, much smaller in the case of the background parameters taken from the electron heated discharge.

The overall lower transport level for the ECH discharge can be probably explained through the lower ion temperature. Figure 2.13 illustrates the behaviour of heat transport for increasing temperature.
Considering the dependences on q and $\hat{s}$, it is interesting to look at the effect of the plasma current on the entire temperature profiles. The discharge # 13042 with $P_{NBI} = 5$ MW, $I_{pl} = 1$ MA and medium density is simulated with the CDBM model, setting the bound-

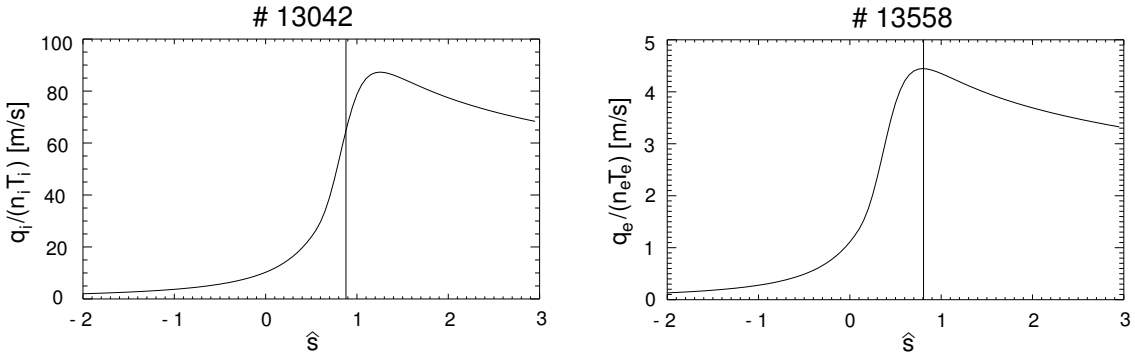

Figure 2.12: Dependence of the CDBM model on the magnetic shear $\hat{s}$.

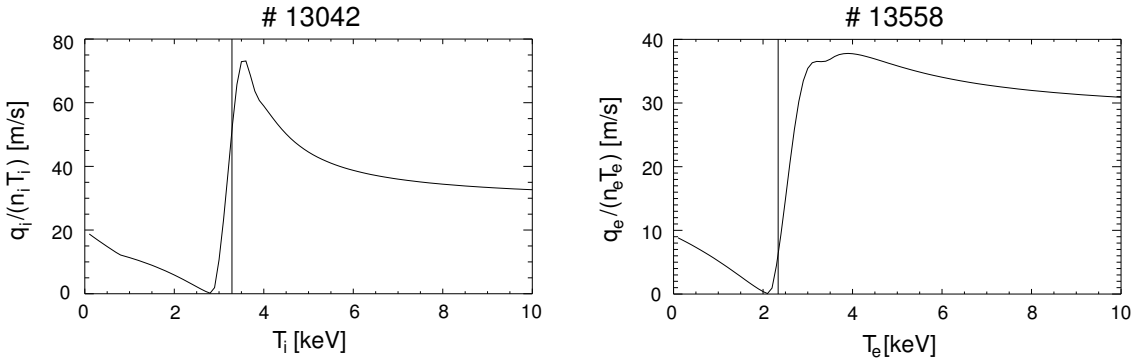

Figure 2.13: Dependence of the CDBM model on the temperature values.

ary condition for the temperatures at $\rho_{tor} = 0.8$, where ρ_{tor} is the normalised toroidal flux coordinate. The input current is varied artificially from 0.8 to 1.2 MA, corresponding to a 40 % variation. This changes significantly the edge q values from $q(\rho_{tor} = 0.95)$=4.8 (for 0.8 MA) to $q(0.95) = 3.0$ (with 1.2 MA). When the q profile is stationary, the modelled temperatures appear not to be affected by the change in the plasma current: $T_i(0.4)$=2.49 keV and $T_e(0.4)$=2.06 keV in the case with 0.8 MA, $T_i(0.4)$=2.48 keV and $T_e(0.4)$=2.07 keV in the case with 1.2 MA. One reason is that q values are less modified in the core region, where the temperature profiles are modelled. Besides, Fig. 2.13 shows a resilience of the temperature to deviate from a given value: as soon as this is exceeded, high heat transport is generated and recovers the previous value. Plotting the analogous of Fig. 2.13 (a) in the cases of 0.8 MA and 1.2 MA yields indeed similar results.

Chapter 3

The theory of the Weiland model

3.1 Introduction

In the following we derive the equations of the Weiland model and the subsequent quasi-linear estimate for heat and particle fluxes. Although no new physics is added to the original Weiland model, this review unifies results from different works, such as [25] and [12]. Most final results are published, but have never been derived explicitely in the publications. This section also provides an attempt to list together all the assumptions contained at different stages in the model, giving an overview on the physics approach and on the model's consistency.
The model we derive here is the simplest one containing ITG and TEM modes coupled, which corresponds to the four equations version.
According to the equations and transport coefficients derived in the following, a simplified model has been implemented as a Fortran code in order to benchmark the more complete model and allow a more direct control on the behaviour of the different physics ingredients. Modelling results of JET discharges with this simplified version of the Weiland model can be found in Chapter 6 together with the simulations performed with the models presented in section 2.4.
Among the several transport models considered, the Weiland model has a fairly transparent physics, based on the fluid equations and quasi-linear transport coefficients. It contains only algebraic equations and the formulas are analytic. Nevertheless, it predicts temperature profiles in good agreement with the measurements in a variety of experimental conditions.
Complements to the following derivation can be found in Appendix B.

3.2 Assumptions

The Weiland model is a fluid model based on the physics of ion temperature gradients and trapped electron mode. Transport is induced when a critical threshold in the inverse gradient length $1/L_{T_j}$ is exceeded.
Besides the drift velocities and frequencies (see Table 2.1), it is important to define the following quantities:

$$\begin{aligned}
\mathbf{e}_\parallel &= \frac{\mathbf{B}_0}{B_0} \\
\eta_j &= \frac{L_{n_j}}{L_{T_j}} \\
\epsilon_n &= \frac{2L_n}{L_B} \\
c_s &= \sqrt{\frac{T_e}{m_i}} \\
\beta_j &= \frac{4\pi p_j}{B^2} \\
\rho_s &= \sqrt{\frac{T_e}{m_i \Omega_{ci}^2}} \\
\tau &= \frac{T_e}{T_i} \\
N_j &= \omega^2 - \frac{5}{3}\omega\omega_{Dj} + \frac{10}{3}\omega_{Dj}^2 \ .
\end{aligned} \tag{3.1}$$

Deriving the equations, it is assumed for simplicity that there is only one ion species and that it is an isotope of hydrogen. Therefore, either $j = i$ or $j = e$ and $Z = 1$. Impurities are not treated and the parallel ion motion is neglected.
The model relies basically on the following physics assumptions:

- $k_\parallel / k_\perp \ll 1$, and in the perpendicular direction for the linear case $k_x \ll k_y$, where x refers to the radial and y to the poloidal direction. This corresponds to the fact that the linear modes which transport most of the heat exhibit elongated structures in the radial direction. As a consequence, $\nabla \approx ik_y$ and $\mathbf{k} \cdot \mathbf{v}_D \approx \omega_D$. However, when the instability saturates due to nonlinear terms, it is assumed to be isotropic: $k_x \approx k_y$.

- Finite β effects are neglected, in particular

$$\frac{\delta B_\parallel}{B_0} \approx -\frac{\mu_0 \delta p}{B_0^2} \ll 1 \ .$$

- Passing electrons are assumed to be adiabatic:

$$\frac{\delta n_{ep}}{n_{ep}} = \frac{e\phi}{T_e} \ . \tag{3.2}$$

- The trapped electrons dynamics is symmetric to the ion dynamics.
- The plasma is quasi-neutral: $n_e \approx n_i$ is satisfied also at the first order, $\delta n_e \approx \delta n_i$.
- The heat flux is set equal to the diamagnetic heat flux (see Appendix B.3.2). This means that the Braginskii equations are retained up to the second moment, with closure coming from the third moment by assuming that the distribution function is Maxwellian.
- There is no background $\mathbf{E}$ except when the stabilising effect of $\omega_{E\times B}$ is implemented (not self-consistently). $\mathbf{E}_\perp$ is assumed to be electrostatic. Electromagnetic effects are not considered in the version of the model employed for this thesis.
- The drift ordering (see [26], paragraph 3.V) applies:

$$\delta = \frac{\rho_s}{L_\perp} = \frac{c_s}{L_\perp \Omega_{ci}} \sim \frac{\delta n}{n} \approx \frac{e\phi}{T} \ll 1 \ ,$$

  where ρ_s and c_s are defined in 3.1 and represent respectively the ion Larmor radius times $\sqrt{T_e/T_i}$ and the sound wave velocity. $L_\perp$ is the smallest gradient length of a background quantity, such as temperature or density. For frequencies the same ordering reads:

$$\frac{\partial}{\partial t} \sim \omega \sim \mathbf{v}_E \cdot \nabla \sim \frac{c_s}{L_\perp} \ll \Omega_{ci} \ .$$

  Practically, it is assumed $k^2\rho_s^2 \approx 0.1$ which yields $\rho_s/L_\perp \ll k\rho_s/2\pi \approx 0.05$. Finite Larmor radius effects are retained up to $k^2\rho_s^2$; electron Larmor radius effects are neglected.

3.3 The Braginskii equations

The most convenient and common way to study heat transport in tokamaks is the fluid approach. This method allows in particular to define measurable quantities for the heat transport analysis and diagnose the energy confinement capability of a plasma.
The fluid equations as derived by Braginskii (see [9]) are the moments of the Vlasov equation

$$\frac{\partial f_j}{\partial t} + \mathbf{w} \cdot \nabla f_j + \frac{e_j}{m_j} (\mathbf{E} + \mathbf{w} \times \mathbf{B}) \cdot \frac{\partial f_j}{\partial \mathbf{w}} = C_j + S_j \tag{3.3}$$

where C_j is the Coulomb collision operator and S_j an external particle source. Taking the zeroth, first and second moment we obtain:

Quantity	Definition	Physical meaning
n_j	$\int d^3\mathbf{w} f_j$	Particle density
$\mathbf{v}_j$	$\int d^3\mathbf{w} f_j \mathbf{w}/n_j$	Fluid velocity
S_{nj}	$\int d^3\mathbf{w} S_j$	Particle source
$\mathbf{F}_j$	$\int d^3\mathbf{w} m_j \mathbf{w} C_j\left(f_j\right)$	Collisional momentum
p_j	$\int d^3\mathbf{w}\left(\frac{m_j\lvert\mathbf{w}-\mathbf{v}_j\rvert^2}{3}\right) f_j$	Plasma pressure
π_j	$\int d^3\mathbf{w} m_j f_j\left(\mathbf{w}-\mathbf{v}_j\right)\left(\mathbf{w}-\mathbf{v}_j\right) - p_j \boldsymbol{I}$	Stress tensor
$\mathbf{q}_j$	$\int d^3\mathbf{w}\left(\mathbf{w}-\mathbf{v}_j\right) \times \left(\frac{m_j}{2}\lvert\mathbf{w}-\mathbf{v}_j\rvert^2\right) f_j$	Heat flux
Q_j	$\int d^3\mathbf{w} \frac{1}{2} m_j \lvert\mathbf{w}-\mathbf{v}_j\rvert^2 C_j\left(f_j\right)$	Collisional heat exchange rate
S_{Ej}	$\int d^3\mathbf{w} \frac{m_j w^2}{2} S_j$	Energy from particle source

Table 3.1: Definition of the fluids quantities. The label refers to the plasma species.

- Continuity equation:

$$\frac{\partial n_j}{\partial t} + \nabla \cdot \left(n_j \mathbf{v}_j\right) = S_{nj} \tag{3.4}$$

- Momentum balance equation:

$$m_j n_j \frac{\partial \mathbf{v}_j}{\partial t} + m_j n_j \mathbf{v}_j \cdot \nabla \mathbf{v}_j = n_j q_j \left(\mathbf{E} + \mathbf{v}_j \times \mathbf{B}\right) + \mathbf{F}_j - \nabla p_j - \nabla \cdot \pi_j \tag{3.5}$$

- Energy equation:

$$\begin{aligned} &\frac{\partial}{\partial t}\left(\frac{1}{2} m_j n_j v_j^2 + \frac{3}{2} p_j\right) + \nabla \cdot \left[\left(\frac{1}{2} m_j n_j v_j^2 + \frac{5}{2} p_j\right) \mathbf{v}_j + \pi_j \cdot \mathbf{v}_j + \mathbf{q}_j\right] = \\ &\left(q_j n_j \mathbf{E} + \mathbf{F}_j\right) \cdot \mathbf{v}_j + Q_j + S_{Ej} \end{aligned} \tag{3.6}$$

where the mentioned quantities are defined in Table 3.1. Subtracting from equation 3.6 the equation 3.4 times $m v_j^2/2$ and 3.5 times $\mathbf{v}_j \cdot$ one obtains:

$$\frac{3}{2}\left(\frac{\partial}{\partial t} + \mathbf{v}_j \cdot \nabla\right) p_j + \frac{5}{2} p_j \nabla \cdot \mathbf{v}_j + \pi : \nabla \mathbf{v}_j + \nabla \cdot \mathbf{q}_j = S_{Qj} \tag{3.7}$$

where the source term S_{Qj} is the sum of different contributions: $S_{Qj} = Q_j + S_{Ej} - m_j v_j^2 S_{nj}/2$.

3.4 Derivation of the dispersion relation

The starting point for the Weiland model is the Braginskii set of equations 3.4, 3.5 and 3.6, neglecting sources (S_{nj} and S_{Ej}) and Coulombian collision terms (Q_j and $\mathbf{F}_j$). We multiply the 3.5 times $\frac{1}{m_j n_j}\mathbf{e}_\parallel \times$ and make use of the vector identity (2) from [27]. Furthermore,

we assume the electrostatic approximation $\mathbf{B} = B_0\mathbf{e}_\parallel$.

$$\frac{d}{dt}\mathbf{e}_\parallel \times \mathbf{v}_j = \frac{q_j}{m_j}\left\{\mathbf{e}_\parallel \times \mathbf{E} + B_0\left[\mathbf{v}_j\left(\mathbf{e}_\parallel \cdot \mathbf{e}_\parallel\right) - \mathbf{e}_\parallel\left(\mathbf{e}_\parallel \cdot \mathbf{v}_j\right)\right]\right\} - \frac{1}{m_j n_j}\mathbf{e}_\parallel \times (\nabla p_j + \nabla \cdot \pi_j) \ . \tag{3.8}$$

Since $\mathbf{v}_j\left(\mathbf{e}_\parallel \cdot \mathbf{e}_\parallel\right) - \mathbf{e}_\parallel\left(\mathbf{e}_\parallel \cdot \mathbf{v}_j\right)$ is $\mathbf{v}_{\perp j}$, dividing by Ω_{ci} we find (see [25], (2.2)):

$$\mathbf{v}_{\perp j} = \frac{1}{B_0}\left(\mathbf{E} \times \mathbf{e}_\parallel\right) + \frac{1}{\Omega_{cj}}\frac{d}{dt}\left(\mathbf{e}_\parallel \times \mathbf{v}_j\right) + \frac{1}{q_j n_j B_0}\mathbf{e}_\parallel \times (\nabla p_j + \nabla \cdot \pi_j) = \mathbf{v}_E + \mathbf{v}_{pj} + \mathbf{v}_{\star j} + \mathbf{v}_{\pi j} \ . \tag{3.9}$$

where $\mathbf{v}_E$, $\mathbf{v}_{pj}$, $\mathbf{v}_{\star j}$ and $\mathbf{v}_{\pi j}$ are the drift velocities defined in Table 2.1. The second term actually reduces to $\mathbf{v}_{\pi j}$ under the assumption that the electrostatic drift velocity $\mathbf{v}_E$ is the main contribution to $\mathbf{v}_{\perp j}$. The ion continuity equation then reads:

$$\frac{\partial n_i}{\partial t} = -\nabla \cdot (n_i \mathbf{v}_{\star i}) - \nabla \cdot (n_i \mathbf{v}_E) - \nabla \cdot (n_i \mathbf{v}_{pi}) - \nabla \cdot (n_i \mathbf{v}_{\pi i}) - \nabla \cdot \left(n_i \mathbf{v}_\parallel\right) \ . \tag{3.10}$$

In the following derivation we neglect for simplicity the parallel ion motion term $\nabla \cdot \left(n_i \mathbf{v}_\parallel\right)$, although the Weiland model treats it in the strong ballooning approximation [28]. An estimate of this quantity can be found in appendix B.2. We introduce in the continuity equation an harmonic perturbation $\tilde{n}_j = n_j - n_j^{(0)}$ by defining

$$\tilde{n}_j = \delta n_j e^{i(\mathbf{k}\cdot\mathbf{r} - \omega t)} \tag{3.11}$$

The frequency is in general complex, $\omega = \omega_r + i\gamma$. In this convention, an instability occurs if $\gamma > 0$. The linearised first order equation has the form:

$$\frac{\partial \tilde{n}_i}{\partial t} = -n_i^{(0)} \nabla \cdot \tilde{\mathbf{v}}_{drift} - \nabla n_i^{(0)} \cdot \tilde{\mathbf{v}}_{drift} - \tilde{n}_i \nabla \cdot \mathbf{v}_{drift}^{(0)} - \nabla \tilde{n}_i \cdot \mathbf{v}_{drift}^{(0)} \ . \tag{3.12}$$

- $\mathbf{v}_{Di}$ is no fluid drift, so it does not appear in the fluid equations and does not contribute directly to $\nabla \cdot (n\mathbf{v}_i)$.
- $\nabla \tilde{n}_i / \nabla n_i$ can be assumed to be order 1 at the saturation, but in the linear case it is arbitrarily small.
- The products $\tilde{n}_i \nabla \cdot \mathbf{v}_E^{(0)}$ and $\nabla \tilde{n}_i \cdot \mathbf{v}_E^{(0)}$ should be considered, but we assume that there is no background $\mathbf{E}$. In the following, we write $\mathbf{v}_E$ instead of $\delta \mathbf{v}_E$ for simplicity.

So equation 3.12 reduces to

$$-i\omega\delta n_i = -\nabla n_i^{(o)} \cdot \mathbf{v}_E - n_i^{(o)} \nabla \cdot \mathbf{v}_E + First\ order\ \left\{-\nabla \cdot \left[n_i\left(\mathbf{v}_{pi} + \mathbf{v}_{\pi i}\right)\right] - \nabla \cdot (n_i \mathbf{v}_{\star i})\right\} \ . \tag{3.13}$$

In appendix B.3 all first order contributions are evaluated using the assumptions mentioned in Section 3.2. In this way, equations for the density perturbations of ions, trapped

electrons and passing electrons are obtained. As the equations B.68 and B.69 show, the frequencies are of the order of the curvature drift frequency ω_{De}, therefore it makes sense to normalise them to this physical quantity: $\hat{\omega} = \omega/\omega_{De}$, $\hat{N}_j = N_j/\omega_{De}^2$. The dispersion relation results from quasi-neutrality:

$$\hat{N}_i \hat{N}_e \epsilon_n \frac{T_e}{e\phi} \left[\frac{\delta n_i}{n_i} - f_t \frac{\delta n_{et}}{n_{et}} - (1 - f_t) \frac{\delta n_{ep}}{n_{ep}} \right] = 0 \ . \tag{3.14}$$

Substituting the results B.68, B.69 and 3.2 the dependence of the dispersion relation on the physical plasma parameters can be made explicit:

$$\begin{aligned} &\hat{N}_e \left[-\hat{\omega}^2 k^2 \rho_s^2 \epsilon_n + \hat{\omega} \left(1 - \epsilon_n - k^2 \rho_s^2 \frac{5}{3} \frac{\epsilon_n}{\tau} - k^2 \rho_s^2 \frac{1 + \eta_i}{\tau} \right) + \right. \\ &\left. - \frac{1}{\tau} \left(\eta_i - \frac{7}{3} + \frac{5}{3} \epsilon_n \right) - k^2 \rho_s^2 \frac{5}{3\tau^2} (1 + \eta_i) \right] = \\ &= (1 - f_t) \hat{N}_i \hat{N}_e \epsilon_n + f_t \hat{N}_i \left[\hat{\omega} (1 - \epsilon_n) + \left(\eta_e - \frac{7}{3} + \frac{5}{3} \epsilon_n \right) \right] \ . \end{aligned} \tag{3.15}$$

The equation is a fourth degree polynomial in ω, which allows up to two roots with positive imaginary part. In terms of physics, this means that there are up to two unstable modes.

If ϵ_n is around 1 ($L_n \approx R/2$), the modes are rather independent and propagate in opposite directions. The dispersion relation is then well approximated neglecting the part with the larger N_j (see [25], par. 5.11.2). If $N_i \gg N_e$, the TEM becomes decoupled and dominates the dispersion relation. This is the case for frequencies close to the resonant values:

$$\omega = \omega_{De} \frac{5 \pm \sqrt{10}}{3} \ . \tag{3.16}$$

Since usually $|\omega| > |\omega_{Dj}|$, the condition 3.16 can be satisfied if $|\omega_{De}| > |\omega_{Di}|$, i. e. for $T_e > T_i$. The formulas for the TEM stability threshold and the growth rate of the mode assume the simple form:

$$\hat{\omega}^2 (1 - f_t) \epsilon_n + \hat{\omega} \left(-\frac{10}{3} \epsilon_n + f_t + \frac{7}{3} f_t \epsilon_n \right) + \frac{5}{3} \epsilon_n + f_t \left(\eta_e - \frac{7}{3} \right) = 0 \ . \tag{3.17}$$

If there is an unstable root, the imaginary part of the solution is

$$\begin{aligned} \hat{\gamma} &= \sqrt{\frac{f_t}{\epsilon_n (1 - f_t)}} \sqrt{\eta_e - \eta_{th}} \\ \eta_{th} &= \frac{10}{9} \epsilon_n \frac{1 - f_t}{f_t} + \frac{f_t}{1 - f_t} \frac{1}{4\epsilon_n} (1 - \epsilon_n)^2 + \frac{2}{3} \ . \end{aligned} \tag{3.18}$$

Reminding thar $\eta_e/\epsilon_n = R/2L_{T_e}$, the stability condition can be expressed in terms of the temperature gradient length:

$$\hat{\gamma} = \sqrt{\frac{f_t}{2 (1 - f_t)} \left(\frac{R}{L_{T_e}} - \frac{R}{L_{T_{cr}}} \right)}$$

$$\frac{R}{L_{T_{cr}}} = \frac{20}{9}\frac{1-f_t}{f_t} + \frac{f_t}{2\,(1-f_t)}\left(\frac{R}{2L_n} - 1\right)^2 + \frac{2}{3}\frac{R}{L_n}\,. \tag{3.19}$$

The critical threshold of the TEM as a function of R/L_n is illustrated in Fig. 3.1 for different radii and hence for different trapped electrons fraction. This approximated formula will be used for comparison with the experimental inverse gradient length in Section 5.8.

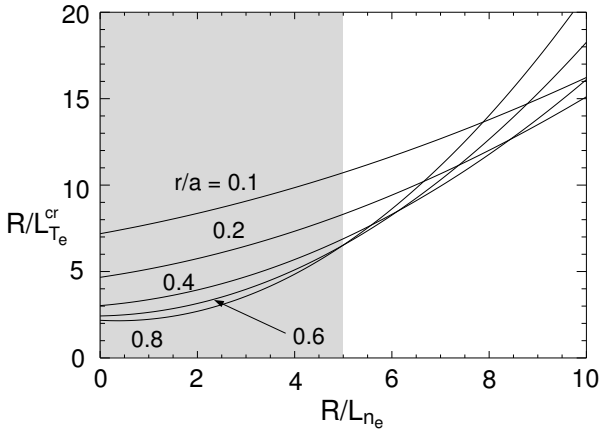

Figure 3.1: Critical threshold for R/L_{T_e} as a function of R/L_{n_e}, for $r/a = 0.1$, 0.2, 0.4, 0.6 and 0.8. The shaded region is the common range of measured R/L_{n_e} values.

3.5 Quasi-linear transport

The quasi linear particle and heat fluxes arising from the turbulence are the average over harmonic time and space variations of the fluctuation. This points out the importance of the phase shift between the radial electrostatic drift and the density or temperature perturbation. The contribution of all instabilities should be summed, but the quasi linear approach uses the simplifying assumption that transport is determined by the fastest growing mode. In addition, the model is local and thus neglects the coupling between different harmonics due to plasma inhomogeneities.

$$\Gamma = < \tilde{n} v_E >$$
$$\Gamma_{T_j} = < \tilde{T}_j \mathbf{v}_E >$$

The corresponding diffusion coefficients come from the Fick's and Fourier's laws:

$$D = -\frac{\Gamma}{\nabla n}$$

$$\chi_i = \frac{\Gamma_{T_i}}{\nabla T_i}$$
$$\chi_e = \frac{n_{et}\Gamma_{T_e}}{n_e \nabla T_e} \tag{3.20}$$

Actually, the adiabatic electrons do not contribute to particle transport, because v_E is always phase shifted by $\pi/2$ with respect to δn_{ep} and therefore integration over a period returns zero (they are normal to each other). The quantities $\frac{\delta n_i}{n_i}$ and $\frac{\delta n_e}{n_e}$ are given by the B.68, B.69 and 3.2. In an inhomogeneous plasma, the amplitude of the modes has an additional slow space variation:

$$\tilde{T} = \frac{1}{2}\left[\delta T\left(x\right) e^{-i\left(\omega t - \mathbf{k}\cdot\mathbf{r}\right)} + \ C.\,C.\right] \ . \tag{3.21}$$

The heat flux results to be

$$\Gamma_{T_j} = \frac{1}{2}\left(\sum_k \delta T_j \bar{v}_E + CC\right) \tag{3.22}$$

where CC means "complex conjugate". The products $\delta T v_E e^{-2i\left(\omega t - \mathbf{k}\cdot\mathbf{r}\right)}$ and $\bar{\delta T}\bar{v}_E e^{2i\left(\omega t - \mathbf{k}\cdot\mathbf{r}\right)}$ vanish in the time average.

We focus on the contribution of a single mode to transport. Saturation is reached when the dominant non linearity (the convective $E \times B$ one) balances the linear growth: from the continuity equation for instance

$$\frac{\partial n}{\partial t} \sim \mathbf{v}_E \cdot \nabla n \tag{3.23}$$
$$\gamma \delta n e^{i\mathbf{k}\cdot\mathbf{r}} = \mathbf{v}_E \cdot \nabla\left(\delta n e^{i\mathbf{k}\cdot\mathbf{r}}\right) \tag{3.24}$$

The gradient can be expressed as the characteristic inverse length in the radial direction, i. e. k_x, which is assumed to be approximately equal to k_y when the instability saturates (isotropic turbulence), i. e.

$$v_E = -i\frac{\gamma}{k_x} \ .$$

Substituting the relation B.2 yields

$$\omega_{\star e}\frac{e\phi}{T_e} = i\frac{v_E}{L_n} = \frac{\gamma}{k_x L_n} \ .$$

The ion heat flux can be now evaluated as

$$\Gamma_{T_i} \approx \frac{1}{2}\left(i\frac{\gamma}{k_x}\delta T_i + CC\right) = Re\left(i\frac{\gamma}{k_x}\delta T_i\right) \ . \tag{3.25}$$

Due to quasi neutrality, according to equations B.49, B.69 and 3.2 the temperature perturbation is:

$$\delta T_i = \frac{T_i}{\omega - \omega_{Di}5/3}\frac{\gamma}{k_x L_n}\left[\frac{2}{3}\frac{\omega}{\omega_{\star e}}\left(1 - f_t + f_t A_e\right) + \eta_i - \frac{2}{3}\right] \ ,$$

where

$$A_e = \frac{1}{\epsilon_n \hat{N}_e}\left[\hat{\omega}\left(1-\epsilon_n\right) + \left(\eta_e - \frac{7}{3} + \frac{5}{3}\epsilon_n\right)\right] \ . \tag{3.26}$$

Substituting this result in 3.25, after some algebra (see appendix B.4) the quasi linear heat diffusivity results to be:

$$\chi_i = \frac{1}{\eta_i}\left[\eta_i - \frac{2}{3} - \left(1-f_t\right)\frac{10}{9}\frac{\epsilon_n}{\tau} - \frac{2}{3}f_t\Delta_i\right]\frac{\hat{\gamma}^3\omega_{De}/k_x^2}{\left(\hat{\omega}_r + 5/3\tau\right)^2 + \hat{\gamma}^2} \ , \tag{3.27}$$

$$\Delta_i = \frac{1}{\hat{N}}\left\{|\hat{\omega}|^2\left[|\hat{\omega}|^2\left(\epsilon_n - 1\right) + \hat{\omega}_r\left(\frac{14}{3} - 2\eta_e - \frac{10}{3}\epsilon_n\right) + \frac{5}{3}\left(-\frac{11}{3} + 2\eta_e + \frac{7}{3}\epsilon_n\right) + \right.\right.$$
$$\left.\left. -\frac{5}{3\tau}\left(1 + \eta_e - \frac{5}{3}\epsilon_n\right)\right] + \frac{50}{9\tau}\left(1-\epsilon_n\right)\hat{\omega}_r + \frac{25}{9\tau}\left(\eta_e - \frac{7}{3} + \frac{5}{3}\epsilon_n\right)\right\} \ , \tag{3.28}$$

where $\hat{N}$ is

$$\hat{N} = |\hat{N}_e|^2 = \left(\hat{\omega}_r^2 - \hat{\gamma}^2 - \frac{10}{3}\hat{\omega}_r + \frac{5}{3}\right)^2 + 4\left(\hat{\omega}_r\hat{\gamma} - \frac{5}{3}\hat{\gamma}\right)^2 \ . \tag{3.29}$$

The expression for χ_e is slightly simpler, since only the trapped electrons contribute to transport: similarly to the ions' case

$$\delta T_e = \frac{T_e}{\omega - 5\omega_{De}/3}\frac{\gamma}{k_x L_n}\left[\frac{2}{3}\frac{\omega}{\omega_{\star e}}A_e + \eta_e - \frac{2}{3}\right] \ . \tag{3.30}$$

The quasi linear electron thermal diffusivity has the form:

$$\chi_e = \frac{1}{\eta_e}f_t\left(\eta_e - \frac{2}{3} - \frac{2}{3}\Delta_e\right)\frac{\hat{\gamma}^3\omega_{De}/k_x^2}{\left(\hat{\omega}_r - 5/3\right)^2 + \hat{\gamma}^2} \ . \tag{3.31}$$

The quantity Δ_e is almost identical to Δ_i, except that ω_{De} replaces ω_{Di} in the 3.28 and therefore factors $-1/\tau$ vanish, giving:

$$\Delta_e = \frac{1}{\hat{N}}\left\{|\hat{\omega}|^2\left[|\hat{\omega}|^2\left(\epsilon_n - 1\right) + \hat{\omega}_r\left(\frac{14}{3} - 2\eta_e - \frac{10}{3}\epsilon_n\right) + \frac{5}{3}\left(-\frac{8}{3} + 3\eta_e + \frac{2}{3}\epsilon_n\right)\right] + \right.$$
$$\left. -\frac{50}{9}\left(1-\epsilon_n\right)\hat{\omega}_r - \frac{25}{9}\left(\eta_e - \frac{7}{3} + \frac{5}{3}\epsilon_n\right)\right\} \ . \tag{3.32}$$

For particles we need to determine the density perturbation; taking for instance the trapped electron dynamics:

$$\delta n_{et} = f_t n_e \frac{e\phi}{T_e}A_e \ , \tag{3.33}$$

$$\Gamma = \frac{1}{2}\left(\bar{v}_E\delta n_{et} + CC\right) = Re\left(i\frac{\gamma}{k_x}\delta n_{et}\right) = -Im\left(\frac{\gamma}{k_x}f_t n_e\frac{e\phi}{T_e}A_e\right) \ . \tag{3.34}$$

As usual we consider only the fastest mode:

$$D = -\frac{\Gamma}{\nabla n} = Im\left(\frac{\gamma}{k_x}f_t\frac{n_e}{\nabla n_e}\frac{e\phi}{T_e}A_e\right) = Im\left(-\frac{\gamma^2}{k_x^2\omega_{\star e}}f_t A_e\right) =$$
$$= Im\left(-\frac{\hat{\gamma}^2\omega_{De}}{k_x^2}f_t\epsilon_n A_e\right) = -\frac{\hat{\gamma}^3\omega_{De}}{k_x^2}f_t\Delta_n \ , \tag{3.35}$$

where Δ_n can be immediately derived from equation B.76:

$$\Delta_n = \frac{1}{\hat{N}}\left[|\hat{\omega}|^2(\epsilon_n - 1) + \hat{\omega}_r\left(\frac{14}{3} - 2\eta_e - \frac{10}{3}\epsilon_n\right) + \frac{5}{3}\left(-\frac{11}{3} + 2\eta_e + \frac{7}{3}\epsilon_n\right)\right] . \tag{3.36}$$

3.6 Transport coefficients

With the expressions 3.27, 3.31 and 3.35 the fluxes are fully determined, through the effective diffusivities χ_i, χ_e and D. However, it is numerically unconvenient to divide by gradients, which can become close to zero during the profile evolution, as for instance after a sawtooth crash. The transport matrix in the transport code ASTRA allows by default to split the contribution to the fluxes from the different driving gradients.
The transport equation can be written in the matrix form

$$\begin{pmatrix} q_i/n_iT_i \\ q_e/n_eT_e \\ \Gamma_e/n_e \end{pmatrix} = -\begin{pmatrix} a_{11} & a_{12} & a_{13} \\ a_{21} & a_{22} & a_{23} \\ a_{31} & a_{32} & a_{33} \end{pmatrix}\begin{pmatrix} \nabla T_i/T_i \\ \nabla T_e/T_e \\ \nabla n_e/n_e \end{pmatrix} + \begin{pmatrix} U_i \\ U_e \\ U_n \end{pmatrix} , \tag{3.37}$$

where U_i, U_e and U_n have the meaning of anomalous pinch velocities. In a_{13} we neglect ∇Z_{eff} and assume $\nabla n_i/n_i \approx \nabla n_e/n_e$. Defining the useful coefficients

$$c_1 = \frac{\hat{\gamma}^3\omega_{De}}{k_x^2}$$

$$c_2 = \frac{c_1 f_t}{(\omega_r - 5/3)^2 + \hat{\gamma}^2}$$

the transport coefficients derived in B.4.1 read:

$$\begin{cases} a_{11} = \dfrac{c_1}{(\omega_r + 5/3\tau)^2 + \hat{\gamma}^2} \\ a_{12} = -a_{11}\dfrac{2}{3}\dfrac{f_t}{\hat{N}}\left[|\hat{\omega}|^2\left(-2\hat{\omega}_r + \dfrac{10}{3} - \dfrac{5}{3\tau}\right) + \dfrac{25}{9\tau}\right] \\ a_{13} = -a_{11}\dfrac{2}{3}\left[1 + \dfrac{f_t}{\hat{N}}|\hat{\omega}|^2\left(-|\hat{\omega}|^2 + \dfrac{14}{3}\hat{\omega}_r - \dfrac{55}{9} - \dfrac{5}{3\tau}\right) + \dfrac{f_t}{\hat{N}}\dfrac{1}{\tau}\left(\dfrac{50}{9}\hat{\omega}_r - \dfrac{175}{27}\right)\right] \\ U_i = -a_{11}\dfrac{4}{3R}\left[\dfrac{5}{3\tau}(1 - f_t) + \dfrac{f_t}{\hat{N}}|\hat{\omega}|^2\left(|\hat{\omega}|^2 - \dfrac{10}{3}\hat{\omega}_r + \dfrac{35}{9} + \dfrac{25}{9\tau}\right) + \dfrac{f_t}{\hat{N}}\dfrac{1}{\tau}\left(-\dfrac{50}{9}\hat{\omega}_r + \dfrac{125}{27}\right)\right] \end{cases} \tag{3.38}$$

$$\begin{cases} a_{21} = 0 \\ a_{22} = c_2\left\{1 - \dfrac{2}{3\hat{N}}\left[|\hat{\omega}|^2(-2\hat{\omega}_r + 5) - \dfrac{25}{9}\right]\right\} \\ a_{23} = -c_2\dfrac{2}{3}\left[1 - \dfrac{|\hat{\omega}|^2}{\hat{N}}\left(-|\hat{\omega}|^2 + \dfrac{14}{3}\hat{\omega}_r - \dfrac{40}{9}\right) + \dfrac{1}{\hat{N}}\left(-\dfrac{50}{9}\hat{\omega}_r + \dfrac{175}{27}\right)\right] \\ U_e = -c_2\dfrac{4}{3R}\dfrac{1}{\hat{N}}\left[|\hat{\omega}|^2\left(|\hat{\omega}|^2 - \dfrac{10}{3}\hat{\omega}_r + \dfrac{10}{9}\right) + \dfrac{50}{9}\hat{\omega}_r - \dfrac{125}{27}\right] \end{cases} \tag{3.39}$$

$$\begin{cases} a_{31} = 0 \\ a_{32} = -c_1 \dfrac{f_t}{\hat{N}} \left(-2\hat{\omega}_r + \dfrac{10}{3} \right) \\ a_{33} = -c_1 \dfrac{f_t}{\hat{N}} \left(-|\hat{\omega}|^2 + \dfrac{14}{3}\hat{\omega}_r - \dfrac{55}{9} \right) \\ U_n = -c_1 \dfrac{f_t}{\hat{N}} \dfrac{2}{R} \left(|\hat{\omega}|^2 - \dfrac{10}{3}\hat{\omega}_r + \dfrac{35}{9} \right) \end{cases} \tag{3.40}$$

It is interesting to note that all transport coefficients contain the factor

$$\frac{\omega_{De}}{k_x^2} \approx 2\frac{k_\perp \rho_s c_s}{k_\perp^2 L_B} = 2\frac{\rho_s^2 c_s}{\rho_s k_\perp L_B} = 2\frac{T_e^{1.5} m_i^{-1.5}}{\Omega_{ci}^2 \rho_s k_\perp L_B} \approx 2\frac{T_e^{1.5} m_i^{0.5}}{e^2 B^2 \rho_s k_\perp R} \ .$$

Assuming that $\rho_s k_\perp$ is constant, this factor contains a significant temperature dependence. The physics consequence is a steeper increase of transport beyond the critical threshold for higher T_e and consequently stronger profile stiffness.

Chapter 4

Ion and electron heat transport in standard H-mode discharges

Per aspera ad ASTRA

In this chapter we apply the models presented in chapter 2 to ASDEX Upgrade H-mode discharges heated with Neutral Beam Injection (NBI). For these experiments the temperature profiles have been observed to be stiff [29] [30] [31], their gradient length being close to a critical threshold, particularly for T_i. The profile shape tends to remain the same from discharge to discharge (profile resilience) and the ratio between core and pedestal temperature is constant, regardless of the heat absorption profile.
Our interest is to test ITG physics, with particular focus on profile stiffness, so we try to isolate this feature from other physics effects. For this purpose we have selected a database in which only one plasma parameter is varied from a given standard set of parameters. Additional discharges featuring also Electron Cyclotron Heating (ECH) are modelled, to check the predictions when the electron heat flux becomes relevant and to look at the influence of the ratio T_e/T_i on both ion and electron transport.
The comparison between theory based models and experimental data allows to order and interprete the data. Besides, it makes possible to evaluate the predictive capability of the models, finding their ranges of applicability and judging some of their assumptions.

4.1 Diagnostic systems

The tokamak ASDEX Upgrade is equipped with a comprehensive set of diagnostic systems, covering all the measurements required of a modern tokamak. For our purposes, plasma equilibrium as well as several experimental profiles have to be diagnosed, partly for comparison with the theoretical predictions, partly as input for the simulations which

are not fully self-consistent. In particular, ion and electron temperature and density profiles measurements are necessary, as well as toroidal velocity (v_{tor}), effective charge (Z_{eff}) and radiated power. Also scalar parameters are required, such as plasma current, toroidal magnetic field, NBI power for each source and geometric parameters like elongation and triangularity.
The ion temperature profile, the plasma toroidal rotation and the effective charge (Z_{eff}) are measured with the Charge eXchange Recombination Spectroscopy (CXRS) [32]. The toroidal CXRS diagnostic has sight-lines lying on the equatorial plane of ASDEX Upgrade, measuring ion temperature at 16 radial positions in the plasma. The spatial resolution is 1-2 cm, depending on the sight-line: the best resolution is obtained at half radius, whereas in the plasma center and at the edge the uncertainty is larger. The errors are moderate in the case of ion temperature, but are relevant for Z_{eff}, which influences the simulations since the models depend on Z_{eff}, as discussed in section 2.4.5. The basic mechanism of the CXRS diagnostic is the measurement of the Doppler shifted and broadened carbon recombination, which is detectable only in presence of NBI.
Electron temperature profiles measurements are performed with the Electron Cyclotron Emission (ECE) system [33]. The ECE in the millimetre wavelength range is measured by a heterodyne radiometer system, which detects the second harmonic of the X-mode electron cyclotron radiation. The system has 60 output channels, allowing a fine spatial coverage of the T_e profile measurement; the spatial resolution is about 5-10 mm, the sampling rate 31.25 kHz.
Electron density is diagnosed by the combination of line-averaged interferometry and Lithium-beam diagnostics [34]. The Mach-Zehnder interferometer uses a DCN laser (wavelength 195 μm) as light source. The system has 8 output channels, corresponding to 5 horizontal and 3 vertical sightlines. The signal is then Abel inverted, delivering a density profile.
Auxiliary heating in the selected discharges is always supplied by Neutral Beam Injection (NBI), usually with 60 kV beams, but in some cases a part of the beam is accelerated with 93 kV.

4.2 NBI heated H-mode discharges

A database of 70 ASDEX Upgrade deuterium discharges with low triangularity ($\delta < 0.2$) is established. They are H-mode discharges, with low to moderate plasma density and no Internal Transport Barriers (ITBs). In Table 4.1 the parameters of the discharges are listed; the experimental data are grouped into a power, a density and a current scan. In each considered scan two quantities are kept fixed to the standard values, which are 5 MW for the NBI heating power, 1 MA for the total plasma current and 6 to 8 $\times$ 10^{19}

m^{-3} for the plasma density. The third quantity is varied over the widest range possible. In this way, different physics effects can be distinguished and eventually be related to profile stiffness. The current scan influences the pedestal pressure through a MHD limit, the heating power affects the heat flux in the plasma core as well as the pedestal pressure, a density variation changes the boundary temperature leaving pressure unchanged.

Scan	P_{NBI} (MW)	I_{pl} (MA)	$\overline{n}_e$ (10^{19} m^{-3})
P_{NBI}	1.8	0.8	6.18
	2.5	1.0	7.85
	5.0	1.0	7.13
	7.5	1.0	6.61
	10.0	1.0	7.31
	12.5	1.0	7.04
I_{pl}	5.0	0.4	$3.15 \leq n_e \leq 4.34$
	5.0	0.6	4.60
	5.0	0.8	4.98
	5.0	1.0	7.13
	5.0	1.2	6.55, 7.13
n_e	5.0	1.0	$3.75 \leq n_e \leq 8.07$

Table 4.1: Parameters of the selected ASDEX Upgrade discharges.

4.2.1 Discharges with NBI and ECH

An additional set of 7 discharges with both NBI and ECH are modelled to study the case where the electron heat flux becomes larger and T_e/T_i is somewhat different. Again, the NBI heating power is roughly 5 MW and the plasma current 1 MA. In addition, ECH power is applied varying between 0.8 and 1.6 MW. For a description of the heating scheme and of the ASDEX Upgrade ECH system, see Section 5.1. The plasma density of these discharges is low and rather constant, close to 3.5 10^{19} m^{-3}; in most cases the heat is absorbed close to the magnetic axis. The deposition radii are calculated with a beam tracing technique using the TORBEAM code [35].

P_{ECRH} (MW)	ρ_{dep}	$\overline{n}_e$ (10^{19} m^{-3})
0.8	0.01	3.66
1.2	0.01	3.53
1.2	0.33	3.73
0.8	0.10	3.77
1.6	0.01	3.50
1.2	0.20	3.30
1.6	0.07	3.29

Table 4.2: Parameters of the discharges with both ECH and NBI.

4.3 Experimental results

4.3.1 Ion profile stiffness

The behaviour of the experimental core temperature as a function of the edge value is reported in Fig. 4.1. As edge position $\rho_{tor} = 0.8$ is chosen. In this way we make sure that we exclude from the analysis the pedestal region, where MHD instabilities and other modes, different from ITG, play a significant role. The core experimental temperature is taken at $\rho_{tor} = 0.4$, because further inside the measurement is influenced by sawteeth.

The relation between core and edge T_i is clearly linear. The proportionality is observed for

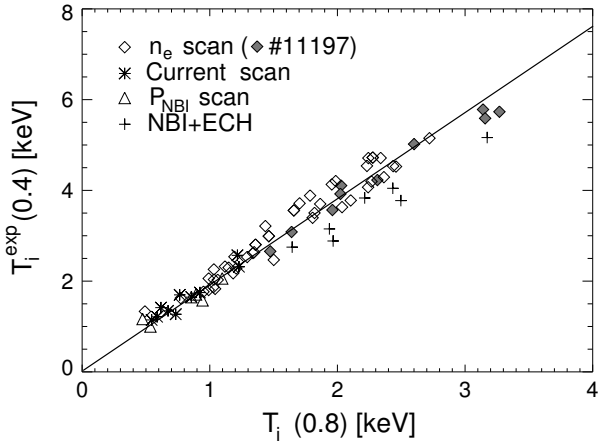

Figure 4.1: Experimental ion core temperature as a function of the edge temperature. Diamonds refer to the density scan, triangles to the power scan and stars to the plasma current scan discharges. The line is a guide for the eye.

all scans performed and with the same factor. This means that the ion temperature profile

is determined by the pedestal value, with the logarithmic temperature gradient $\nabla T_i/T_i$ keeping almost constant from shot to shot. This behaviour is known as profile stiffness (see [36]) and indicates some instability mechanism with a critical threshold in $\nabla T_i/T_i$, which keeps the experimental inverse gradient length close to the critical value as discussed in Section 2.3. Such strict proportionality is, therefore, a clear argument in favour of the ITG instability as the mechanism controlling ion heat transport. Indeed, varying heating power, current or plasma density affect the plasma in different ways, but apparently only the pedestal T_i value influences the core T_i profile. For instance, current variations change the pedestal pressure significantly (factor 4 in the present database), whereas density changes do not. The scan over heating power is an evidence for profile stiffness, because heat fluxes are enhanced by factors up to 5, and with a different distribution between electrons and ions (see Fig. 4.2) but the average gradient lengths remain the same. Another strong argument is provided by the density scan, which covers a very wide

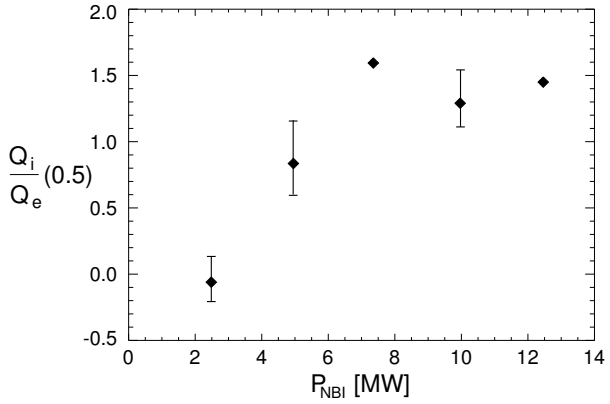

Figure 4.2: Experimental ratio of the ion and electron heat fluxes versus NBI heating power for the power scan discharges.

range of $T_i(0.8)$, thus making the evidence for a linear relation between core and edge T_i reliable. Furthermore, the partition of NBI power between ions and electrons and the penetration of the beams depend strongly on n_e and T_e (which is almost proportional to $1/n_e$, since current and heating power do not change), leading to radical changes in the local ion heat flux (see Fig. 4.4). In spite of that, the gradient lengths remain the same, as the diamonds in Fig. 4.1 show.

Figure 4.1 shows also that in all ECH discharges the average ion temperature gradients are smaller than in the pure NBI shots, although the ion heat flux is larger. Namely, for high T_e the heat exchange with the electrons is reduced and a larger fraction of the NBI power goes to the ions. The trend of ECH experiments is another evidence in favour of a threshold behaviour. The fact that the ratio $T_i(0.4)/T_i(0.8)$ is slightly but systematically

lower than for pure NBI discharges can be explained through the dependence of the instability threshold on the ratio T_e/T_i, which is close to 1 in NBI+ECH discharges and about 1.5 in the case of NBI alone. Such a dependence is treated by all ITG/TEM based transport models and has been discussed in detail in Section 2.4.5.

4.3.2 Electron heat transport

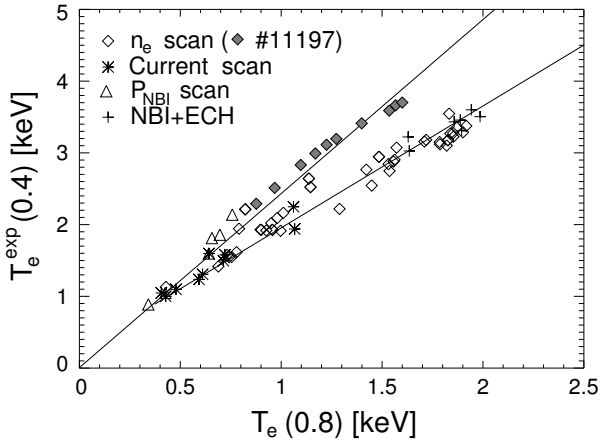

Figure 4.3: Experimental electron core temperature as a function of the edge temperature. Symbols like in Fig. 4.1, in addition full diamonds mark the points related to the discharge #11197. The lines are guides for the eye.

Core electron temperature is proportional to the pedestal value only at low T_e (see Fig. 4.3). Also in this range, however, the proportionality holds strictly only for the power scan (open triangles), so that for these discharges the gradient length remains the same, in agreement with the results obtained with an ECH power scan [14] on ASDEX Upgrade. Interestingly, the power scan discharges exhibit a higher ratio $T_e(0.4)/T_e(0.8)$, showing that it is possible to induce higher gradient lengths by increasing the heating power, at least for low T_e. This indicates that if electron transport is governed by a threshold mechanism, this is not as strict as it has been observed for the ions. In addition, already for $T_e > 0.7$ keV the plot of core versus pedestal T_e tends to spread and to bend towards flatter profiles, with exception of the points related to the discharge #11197, where the short gradient length is likely to be linked to the unusually strong density peaking.
In the selected NBI experiments ion and electron heat fluxes are comparable, with a tendency to be larger for the ions at low density because the electron heating through neutral beams becomes less effective at high T_e (see Fig. 4.4), and because of the reduced heat exchange. The situation changes when ECH is applied too: the electron heat flux gets larger than in the pure NBI case, since the ECH contribution is only partly compensated by the reduction of the heat gained from the ions. Figure 4.3 shows that also ECH

discharges belong to the lower branch in the plot of core versus edge T_e. It appears that the higher ratio $T_e(0.4)/T_e(0.8)$ can be enhanced by increasing the heating power only for low temperatures. This can be understood in terms of weak stiffness, with a model similar to Fig. 1.5. Actually, for higher temperatures, to get a given $\nabla T_e/T_e$ one has to sustain a higher temperature gradient, so that a large amount of power is required. Therefore, for high temperatures the profiles tend to stay closer to the critical threshold.
Also the experimental observation of the discharge #11197 is consistent with a model like in Fig. 1.5. As already discussed, for high temperatures the critical value of $\nabla T_e/T_e$ can hardly be exceeded by raising the heating power. However, the T_e profile can become steeper if the critical gradient is raised too, which appears to be the case for strong density peaking. Indeed, the TEM theory predicts a dependence of the stability threshold on the density gradient; in the Weiland model, peaked density profiles act stabilising, as discussed in Section 3.4 (see Fig. 3.1).

In [37] the coupling with the T_i profiles is invoked to explain the proportionality of core

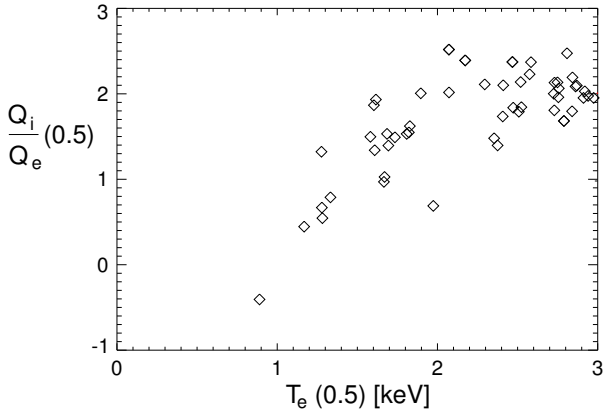

Figure 4.4: Ratio of ion and electron heat fluxes from the power balance analysis for the density scan.

and edge T_e profiles in the high density range. However, in the present database the density is never so high, that electron and ion temperature profiles coincide; moreover, the proportionality factor between $T_e(0.4)$ and $T_e(0.8)$ in the moderate density range is higher than for T_i.

4.3.3 The experimental plasma energy

In ASDEX Upgrade discharges density profiles are generally not stiff [36]. However, in the considered discharges the gradients are moderate in the region of ρ_{tor} between 0.4 and 0.8, with values for $n_e(0.4)/n_e(0.8)$ between 1 and 1.5. Therefore, also the ion pressure

(p_i) profiles resemble stiffness (see Fig. 4.5). The stored plasma energy (see Fig. 4.6) is proportional to the total pedestal pressure ($p(0.8)$) in good approximation for NBI discharges. The energy content reported here is not measured directly, it represents the thermal energy resulting from the integration of the measured pressure profile. The

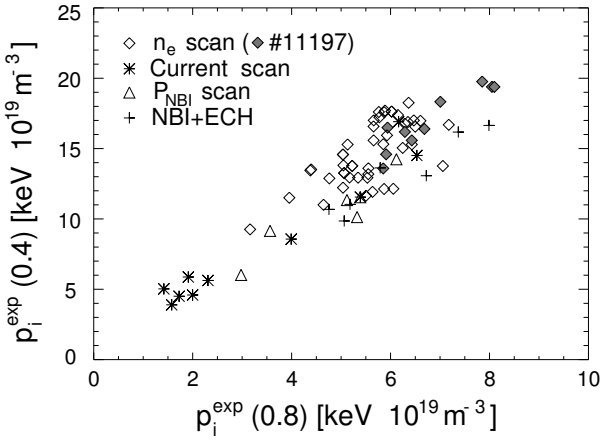

Figure 4.5: Measured core versus pedestal ion pressure. Symbols like in Fig. 4.1.

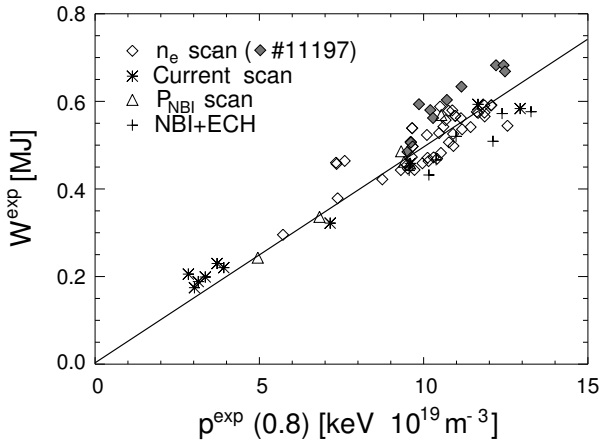

Figure 4.6: Measured total stored energy versus total pedestal pressure. Symbols like in Fig. 4.1. The line is a guide for the eye.

proportionality holds although T_e profiles exhibit no strict linear relation between core and edge. Flatter T_e profiles occur for high T_e discharges, but in that case the ions contribute more to plasma energy, because T_i in this range is almost twice T_e. This is not

the case for ECH+NBI H-mode discharges, which present correspondingly a lower energy content for a given pedestal pressure (see crosses in Fig. 4.6). Furthermore, the moderate density peaking at low densities leads to improved ion confinement. This compensates the energy lack coming from the electron channel. The proportionality between thermal energy and pedestal pressure allows to order the data in terms of global confinement with a simple linear relation. This however does not provide any simple scaling law in terms of engineering parameters because the pedestal pressure itself depends on them.

4.4 Simulation results

4.4.1 The ASTRA code

All simulations are performed with the ASTRA transport code [38], keeping the densities equal to the measured profiles, thus switching off particle transport in the models which contain it, such as the Weiland and the GLF23 models. The experimental temperatures at ρ_{tor}=0.8 are taken as boundary conditions for the calculation, because neither the ITG nor the CDBM physics are expected to describe the pedestal region correctly. Current diffusion is calculated at every time step according to the neoclassical theory [39], the bootstrap current being calculated as in Ref. [40]. Sawteeth are taken into account with a Kadomtsev full reconnection model [41], the period being experimentally determined. Measured as well as modelled temperature profiles are averaged over a sawtooth period. Heat diffusivities are the sum of the neoclassical [42] [43] [44] [45] and turbulent contributions, the latter determined from the considered transport model. The subroutines for each model are provided by the authors, with no free parameters to be adjusted for the modelling. In the Weiland model, the collisions on trapped electrons have been switched off by setting the collision frequency equal to zero.
In all four models the stabilising term arising from the $E \times B$ shear ($\omega_{E\times B}$) is included. The different implementations of this shearing rate are also provided by the authors; the corresponding descriptions can be found in [46], [6] and [47]. The shearing rate is obtained from the measured toroidal velocity, the neoclassical poloidal rotation [48] and the pressure gradient contribution. The latter is calculated from the modelled profiles.
The NBI heating power distribution is implemented as a subroutine in the ASTRA code. The deposition profiles depend on plasma parameters: higher plasma density leads to less penetration of the beams, high T_e values bring most of the power to the ions (see Fig. 4.4). We take the computed temperature profiles as input for the NBI routine for consistency.

4.4.2 Models comparison

With this setup the discharges described in Section 4.2 are modelled through time integration until the steady state is reached. A typical result is shown in Fig. 4.7 for electron and ion temperature profiles, as predicted by the four models. In Fig. 4.7 (a), the inverse

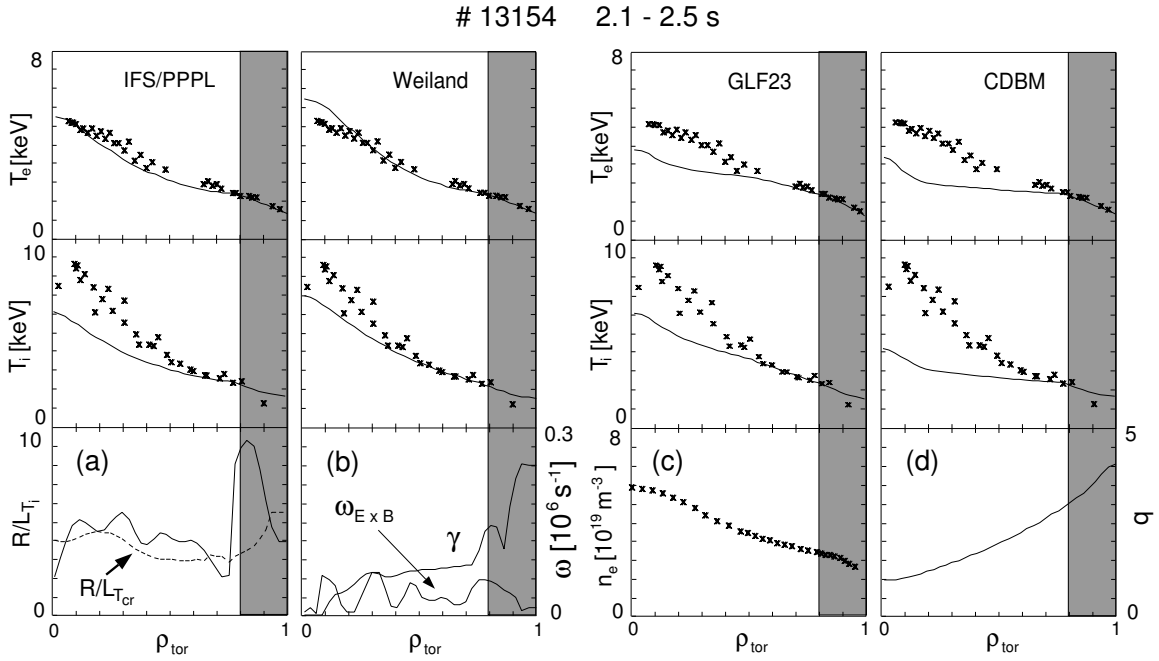

Figure 4.7: Temperature profiles of a typical ASDEX Upgrade H-mode discharge from experiment (points) and from modelling (solid lines). No modelling outside $\rho_{tor} = 0.8$. In the third row: (a) R/L_{T_i} and $R/L_{T_{cr}}$ profiles from the IFS/PPPL model; (b) $\omega_{E\times B}$ and γ from the Weiland model; (c) Experimental density profile (d) q with T_e profile from the CDBM model.

ion temperature gradient length is plotted compared to the critical profile according to the the IFS/PPPL model. In Fig. (b) the growth rate is displayed together with the rotational shearing rate $\omega_{E\times B}$. Figure (c) shows the measured density profile and in (d) the safety factor q is reported from the simulated current diffusion, the T_e profile being taken from the CDBM modelling. Outside ρ_{tor}=0.8 the profiles are not modelled but set equal to the experimental data. The gradient length for the IFS/PPPL model deviates from the critical value in spite of the strong stiffness because the rotational shearing rate $\omega_{E\times B}$ stabilises the ITG around the critical value. Close to the axis the neoclassical transport and the sawteeth allow the gradient length to stay below the critical value.
The plot corresponding to Fig. 4.1 for modelled core and edge T_i is reported in Fig. 4.8.

The ITG models reproduce the experimental data satisfactorily: profile stiffness and weak

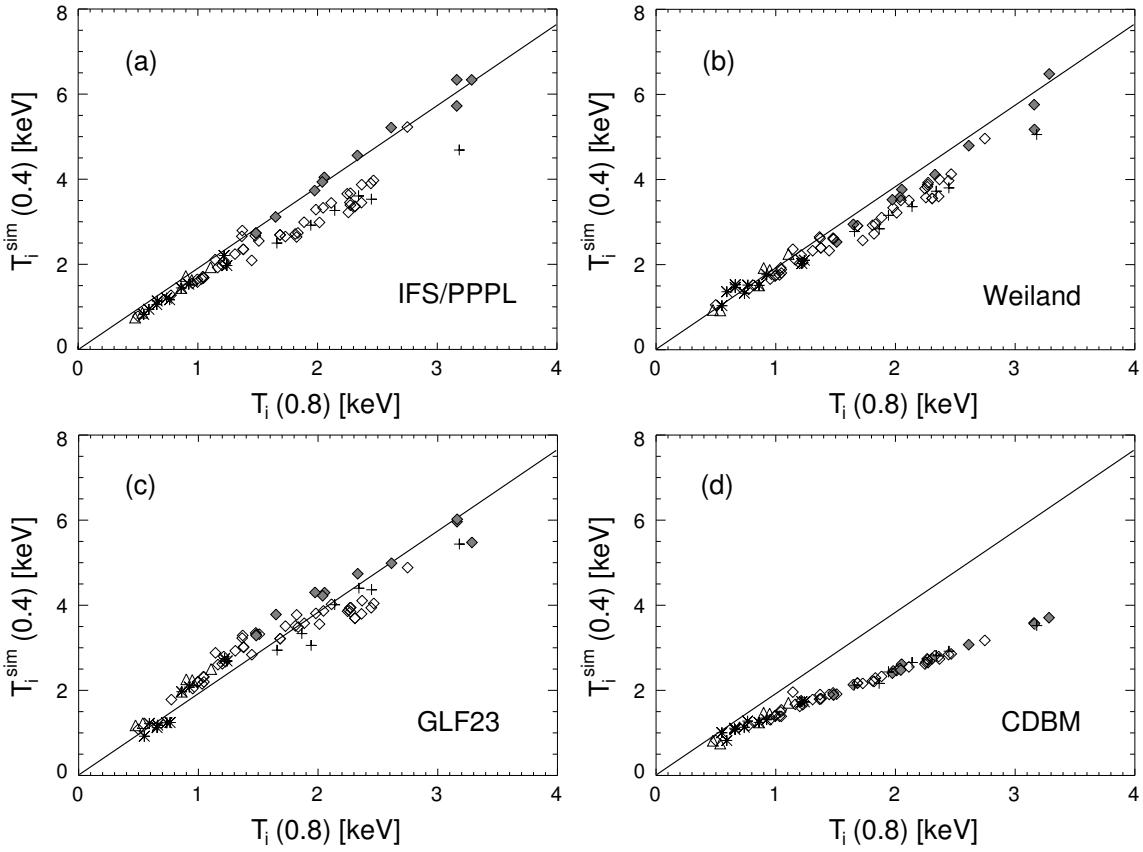

Figure 4.8: Simulated core to edge T_i according to the different models: a) IFS/PPPL b) Weiland c) GLF23 d) CDBM. The line reproduces the experimental points, being the same as in Fig. 4.1. Symbols refer to the scans as in Fig. 4.1.

dependence of L_{Tcr} on plasma parameters under the experimental conditions occur in the ITG models. Also the Weiland model, which exhibits a lower value of $\partial\chi_i/\partial(R/L_{T_i})$ at the turbulence onset, keeps the profiles stiff enough to reproduce the proportionality between core and pedestal T_i shown by the experiments. The ITG models present nevertheless deviations from a perfectly linear relation between core and edge T_i, due to changes in L_{Tcr} (magnetic shear, ratio T_i/T_e or effective ion charge) or to variable $\omega_{E\times B}$ stabilisation. All of them predict steeper T_i profile for the discharge #11197 with highly peaked density, but in the experiment this is not observed (see Fig. 4.1). On the other hand, ECH discharges are characterised by a lower ratio $T_i(0.4)/T_i(0.8)$, and this feature is returned correctly by all ITG models.
The CDBM model fails reproducing T_i profile stiffness. Only in the high density range,

corresponding to $T_i(0.8) < 0.8$ keV, the relation between core and pedestal T_i is predicted to be roughly linear (see Fig. 4.8). The experimental data related to the power and current scans reproduce this proportionality, although the ratio is lower than in the experiment. In the power scan, T_i and ∇T_i are raised simultaneously. In fact, ∇T_i increases with the heat flux and in the experiment it is not possible to decouple the heating power from an increase in pedestal T_i, unless density or current are changed too. Indeed, for the density scan the CDBM returns a clear flattening in the relation between core and edge T_i, in contradiction with the clear linearity observed in the experiment.
The behaviour of electron temperature in the present database is also well reproduced by the ITG/TEM based models as shown in Fig. 4.9. In this figure, the lines are guides for

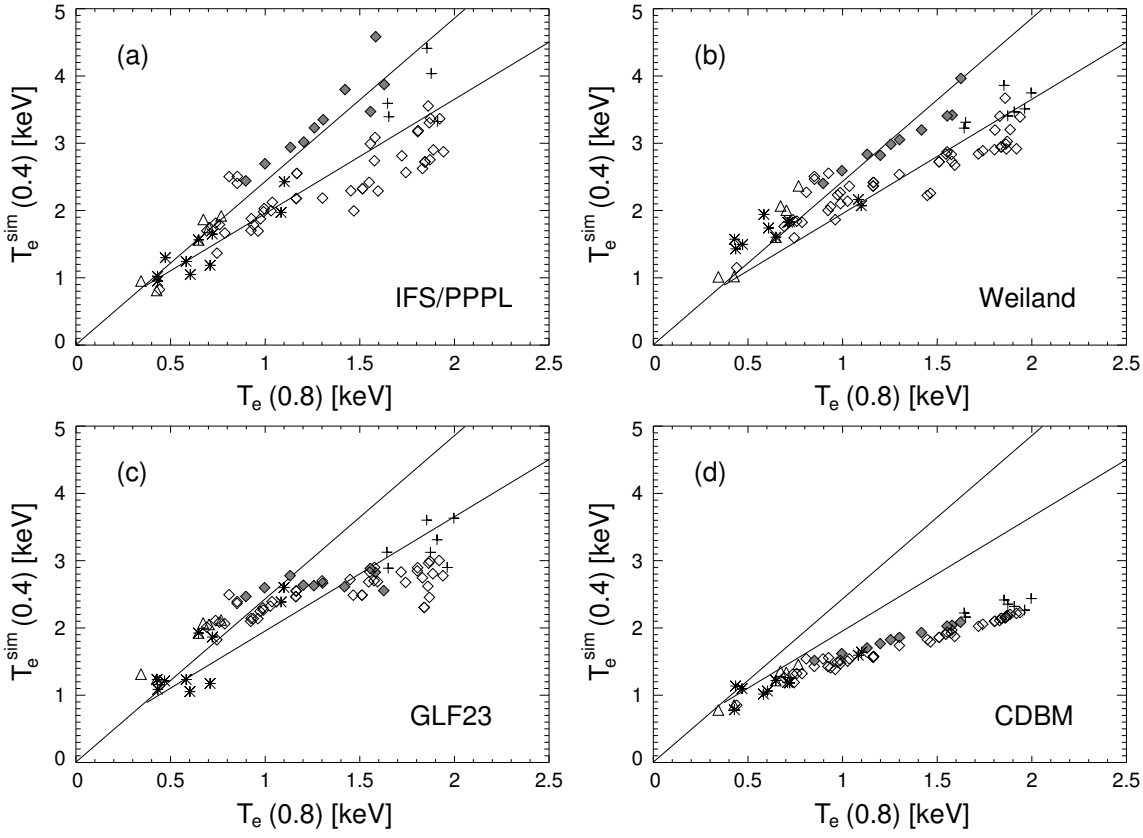

Figure 4.9: Simulated core to edge T_e according to the different models: a) IFS/PPPL b) Weiland c) GLF23 d) CDBM. The lines reproduce the experimental points, being the same as in Fig. 4.3. Symbols refer to the scans as in Fig. 4.1.

the eye and represent the fit of the experimental data in the low and high edge T_e ranges, they are the same as in Fig. 4.3. All models reproduce the bending towards flatter profile in the low collisionality corner of the database.

The change in the ratio of core to edge T_e has been explained introducing other transport mechanisms which would cause the observed "switch" in electron transport [37]; however, in the present database no additional transport feature is required to reproduce this behaviour.
For the CDBM model, however, the simulation results are far from the experimental data, and the change of the slope in Fig. 4.9 is related to the same flattening in the ion temperatures plot (Fig. 4.8), since ion and heat diffusivities are taken to be equal [21]. For the GLF23 model the bending is stronger than for the experiment, leading to overestimated core T_e for $T_e(0.8)$ below 1 keV and underpredicted T_e above this value. The discharge #11197 is not reproduced correctly: the high density gradient in this model generates a large heat flux, in contradiction to the enhanced stability observed in the experiment. It is important to remind that the density profile is not modelled self-consistently but taken from the measurement. A small experimental error can have a large influence on the modelled temperature in discharges where the density is peaked, as reported in [13] pag. 2493: "The model is, in fact, very sensitive to density gradients as the trapped electron modes onset with increasingly peaked density". This modelling set-up might be a disadvantage for the GLF23 model under certain experimental conditions, because solving particle transport self-consistently "leads to a density profile that is almost imperceptibly different from the given experimental profiles, yet the self-consistent density profile gives a much better fit to the temperature data than using the experimental density profile" ([13] pag. 2493). The Weiland model overpredicts core T_e in low current discharges. The decrease in the ratio $T_e(0.4)/T_e(0.8)$ is well reproduced because the inverse gradient length is clearly beyond the critical threshold, so that for high T_e the power is not enough to enhance further the temperature gradient and keep a constant $\nabla T_e/T_e$. The IFS/PPPL reproduces the T_e profile flattening at low densities because χ_e is assumed to be roughly proportional to χ_i [20]. If one considers that $\nabla T_i/T_i$ is fixed (which is the case in the simulations with the IFS/PPPL model), it follows that the ratio $\nabla T_e/T_e$ is proportional to $q_e/q_i\,(T_i/T_e)^{0.6}$. At high densities the ratio $q_e/q_i\,(T_i/T_e)^{0.6}$ remains almost constant, and the core electron temperatures is roughly proportional to the edge value. At lower densities, the ion and electron heat fluxes are less coupled and q_i/q_e is larger than 1 due to the lower electron NBI heating. $\nabla T_e/T_e$ is reduced, yielding a smaller ratio $T_e(0.4)/T_e(0.8)$ in the modelled profiles. This might, however, only partly explain the experimental observations. In the power scan the ratio q_i/q_e increases with heating power (see Fig. 4.2) but the ratio between experimental core and pedestal T_e does not flatten (see triangles in Fig. 4.3). A significant test of the hypothesis $\chi_e \propto \chi_i$ is provided by the ECH discharges, with hot electrons. The IFS/PPPL model predicts far too high core temperatures and turns out to be inadequate for modelling ECH experiments. Also for the discharge #11197 energy confinement is overpredicted. Actually, this discharge is characterised by low collisionality and peaked density gradient, at the limit of the validity

range for which the model was tested: the interpolation was performed for $0 < R/L_{n_e} < 6$. The case of low collisionality and strong density gradient is discussed in [20], warning that a further trapped electron instability occurs in the reference code, which is not included in the formulas for simplicity. So the IFS/PPPL model is expected to return higher stability than the source code under these experimental conditions.
Figures of merit have been introduced according to the definition by Connor and coworkers [19], in order to evaluate quantitatively the reproduction of the experimental data by the models. In particular the stored energy from the modelling is compared with the measured value. Here only the thermal energy is considered, i. e. the integral of the pressure profile, and the volume is taken between $\rho_{tor} = 0.2$ and $\rho_{tor} = 0.8$. The energy amount $p(0.8) \times volume$ is about one half of the total thermal energy and does not depend on the model since the boundary conditions for the temperature profiles are fixed at $\rho_{tor} = 0.8$. This energy fraction has been subtracted from both experimental and calculated energy, leading to the quantities W_j^{sim} and W_j^{exp} (j being the species label), which are plotted in Figures 4.10 and 4.11 . The Weiland model fails reproducing the current scan: the simulation yields too high electron confinement for low current discharges. The GLF23 model shows a trend to overestimate plasma energy at low edge temperatures and underestimate it towards collisionless plasmas; the deviations from the experimental value are small, but there is a clear trend against the pedestal temperature. Looking at the transport coefficient, a dramatic enhancement (even stronger in the electron channel) occurs in discharges with significant density peaking. There is a clear spatial correlation between the regions with high $\nabla n/n$ and flat T_e and T_i, in agreement with [13]. A few discharges at high collisionality behave differently from the overall trend, with the modelled energy below the experimental value: they are low current shots, possibly due to the sensitivity of the model to q and $\hat{s}$ profiles. The CDBM model systematically underpredicts the experimental energy of 20 to 40 %, with a trend to worsen towards high pedestal temperature.
The deviations are summarised in Table 4.3, defining

$$\sigma_j = \sqrt{\frac{1}{N}\sum_1^N \left(\frac{W_j^{sim}}{W_j^{exp}} - 1\right)^2}$$

where the sum is meant over the discharges in the database and N is the amount of shots analysed. Relying only on this figure of merit it is difficult to detect possible systematic trends or bad predictions in the central region: the volume there is small and contributes less to the stored energy. Moreover, even if the modelled temperature gradient were just flat from $\rho_{tor} = 0.5$ inwards, but the temperature profile were realistic outside this region, the lack would hardly be observed also because the contribution $n_j T_j(0.5) \times V(0.2 \leq \rho_{tor} \leq 0.5)$ dominates the central region. As suggested in [19], we extend the analysis reporting also the standard deviation of the temperature profile,

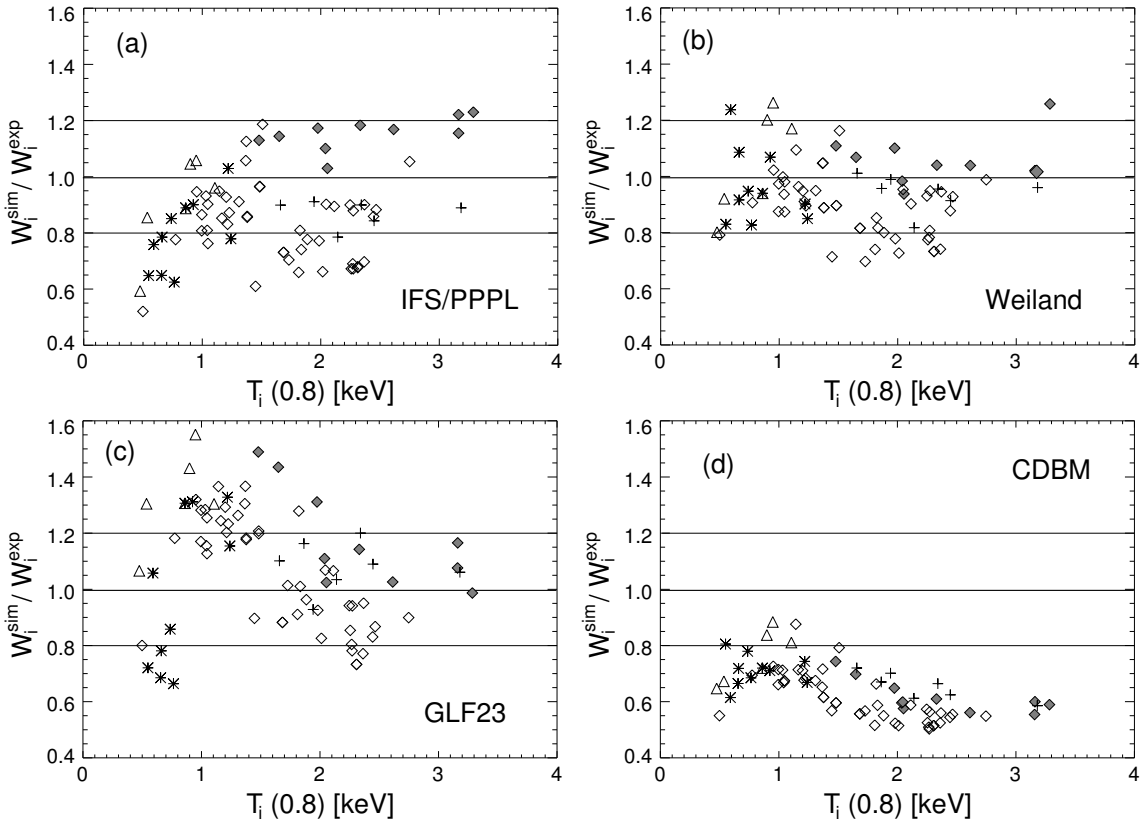

Figure 4.10: Simulated to experimental ion energy ratio vs. edge T_i according to the models: a) IFS/PPPL b) Weiland c) GLF23 d) CDBM. The pedestal pressure contribution is subtracted from both experimental and calculated energy. Symbols refer to the scans as in Fig. 4.1.

defined as

$$\mathrm{std}_j^{(c)} = \sqrt{\frac{\sum_1^n \left(T_j - T_j^{exp}\right)^2}{n \sum_1^n \left(T_j^{exp}\right)^2}}$$

where j is the species label and the sum is performed over n equidistant radial locations; the superscript (c) refers to the central region, from $\rho_{tor} = 0.2$ to $\rho_{tor} = 0.5$. Note that this is the standard deviation for a single discharge; in Table 4.3 this quantity is reported in capital letters to remark that it has been averaged over the database. To have a general insight whether data are systematically under- or overpredicted by a model, we report also the offset of the temperature profiles, again for the region between $\rho_{tor} = 0.2$ and

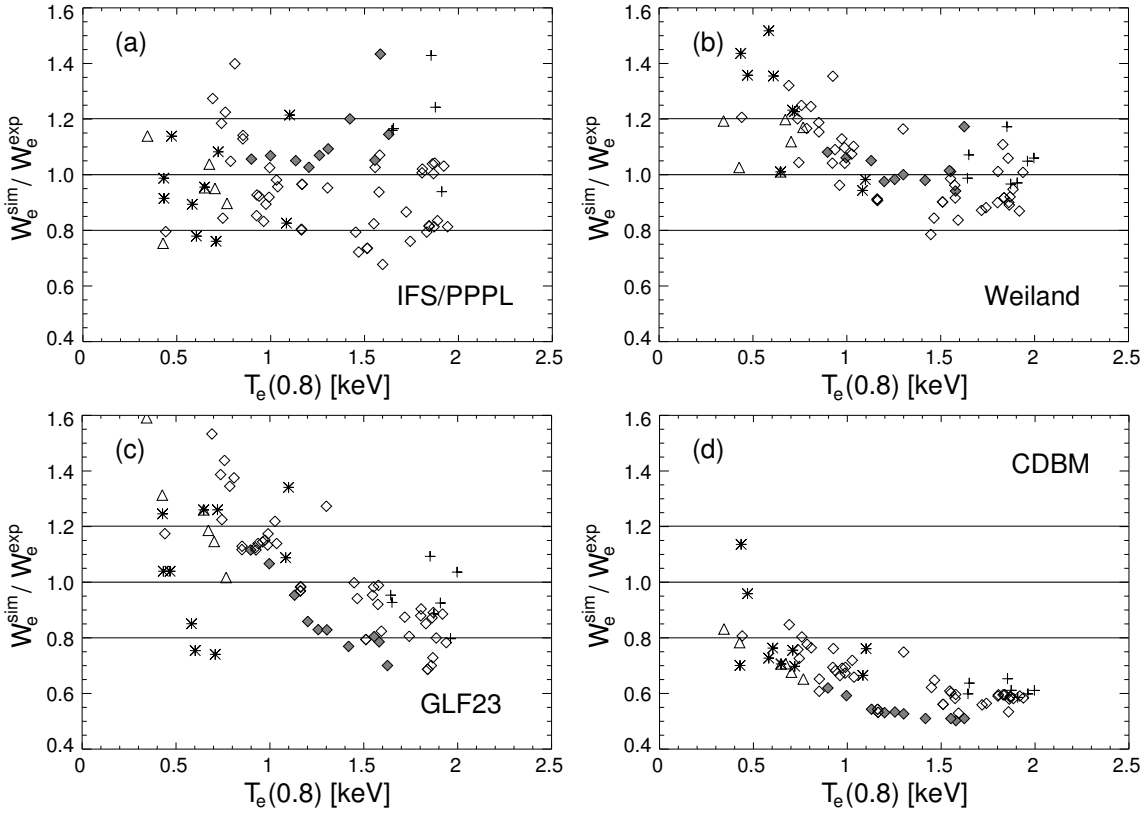

Figure 4.11: Simulated to experimental electron energy ratio vs. edge T_e according to the models: a) IFS/PPPL b) Weiland c) GLF23 d) CDBM. The pedestal pressure contribution is subtracted from both experimental and calculated energy. Symbols refer to the scans as in Fig. 4.1.

$\rho_{tor} = 0.5$:

$$\mathrm{off}_j^{(c)} = \frac{\sum_1^n \left(T_j - T_j^{exp}\right)}{\sqrt{n \sum_1^n \left(T_j^{exp}\right)^2}}$$

To average this quantity over the database is of course a loss of information, because positive and negative contribution might cancel. However, the amount of the deviation is already described by the quantity $\mathrm{STD}_i^{(c)}$.

The global energy content is well predicted by the ITG models, also subtracting the pedestal contribution; if one considers the full thermal energy both from experiment and modelling, the deviation drop by a factor of roughly 1.5. On the other hand, the prediction is improved by fixing the density to the experimental profile instead of modelling it self-consistently. The ITG-TEM based models are able to reproduce the experimental

	IFS/PPPL	Weiland	GLF23	CDBM
σ_{tot}	0.177	0.133	0.210	0.367
σ_i	0.211	0.148	0.244	0.372
σ_e	0.162	0.178	0.216	0.366
$\mathrm{STD}_i^{(c)}$	0.198	0.153	0.190	0.369
$\mathrm{STD}_e^{(c)}$	0.122	0.107	0.175	0.339
$\mathrm{OFF}_i^{(c)}$	-0.154	-0.113	0.013	-0.350
$\mathrm{OFF}_e^{(c)}$	-0.029	0.054	-0.016	-0.325

Table 4.3: Deviation of calculated from measured stored energy for NBI heated discharges, without pedestal contribution. Standard deviation and offset of T_e and T_i profiles. All quantities averaged over the database of NBI heated discharges.

energy within 20 %, the Weiland model yielding the best predictions. The CDBM model's deviations exceed 35 % and return systematically plasma energy below the experimental values.
The same analysis is applied to ECH+NBI heated discharges and the results are summarised in Table 4.4. The Weiland and GLF23 model perform even better than in the pure NBI case, with ion and electron energy predicted within 10 %.
The IFS/PPPL and CDBM models prove to be inadequate to describe NBI+ ECH experiments. For the CDBM model the reproduction of these data set is in line with the trend shown for NBI heated discharges. The IFS/PPPL model yields still very good predictions for ion transport but fails treating electron temperature, indicating that the assumption of $\chi_e \propto \chi_i$ holds only under particular conditions and is not a general property of tokamak core plasmas. When the ion heat flux is small, the ITG mode is not driven and χ_i is low. As a consequence, χ_e is small as well; in presence of electron heating, this leads to extremely overpredicted electron temperature gradients.

4.5 Summary

Summarising, the ion temperature profiles on ASDEX Upgrade in conventional scenarios are stiff over a large range of plasma density, current, NBI heating power and pedestal temperature. However, NBI+ECH discharges exhibit slightly lower values of $\nabla T_i/T_i$, indicating that either the stability threshold or the driven flux depends on the ratio T_e/T_i. Actually, also for the density scan the ratio T_e/T_i exhibit a significant variation, getting smaller towards lower densities till values around 0.5 . It seems that the stronger transport driven by high temperatures (due to the Gyro-Bohm pre-factor of the transport

	IFS/PPPL	Weiland	GLF23	CDBM
$\sigma_{tot}^{(r)}$	0.149	0.054	0.071	0.369
$\sigma_{i}^{(r)}$	0.136	0.081	0.116	0.349
$\sigma_{e}^{(r)}$	0.391	0.078	0.105	0.387
$\mathrm{STD}_{i}^{(c)}$	0.163	0.118	0.074	0.359
$\mathrm{STD}_{e}^{(c)}$	0.345	0.082	0.093	0.368
$\mathrm{OFF}_{i}^{(c)}$	-0.138	-0.090	0.014	-0.334
$\mathrm{OFF}_{e}^{(c)}$	0.284	0.063	-0.060	-0.350

Table 4.4: Deviation of calculated from measured stored energy for NBI+ECH heated discharges, without pedestal contribution. Standard deviation and offset of T_e and T_i profiles. All quantities averaged over the database of ECH+NBI discharges.

coefficients) is compensated by the (stabilising) deviation of T_e/T_i from unity. This is not the case for NBI+ECH discharges, where T_e/T_i is kept roughly equal to one. The electron temperature behaves similarly to the ion temperature for moderate density but not for lower densities, where the data of core T_e against pedestal T_e are more spread and tend to flatten. For low collisionality, a higher ratio $T_e(0.4)/T_e(0.8)$ cannot be obtained by additional power (as ECH), but can be obtained through the stabilising effect of peaked density profiles.

The ITG-TEM based models reproduce the experimental ion and electron temperature profiles well. Therefore, the prediction of the global confinement results to be very good, within 20 %, after subtracting the pedestal energy contribution. The Weiland model yields in average the best predictions, although electron temperature is poorly reproduced for low current discharges. The IFS/PPPL predicts too much stored energy for the case with very low collisionality and strongly peaked density gradient and wrong electron transport in NBI+ECH discharges. The GLF23 model underpredicts the temperature and energy data of low density shots, with a local strong enhancement in transport in the regions with significant density peaking. The error on the global confinement is moderate but there is a trend with decreasing density. The CDBM always predicts temperature and energy values far below the experimental ones, and fails qualitatively since it does not reproduce the linear relation between core and edge ion temperature.

In terms of the physics contained in the models, the ITG/TEM paradigm results to be satisfactory. The mode appears to be dominantly ion temperature gradient driven in pure NBI discharges (hence the good agreement of the IFS/PPPL model). However, for an accurate description of the electron channel under all circumstances a model has to retain both density and electron temperature gradient lengths when determining the onset of

anomalous electron transport. The coupling between ITG and TEM of the Weiland and GLF23 models yields good agreement with the experimental data.

Chapter 5

Heat transport in ECH dominated discharges

In theory, there is no difference between theory and practice.
But, in practice, there is. (R. M. Nixon)

In Chapter 4 heat transport has been investigated for H-mode discharges heated through NBI and a few cases featuring also ECH. It is appealing to switch to pure ECH discharges, to check the models' predictions for the case where electron heating becomes dominant. Actually, in this case the ITG does not play a major role and it is possible to test the models' behaviour for pure TEM. ECH power can be modulated in time giving rise to heat pulses. Observing their propagation in the plasma it is possible to investigate energy transport also transiently, providing a constraining test for the models and a measure of profile stiffness.
Evidence for a threshold behaviour of electron transport is observed on ASDEX Upgrade. Indeed, an ECH power scan experiment exhibits T_e profiles with almost constant $\nabla T_e/T_e$ in the confinement region [14]. However, a power scan could mimic this effect by enhancing simultaneously T_e and ∇T_e. Experiments on ASDEX Upgrade with ECH power modulation (MECH) confirm a non-linear relation between the electron heat flux and the temperature gradient: χ_e^{pert} is close to χ_e^{PB} inside the deposition layer, where the heat flux is small, and larger outside [49].
The modelling with empirical transport models based on a threshold in $\nabla T_e/T_e$ yields promising results; the best agreement is found assuming that the gradient lengths are not kept close to the critical threshold [16]. To improve the physical understanding of electron transport, a comparison with theory based models is required, in order to relate transport properties to the physics mechanisms. Modelling MECH discharges provides a very constraining test for the model itself, which has to reproduce simultaneously the

steady state profiles and the heat pulse propagation [50]. The Weiland and GLF23 models [12] [13] are applied here to very different plasma conditions compared to Chapter 4, namely with dominant electron heating provided by ECH. The IFS/PPPL model is not considered since the TEM is poorly treated. The CDBM model is not applied since it clearly fails to describe the NBI heated discharges.

5.1 The Electron Cyclotron Heating

5.1.1 Principle of the ECH

The ECH mechanism is based on the energy exchange at the resonance between the launched wave and the gyration motion of electrons around the magnetic field with the characteristic cyclotron frequency Ω_{ce}. The wave sources, called gyrotrons, operate at a given frequency. The resonance takes place at the layer where the magnetic field strength is such that the gyration frequency Ω_{ce} or a higher harmonic equals the wave frequency. Since the field strength is described in good approximation by the relation $B = B_o R_o / R$, it is constant on a cylindrical surface around the torus axis, which corresponds to a vertical line in the poloidal projection shown in Fig. 5.1. The figure illustrates the location of

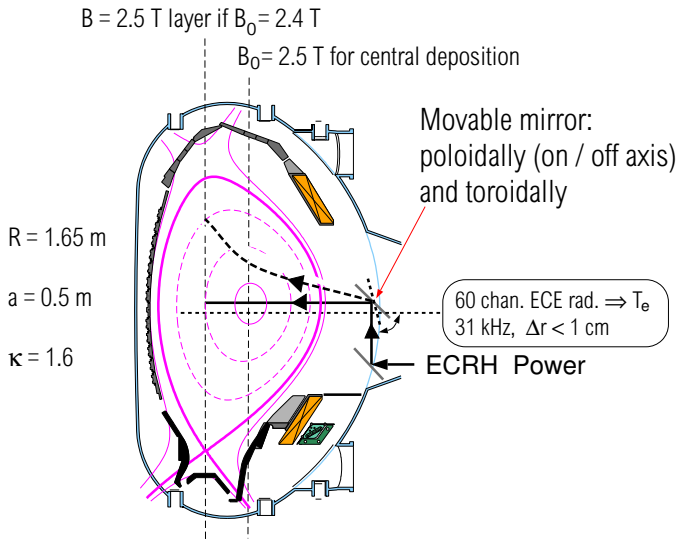

Figure 5.1: The ECH system on ASDEX Upgrade (poloidal section). The wave enters the plasma after reflection on a steady and a movable mirror. The poloidal angle together with the central magnetic field determine the deposition radius. Fast parallel energy transport heats rapidly the whole magnetic surface (dashed ellipsis).

the heat power deposition, at the section between the beam trajectory and the resonant layer. In tokamaks heat transport parallel to the magnetic field is very fast, so that the

whole magnetic surface (the dashed ellipsis in Fig. 5.1) is rapidly heated and we can define the deposition radius ρ_{dep} as the radial label of this surface, in normalised toroidal flux coordinate. Even if the focus happens to be set exactly at the resonant layer, the deposition width remains finite because the beam focusing is limited by diffractive effects [35]. Besides, relativistic electrons slightly broaden the absorption towards the high field side, since the gyration frequency decreases with increasing relativistic mass.

5.1.2 The ECH system on ASDEX Upgrade

On ASDEX Upgrade there are 4 gyrotrons operating at a frequency of 140 GHz, for a second harmonic X-mode absorption at the $B = 2.5$ T layer. The electrons absorb 100 % of the power in a single pass, which is important in order to avoid spurious energy sources at other plasma locations. Each gyrotron delivers up to 0.4 MW to the plasma, giving a maximum ECH power of 1.6 MW. The beams are focused by mirrors, yielding a narrow power deposition width, roughly 3 cm, corresponding to less than 10 % of ASDEX Upgrade's minor radius. If $B_o = 2.5$ T and the beam travels along the equatorial plane, then the plasma center is heated. Off-axis heating can be obtained either by changing the central magnetic field or by varying the poloidal angle of the movable mirror (see the dashed beam in Fig. 5.1). The localised power deposition is a major advantage of the EC heating concerning transport studies, because it allows an accurate reconstruction of the heat flux, which is almost step-like. Another powerful feature is the possibility to modulate the heat power sources with different frequencies, providing the ideal conditions for a transient state analysis, since the localised power deposition ensures a wide region of source-free plasma. In addition, high flexibility is provided by the ECH system available on ASDEX Upgrade: the 4 gyrotrons can be decoupled in order to deposit energy into different locations. In this way, the effects of enhanced heat flux and eventually enhanced temperature gradients can be investigated. It is also possible to apply power modulation to some of the gyrotrons and continuous power to the others, so that the effects of heating on transport can be detected also by means of the transient state analysis.

5.2 Diagnostic systems

The electron temperature profiles are measured by the ECE diagnostics, described in Section 4.1. The time resolution and the sampling rate are much higher than the modulation frequency, thus allowing to apply the Fourier analysis to the ECE time trace. In this way, the amplitude and phase profiles of the propagating heat wave can be measured.
The electron density is measured through the combination of interferometry and Lithium beam diagnostics, also presented in Section 4.1. The ECH deposition radii are measured in case of power modulation, otherwise they are calculated with the TORBEAM code

[35].

5.3 Simulation set-up

The version of the Weiland model used here is of June 1998 with 7 equations, including impurities (dilution approximation) and parallel ion motion. Again, collisions on trapped electrons are switched off by setting the collision frequency equal to zero. Also for the GLF23 model the same version is used as for the ion transport analysis (see Section 4.4.1). The boundary conditions for T_e and T_i are taken at the last closed flux surface. In this way, the heat wave propagation is affected only at the very edge. The value is adjusted by hand in order to match the outermost experimental channel of the ECE measurement. Since T_i profiles are not measured, $T_i(1)$ is set equal to $T_e(1)$. Plasma density is taken equal to the experimental profile, i. e. particle transport is not considered. The models are implemented as subroutines in the ASTRA code [38], returning the anomalous transport coefficients at every time step.

5.4 ECH power scan

A set of discharges has been selected with on-axis ECH and fairly low density, around 2 10^{19} m^{-3}. In Fig. 5.2 the comparison between experiment and models is shown for the discharges #13557 and #13558, with 0.8 and 1.6 MW EC power, respectively. The experimental as well as the modelled electron temperature profiles are averaged over several modulation periods. Although T_i profiles are not diagnosed for these discharges, the central T_i is measured to be about 1 keV. The measurement is taken with the Neutral Particle Analysers. Considering the experimental uncertainty and some degree of arbitrariness coming from the boundary condition $T_i(1) = T_e(1)$, both models are consistent with the measurement. As Fig. 5.2 shows, the heat goes almost entirely to the electrons. The anomalous electron transport returned by the models increases across the deposition layer (see Fig. 5.2 b)), since the electron temperature gradient is enhanced and drives the TEM turbulence unstable. Both models reproduce the experimental data with good accuracy.

5.5 Several harmonics transport analysis

The good results of the steady state modelling encourage a further, more stringent comparison between theory and experiment, involving also the transient behaviour. The comparison between experiment and model is shown for the discharge 13722, with a line

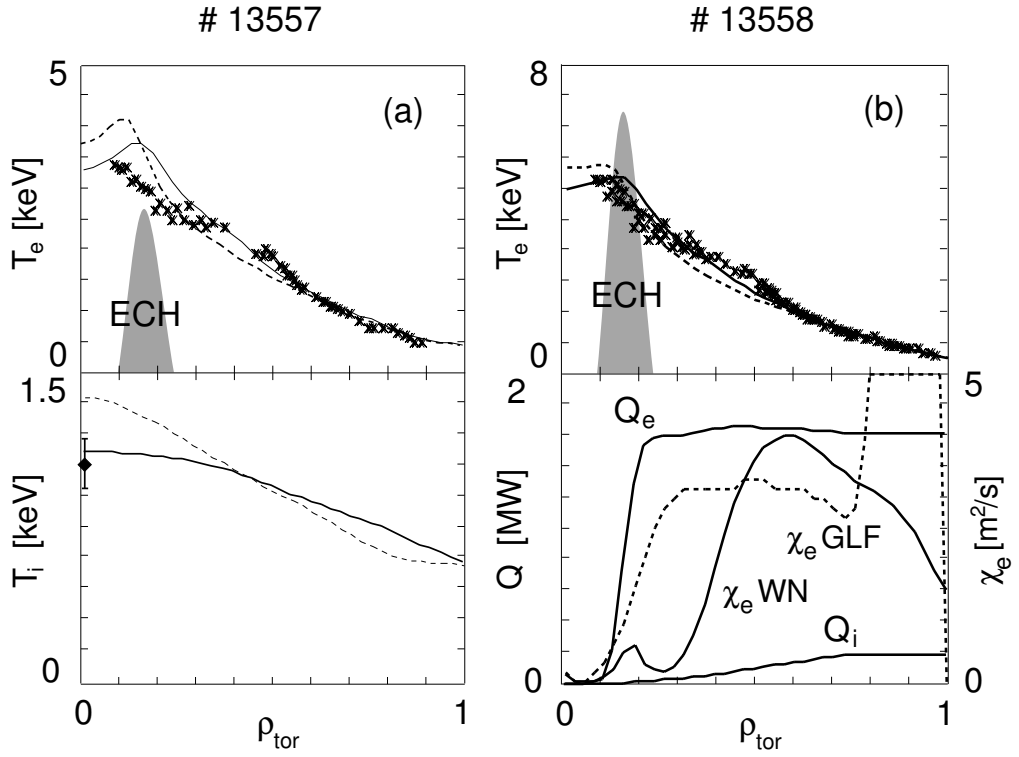

Figure 5.2: Steady state profiles: (a) T_e profile of the discharge #13557: experimental (crosses), from the Weiland model (solid line), from the GLF23 model (dashed line). The ECH power density profile is plotted too (a.u.). Below: T_i profiles according to the models, compared with the measured value of central $T_i = 1.05$ keV. (b) T_e profile of the discharge #13558 (symbols as in (a)). Below: integrated electron and ion power profiles and electron heat diffusivities from Weiland (WN) and GLF23 models.

averaged density around 4 10^{19} m^{-3} and an average ECH power of 1.5 MW deposited off-axis, at $\rho_{dep} = 0.32$. The plasma current is 0.6 MA. The reproduction of the steady state is shown in Fig. 5.3. The experimental T_e is well predicted by the Weiland model over the whole profile. The GLF23 model has an overall lower ∇T_e, possibly due to the low plasma current, as the model exhibits higher transport at low current (see Figures 4.10 and 4.11).

The gyrotrons are modulated with a period of 34 ms, duty cycle=0.85 and 100 % (on-off) power modulation. In this way, heat waves are induced and travel across the plasma. The pulse propagation is source-free over a wide radial extension, because the absorption layer is quite thin ($w/a < 0.1$) and the other heat sources are not periodic. Several harmonics of the temperature perturbation exhibit a good signal to noise ratio, allowing to study the heat wave propagation at different frequencies with identical plasma conditions (see Fig. 5.4). The amplitude and phase profiles of $\tilde{T}_e$ can be compared to the model

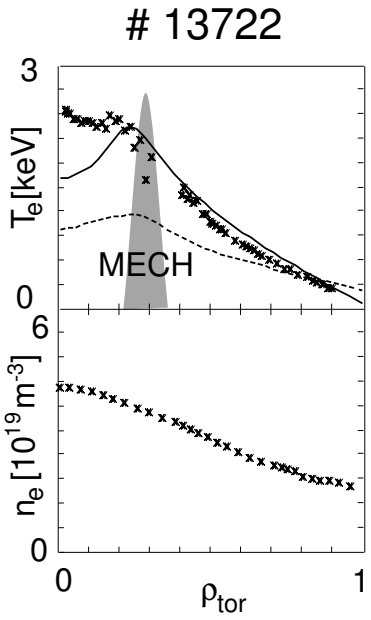

Figure 5.3: Steady state profiles of the discharge 13722: experimental T_e profile (points) compared to the predictions by the Weiland model (solid line) and the GLF23 model (dashed line). Below: experimental density profile.

predictions for frequencies of 29.4, 58.8, 88.2 and 107.6 Hz. As discussed in Section 1.4, flat amplitude and phase profiles are associated with high incremental transport and fast heat pulse propagation. The Weiland model matches the data well at all four harmonics, and for both amplitude and phase (see Fig. 5.4). In particular the profiles' asymmetry is well reproduced qualitatively, with steeper profiles (lower heat pulse diffusivity) inside the deposition than outside as in the experiment, as well as quantitatively, since the slopes coincide with the measured ones at all harmonics. Moreover, the correct absolute values of the amplitude and the phase at ρ_{dep} are obtained. For the phase, it means that the time delay of the T_e profile reaction to the heating is well predicted.
The GLF23 model predicts the heat pulse propagation with less accuracy but still the agreement is satisfactory.

5.6 Effects of ECH on transport

In the discharge 12935 the ECH power is modulated at $\rho_{MECH} \approx 0.75$, with a time-averaged power of roughly 0.2 MW and a plasma current of 0.8 MA. Two further gyrotrons are switched on later in the discharge, delivering 0.8 MW at half radius without power modulation. At this time most of the ECH power is applied at a different position with respect to the source of the heat wave [49]. In this way, the impact of heat flux

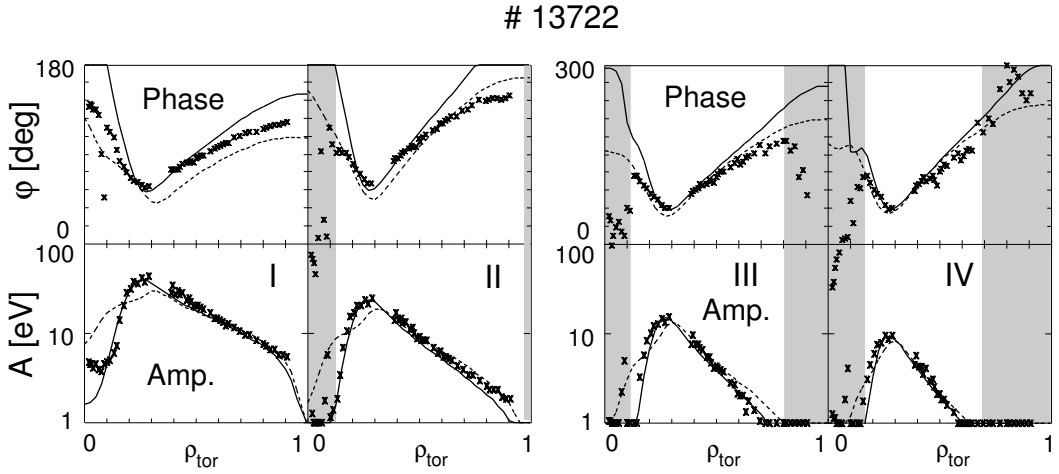

Figure 5.4: Amplitude and phase profiles of $\tilde{T}_e$ for the discharge 13722 at the frequencies ν=29.4, 58.8, 88.2 and 117.6 Hz: from experiment (points), Weiland model (solid lines) and GLF23 model (dashed lines). The shaded regions mark the region with low signal to noise ratio.

variations on transport can be observed decoupled from the analysis tool. In particular this experiment allows to test the models in two different ranges of heat flux. Inside the innermost deposition radius, the electron heat flux is nearly zero because the only source is ohmic and most of the heat is transferred to the ions, which are colder than the electrons. Crossing the ECH layer, the heat flux has a step and becomes large outside. Reminding Fig. 1.5, it is clear that for non linear $q_e - \nabla T_e$ scheme the incremental transport has strongly different behaviours for high and low heat fluxes, since the slope of the relation between q_e and $\nabla T_e/T_e$ changes radically.

The experimental steady state temperature profiles are reproduced well in the ohmic phase, as Fig. 5.5 (a) shows. In the ECH phase, outside ρ_{dep} the prediction is still satisfactory (Fig. 5.5 (c)), the Weiland model yielding the better agreement. However, inside the deposition radius the modelled T_e profiles are too flat. In this region anomalous transport is not driven by ∇T_e, so that small errors in the reconstructed heat flux profile introduce large uncertainties on the computed temperature gradients.

The experimental amplitude and phase profiles (see the points in Fig. 5.5 (d)) change their slope when crossing the ECH deposition radius. The profiles are observed to become flatter outside ρ_{dep}, where the heat flux is larger [49]. Since the ECH source at half radius is not modulated, the slope change between inside and outside ρ_{dep} is not an artifact of power modulation, but indicates indeed a change in the heat wave propagation. The Weiland model reproduces the amplitude and phase profiles very well both in the ohmic as well as in the ECH phase. The most important feature, i. e. the slope flattening outside ρ_{dep}, is reproduced with accuracy (see Fig. 5.5 (d)). Note in the ohmic case the

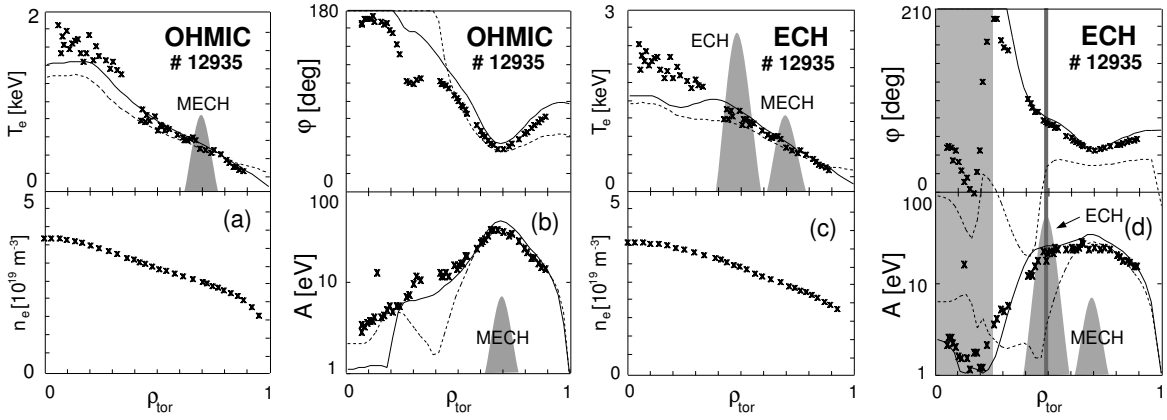

Figure 5.5: Discharge 12935: experimental (points), solid line (Weiland model) and dashed line (GLF23 model). Overplotted, the ECH and MECH power density profiles. Ohmic case: (a) Average T_e profile. Below: n_e profile. (b) Amplitude and phase profiles of $\tilde{T}_e$ at ν=29.4 Hz. After switching on ECH at half radius: (c) Average T_e profile. Below: n_e profile. (d) Amplitude and phase profiles. The vertical line marks the slope change. The shaded region has a low signal to noise ratio.

steepening of the experimental amplitude and phase profiles around $\rho_{tor} = 0.3$ observed in Fig. 5.5 (b). This is nicely reproduced by the Weiland model. Due to the sawteeth instability, the temperature profile is fairly flat inside $\rho_{tor} = 0.25$, so that the temperature gradient is kept below the TEM critical threshold. This is likely to be the explanation of the experimental observation: the heat pulse propagation is slow because the gradients are too low (due to sawtooth oscillations) to drive the turbulence unstable. Switching on ECH at half radius reduces the electron heat flux inside ρ_{dep} due to the exchange with the thermal ions; hence, the temperature profile in that region gets flatter too, with respect to the ohmic case. In this way, the TEM threshold is reached further outside, namely where the strong ECH is applied. Below the TEM onset, however, transport is not purely neoclassic, since there is some residual anomalous transport as we will discuss in detail in Section 5.8.

The GLF23 model predicts the heat wave propagation rather poorly already in the ohmic case: the amplitude falls too steeply towards the plasma center, the phase is too flat outside ρ_{MECH}. When ECH is applied at half radius, the modelling returns far too flat phase profile, with a wrong absolute phase value at ρ_{MECH}. The amplitude drops to very small values inside ρ_{dep}, making the analysis of the phase profiles unreliable in that region. However, a jump in the phase and a change in the logarithmic slope of the amplitude show that there is at least a small qualitative effect caused by the additional heating.

5.7 Experiments with constant ECH power

An ECH power scan might not be an adequate tool to estimate to which extent the T_e profile are stiff, because enhancing the global heating power determines also an increase of the pedestal T_e. Therefore, a uniform value for $\nabla T_e/T_e$ is returned also assuming weak profile stiffness or no threshold behaviour at all, at least in a limited range of temperatures. However, the localised ECH absorption and the possibility to decouple the deposition radii for the 4 gyrotrons ensure the highest flexibility to achieve large variations in the local heat flux with a constant ECH power. Taking advantage of this feature, a set of discharges is performed with the same temperature profile outside $\rho_{tor} = 0.7$ and different heat fluxes at half radius [52]. This is obtained heating the plasma at two different locations $\rho_1 \approx 0.35$ and $\rho_2 \approx 0.70$. In the discharge #14793 all gyrotrons heat at ρ_1, the #14794 has two sources in ρ_1 and two in ρ_2; finally, for the #14796 ECH is deposited only at the outer location ρ_2, thus yielding a very low heat flux between ρ_1 and ρ_2, which is the region of interest. In each discharge two sources (heating at the same radial location) are time modulated, adding useful information about perturbative transport and profile stiffness. The modulation period is 33 ms, with duty cycle equal to 0.5 and about 65 % of the full power during the off-phase, for an average heating rate $\approx$ 1.4 MW. Plasma density is very low and almost constant, around 2.2 10^{19} m^{-3}, the plasma current being 0.8 MA. As Fig. 5.6 shows, the edge T_e value keeps constant in

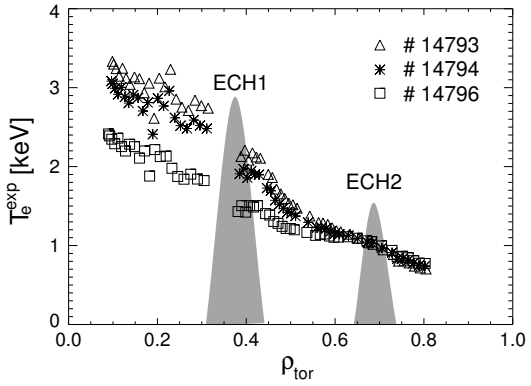

Figure 5.6: Experimental T_e profiles of the discharges #14793, #14794 and #14796. The heating is put: all into the inner location (#14793), half at ρ_1 and half in ρ_2 (#14794), all at ρ_2 (#14796). The total ECH power is kept constant.

the three discharges. This is because the global power input is the same. A check with the Thomson scattering diagnostic confirms that the T_e profile outside ρ_2 is the same for the three discharges [52]. If one assumes strict profile stiffness, given the same boundary condition the profiles should almost coincide over the whole radius, regardless of the shape of the heat deposition profile. On the other hand, in the picture of purely diffusive

transport with χ_e insensitive to the plasma parameters, gradients should steepen by the same factor as the heat flux. The measured temperature gradients are in between these two extreme cases. This confirms the existence of a non-linearity for anomalous transport but shows that profiles are only weakly stiff, in agreement with the the experimental observations and the modelling results already presented in the present Chapter and in Chapter 4. The TEM physics appears to reproduce the steady state temperature profiles,

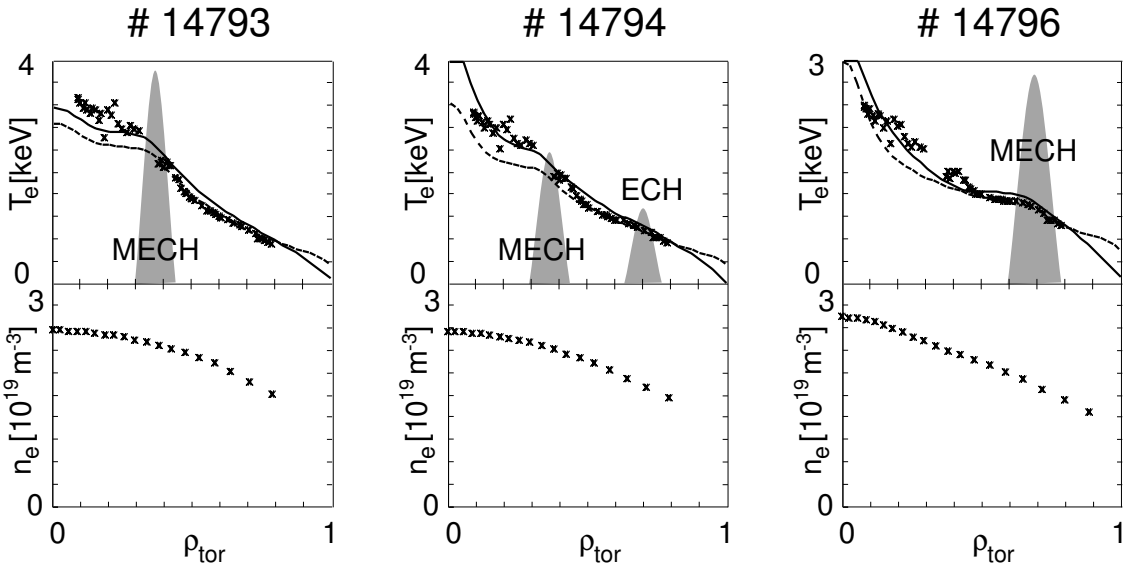

Figure 5.7: T_e profiles of the discharges #14793, #14794 and #14796 from experiment (points), Weiland model (solid lines) and GLF23 model (dashed lines). Overplotted, the ECH and MECH power density profiles. Below: n_e profiles.

as the Weiland and GLF23 models are able to reproduce all 3 cases with good agreement (see Fig. 5.7).

5.8 Discussion: results and profile stiffness

The good agreement between the Weiland model and the experiment allows to extract useful information about the properties required by a transport model to predict successfully the behaviour of ASDEX Upgrade ECH dominated discharges, and about the underlying physics. Considering the experimental results [14] [49], it is important to check how far the experimental and modelled inverse gradient lengths are above the critical threshold. The discharges #13558 and #12935 with strong ECH power and low density are selected for this study. In Fig. 5.8 the critical threshold profiles are shown for experimental background profiles. The stars give the critical value of R/L_{T_e} from the approximated formula 3.19. The experimental R/L_{T_e} profile (solid line) exceeds clearly the predicted stability

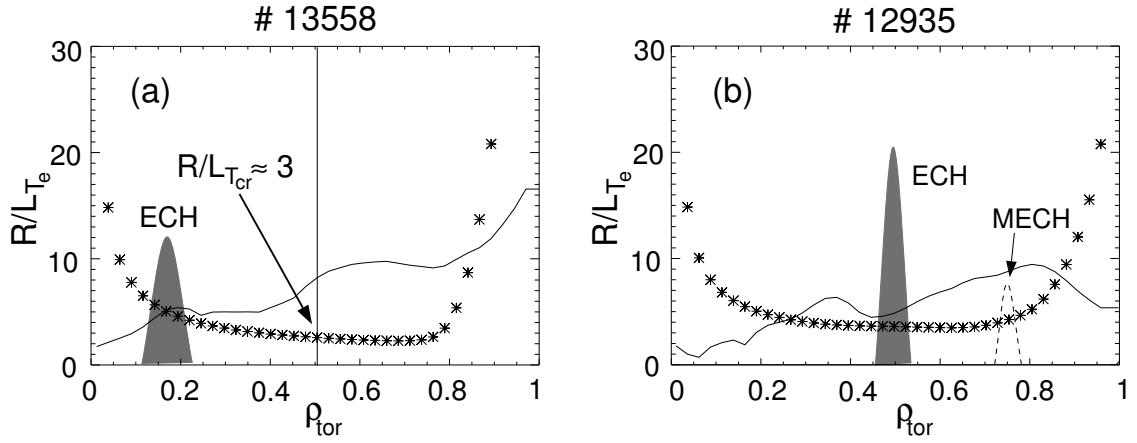

Figure 5.8: Normalised inverse gradient length: TEM critical threshold from the approximated formula with experimental background plasma parameters (stars); experimental profile (solid line). (a) Discharge #13558. (b) Discharge #12935 in the ECH phase.

threshold in the confinement region, by a factor 2 to 3. This means that profiles are not close to marginal stability, at least with strong central electron heating. Indeed, within the model the electron heat diffusivity does not increase very steeply beyond the critical gradient (Fig. 5.9). This fact, combined with the low value of the stability threshold, allows to reach gradients beyond the critical threshold through an increase of the heating power. The discharge #12935 shows an interesting behaviour: for R/L_{T_e} between 2 and 5 the TEM is not yet the mode with the highest growth rate (in fact it is an ITG mode) and the slope of the heat flux with respect to the inverse gradient length is flatter. This explains why the modelled heat wave propagation is slower inside the deposition radius (see the solid line in Fig. 5.5): the experimental R/L_{T_e} at ρ_{dep} is around 5 and increases outside the deposition layer. We remind that the steeper the heat flux, the faster the heat wave propagation, the flatter the amplitude and phase profiles. Considering the quantitative agreement with the experimental amplitude and phase profiles (Fig. 5.5), this observation might provide a physical explanation of the measured slope change. In the discharge #13558 the effect is not observed because of the flat density profile, which gives higher transport.

The GLF23 model does not reproduce simultaneously the steady state and the incremental transport. In most cases it reproduces the average temperature profiles correctly but underestimates the speed of the heat pulse propagation, predicting steep amplitude profiles. On the contrary, the discharge #13722, with low plasma current, is returned with satisfactory agreement concerning phase and amplitude, but the steady state temperature profile is predicted to be too flat. As a general trend, the ratio χ^{pert}/χ^{PB} is lower than in the experiment. This is confirmed if one looks at the behaviour of the heat flux with

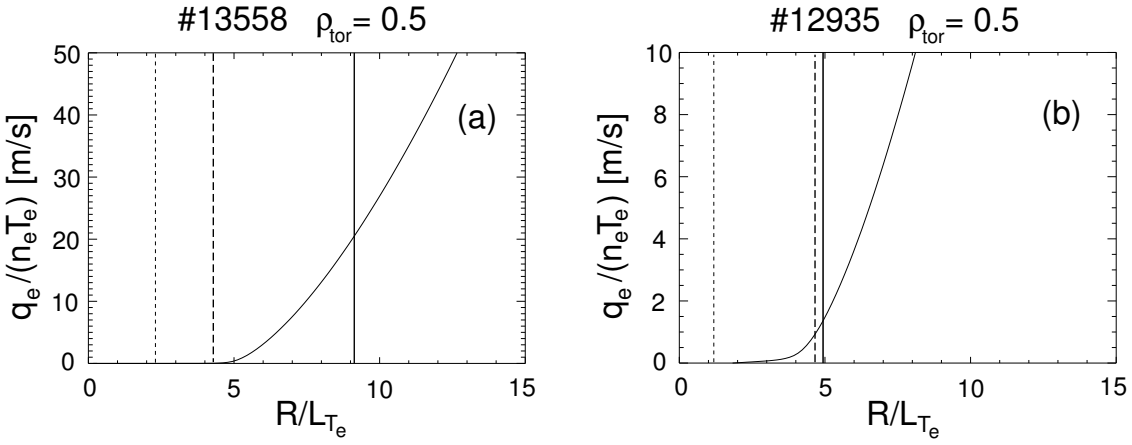

Figure 5.9: q_e dependence on R/L_{T_e} from the Weiland model, other parameters from the experiment at $\rho = 0.5$. The dashed thin line is the onset of the TEM, the thick dashed marks the ∇T_e value at which the mode becomes dominant, the solid line is the experimental R/L_{T_e}. (a) Discharge #13558. (b) Discharge #12935 in the ECH phase.

increasing temperature gradients (Fig. 5.10). The slope is moderately steep, comparable to the Weiland model, but there is not a significant offset of transport. As a consequence, χ^{pert} is close χ^{PB} so that in spite of high anomalous transport the phenomenology is different from that of profile stiffness.
The figure shows also that the stability threshold of the TEM and the anomalous transport depend significantly on L_{T_i}. Since the ion temperature profiles are not measured in these discharges, there is a certain degree of arbitrariness due to the choice of the L_{T_i} value.

5.9 Summary

The Weiland model succeeds in the simultaneous reproduction of the steady state as well as the transient transport in a variety of experimental conditions. For the steady state, the good prediction of χ_e^{PB} holds for different densities, deposition radii and ECH power. The transient behaviour is also well reproduced, since the slopes of the amplitude and phase profiles match the experimental results, showing that χ_e^{pert} is close to the measured one. Amplitude and phase are reproduced at all harmonics simultaneously, so the frequency dependence of the heat wave propagation follows the experimental one. The profiles asymmetry occurring in the experiment is observed also in the modelling, with quantitative agreement both inside and outside ρ_{dep}. The absolute values of amplitude and phase are obtained as well. The effects of heating on transient transport are reproduced, as the slopes flatten outside ρ_{dep} after switching on the further gyrotrons, decoupled from

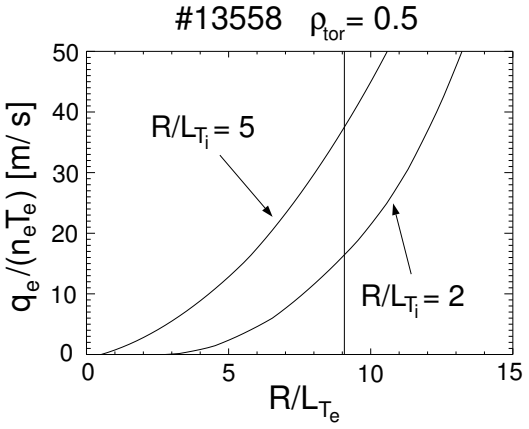

Figure 5.10: q_e dependence on R/L_{T_e} from the GLF23 model, other parameters from the experiment at $\rho = 0.5$, discharge #13558. Different values of R/L_{T_i} are chosen. The vertical line represents the experimental value of R/L_{T_e}.

the heat wave source.
Electron temperature profile are not strongly stiff: at a given pedestal temperature, an increase of the heat flux at mid-radius corresponds to a steeper temperature profile. A comparison with the stability threshold of the TEM in the Weiland model shows that the experimental gradient lengths are 2-3 times higher than the critical threshold if the heating is strong enough. This is because according to the Weiland model q_e increases with ∇T_e starting from $R/L_{T_{cr}}$, but not very steeply, if we compare it for instance with q_i driven by the ITG mode for ion heated discharges.
The TEM physics appears to be able to predict the features of electron heat transport observed on ASDEX Upgrade, including the transient behaviour. Therefore, the TEM is likely to be the mechanism governing electron transport in the case of strong electron heating.
The GLF23 model reproduces the time averaged temperature but underpredicts the speed of propagation of the heat pulse. In a discharge with low plasma current, the heat wave is well predicted but the average temperature is too flat. In all cases, the ratio of the transient to the steady state transport coefficient is close to 1 and hence lower than in the experiment. This is because the model features anomalous transport without a significant offset in terms of ∇T_e, so that the relation between the heat flux and the temperature gradient is roughly linear.

Chapter 6

Modelling of JET data

On ASDEX Upgrade the ion temperature profiles have been observed to be stiff. The ITG/TEM physics contained in the IFS/PPPL, Weiland-Nordman and GLF23 models is able to predict this behaviour and to yield a quantitative agreement with the experiment (see Chapter 4).
Electron temperature profiles exhibit profile consistency under some circumstances, but it seems that this is not a general property. Indeed, a threshold for the onset of anomalous transport is observed and MECH experiments confirm it (see Chapter 5). However, the inverse gradient length is well above the critical threshold and does not keep constant over a density scan. The TEM physics as contained in the Weiland reproduces this feature, and is in excellent agreement with ASDEX Upgrade data also quantitatively. The GLF23 model also reproduces electron transport, but features too small offset in the $q_e - \nabla T_e$ scheme, so that the agreement with the experiment does not hold for both steady state and transient analysis in ECH discharges.
An inter-machine comparison between different sized tokamaks is very helpful in order to validate the theory based transport models considered so far (see section 2.4), which are believed to be the candidates to predict the confinement performance of ITER. It is challenging to apply the models to JET discharges, because there are no free parameters to be adjusted and their physics is derived in terms of dimensionless parameters. JET is the largest tokamak built so far, with a major radius of 2.96 m and a minor radius of 1.25 m, yielding a somewhat lower aspect ratio compared to ASDEX Upgrade. The large minor radius makes JET optimal for core transport analysis and represents a step in tokamak size towards the larger dimensions of ITER. The flexible heating methods allow to study transport properties with locally variable heat flux, which is a key point to investigate eventual profile stiffness; in JET it is possible to have both the hot ion and the hot electron regime, allowing to explore the dependence of transport and stiffness on T_e/T_i.

6.1 Diagnostics employed

The modelling requires experimental measurements either as input for the simulations or as reference for the models' predictions. The same data are needed as discussed in section 4.1 in order to reconstruct the equilibrium and the heat fluxes for both ions and electrons. In addition, the power delivered to the plasma with a combination of Ion Cyclotron Resonant Heating (ICRH) and NBI cannot be computed with the existing ASTRA routines and has to be given as input profile. The reconstruction is done by means of the PION code [53] and relies on the experimental temperature and density profiles.
The electron temperature is measured with the ECE system, based on the Michelson interferometer.
The Charge eXchange Spectroscopy is employed for the ion temperature profile as well as for the ion toroidal velocity. The effective charge measurement is not available for the present discharges, so that for the simulations it is chosen to be 2.5, an arbitrary yet realistic value.
The density profile is obtained with the LIDAR diagnostics, which is based on the Thomson scattering.

6.2 Experimental results

In order to study profile stiffness, a database of discharges with constant edge heat flux is selected. In this way, the pedestal temperature is kept rather constant and profile stiffness can be checked by changing the heat deposition profile. The combination of NBI and ICRH heats on axis in some cases and around half radius in others, although the deposition is not well localised. The total input power is about 12 MW, the plasma current 2.8 MA and the toroidal magnetic field 2.75 T. The line averaged density ranges between 4.5 and 6 10^{19} m^{-3}.
NBI pre-heating ensures that strong ICRH creates a significant supra-thermal ions' population; the slowing down of these particles transfers energy mainly to the thermal electrons, whereas less energetic particles are slowed down by the thermal ions. So it is possible to raise the ratio T_e/T_i by applying NBI pre-heating and higher ICRH power. Actually, in the discharge 52097 the NBI power is reduced to 4 MW and ICRH is enhanced up to 9 MW, so that the total power is still the same as for the other selected discharges.
In addition, two "similarity shots" are analysed: these are discharges built to match most of the relevant dimensionless parameters of corresponding discharges performed on another tokamak, in this case ASDEX Upgrade. The parameters in our case are $\rho^\star = \rho_s/a$, $\nu^\star = \nu_{ie} qR/\epsilon^{1.5} v_{e,th}$ and β. It would be a stringent test for the models, which contain only dimensionless parameters, representing a direct check of the models' physics and of the choice of the experimental similarity parameters. Unfortunately the corresponding

discharges of ASDEX Upgrade were not yet available, so the modelling results of these JET discharges are not shown in the present thesis. The similarity shots have much lower plasma current (1 MA), toroidal field (1.1 T), density (about 2.4 10^{19} m^{-3}) and NBI heating power (3.5 MW). No ICRH is applied.

In Fig. 6.1 the measured core ion temperature is plotted against the pedestal tempera-

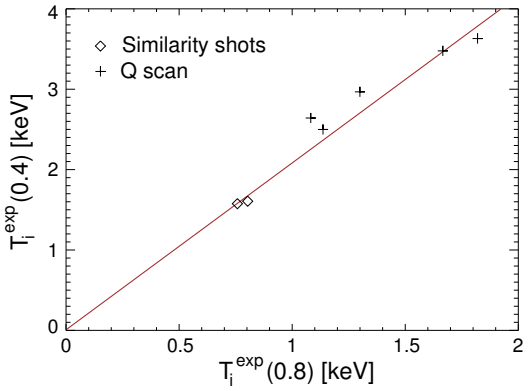

Figure 6.1: Experimental ion core temperature as a function of the edge temperature. The line is a guide for the eye.

ture. The experimental database is certainly too small to make any conclusive statement. However, the results resemble the clear linear relation observed for ASDEX Upgrade standard H-mode discharges (see Fig. 4.1). The range of edge temperatures is fairly wide and the ratio $T_i(0.4)/T_i(0.8)$ is close to the value ≈ 2 found on ASDEX Upgrade. The linear trend of Fig. 6.1 needs to be confirmed by increasing the database and broadening the temperature range.

The behaviour of electron temperature is also consistent with the observation of ASDEX

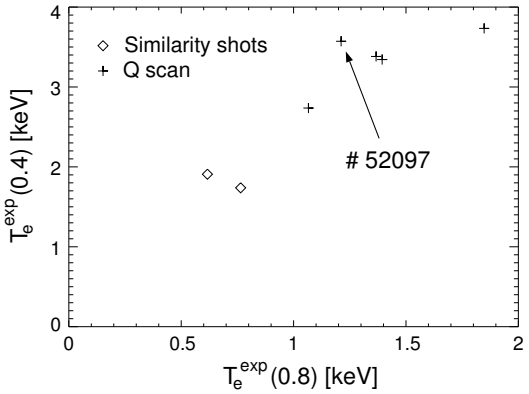

Figure 6.2: Experimental electron core temperature as a function of the edge temperature.

Upgrade (see Fig. 4.3), however the bending to a lower ratio of $T_e(0.4)/T_e(0.8)$ needs to

be established on the basis of several additional discharges.
We show in Fig. 6.3 the plasma density profiles as well as the power deposition profiles reconstructed with the PION code for three representative discharges: one with central heating, an off-axis heated case and a discharge with prevalent electron heating. The simulation results will be discussed in Section 6.3.2. The density profiles are quite simi-

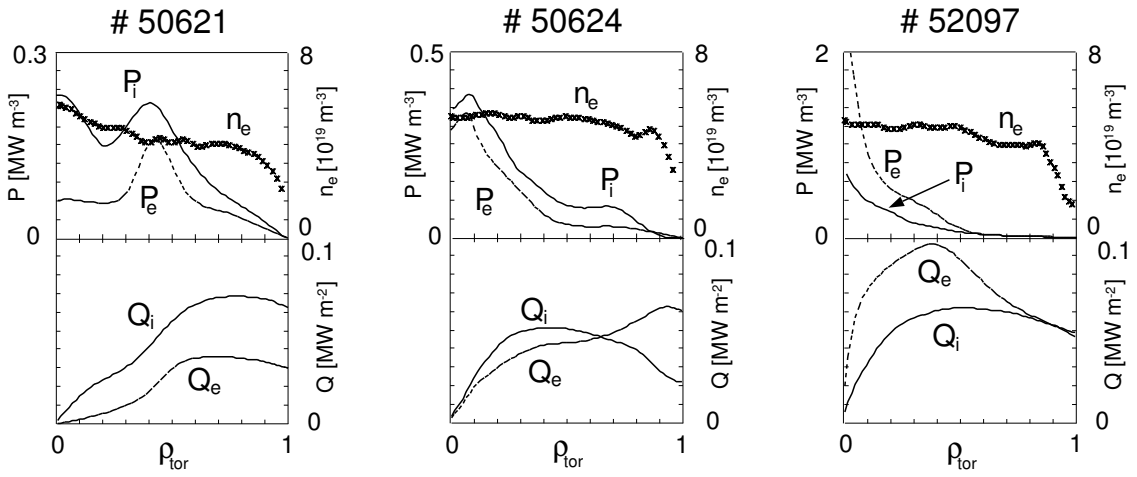

Figure 6.3: Experimental profiles of discharge 50621, 50624 and 52097. Above: power density profiles according to PION reconstruction. Electron density (points) is overplotted. Below: ion and electron heat flux profiles.

lar, whereas the ion and electron heat fluxes vary significantly within the database. The discharge 52097 in particular has strong electron heating in the whole confinement region, thus resembling the experimental situation of the ASDEX Upgrade power scan, analysed in Chapter 4. The case is different from ASDEX Upgrade discharges with both ECH and NBI heating, in that the boundary temperature is lower. Interestingly, the discharge 52097 exhibits the highest ratio $T_e(0.4)/T_e(0.8)$ for given boundary temperature, confirming the experimental trend observed in ASDEX Upgrade for the power scan. This also points in the direction of weak profile stiffness of the electrons, where additional electron heating leads to steeper temperature gradients. The large machine size limits the range of heat flux reachable with respect to smaller sized tokamaks such as ASDEX Upgrade. However, the observation in the discharge 52097 indicates that the "strength" of T_e profile stiffness can be investigated on JET as well.

6.3 Modelling results

6.3.1 Modelling setup

We model the data by means of the same models employed for ASDEX Upgrade. The implementation in the ASTRA code is the same, i. e. the same routines are used. Actually, for JET data we do not show the simulation results obtained with the CDBM model, because again the model has rather poor predictive capability. Instead, we report the modelling with the simplified version of the Weiland model derived in Chapter 3. It corresponds roughly to the version of the Weiland model with 4 equations, with neither impurities effects nor parallel ion motion. For this model, the routine has been programmed and implemented by the user and not by the authors, with the same stabilisation mechanism arising from $\omega_{E\times B}$ as for the Weiland model. The advantage is, that the formulas are explicite, so that all terms can be easily controlled and the physics effects can be recognised straightforwardly.
The boundary condition for the heat transport equations are again at $\rho_{tor} = 0.8$ for both T_i and T_e. The particle transport is not modelled; instead, the experimental density profiles are taken as input for the simulation. For neoclassic transport and current diffusion the same models are assumed as in 4.4.1.
The difference with respect to the modelling of ASDEX Upgrade discharges is that we cannot compute the combined heating delivered by ICRH and NBI with the existing ASTRA routines. Therefore, we take the output profiles of the PION code as experimental reconstruction of the power deposition, which is the common procedure adopted by the modellers of JET data. In this way, the deposition profiles keep constant in time, since they do not follow the evolution of the calculated temperature profiles.

6.3.2 Comparison with the experiment

With these assumptions and setup we apply the models to the three cases mentioned in Section 6.2. The discharge 50621 features off-axis heating, delivered mainly to the ion channel; the 50624 has more centrally peaked power deposition, the 52097 is characterised by dominant electron heating. The predictions of the models are illustrated in Figures 6.4, 6.5 and 6.6. The best agreement for ion transport is obtained with the GLF23 model, but actually all models predict the data with good accuracy. The Weiland and "reduced Weiland" models do not reproduce the profile steepening occurring around $\rho_{tor} = 0.4$. In the case with dominant electron heating the Weiland and GLF23 models yield the best predictions for T_i whereas the IFS/PPPL model underpredicts the central T_i.
As for electron temperature, the reduced Weiland model yields the best predictions. Also the GLF23 and Weiland models, both containing TEM physics, reproduce the experimen-

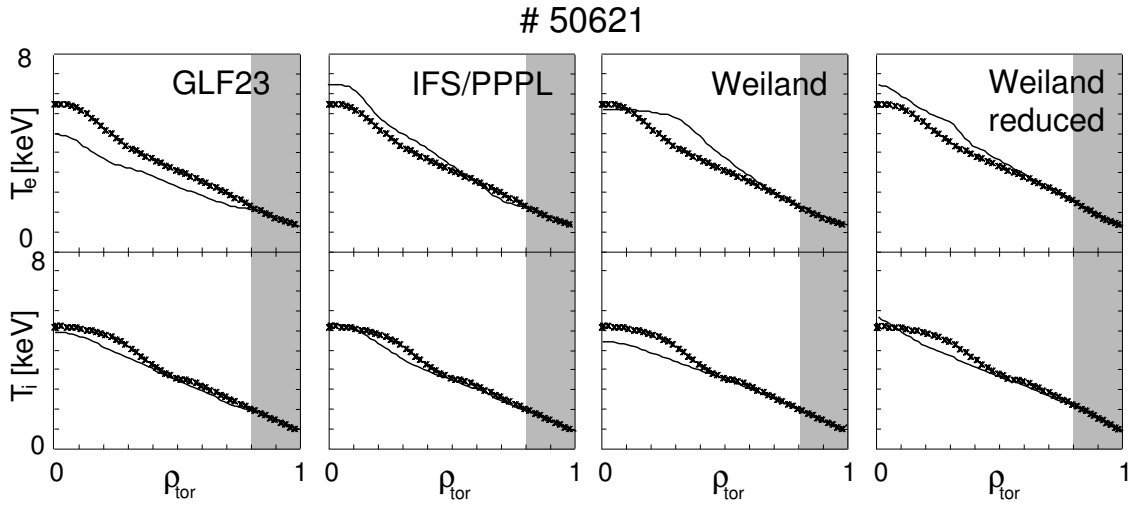

Figure 6.4: Discharge 50621: calculated (solid lines) and measured (points) temperature profiles. No modelling outside $\rho_{tor} = 0.8$.

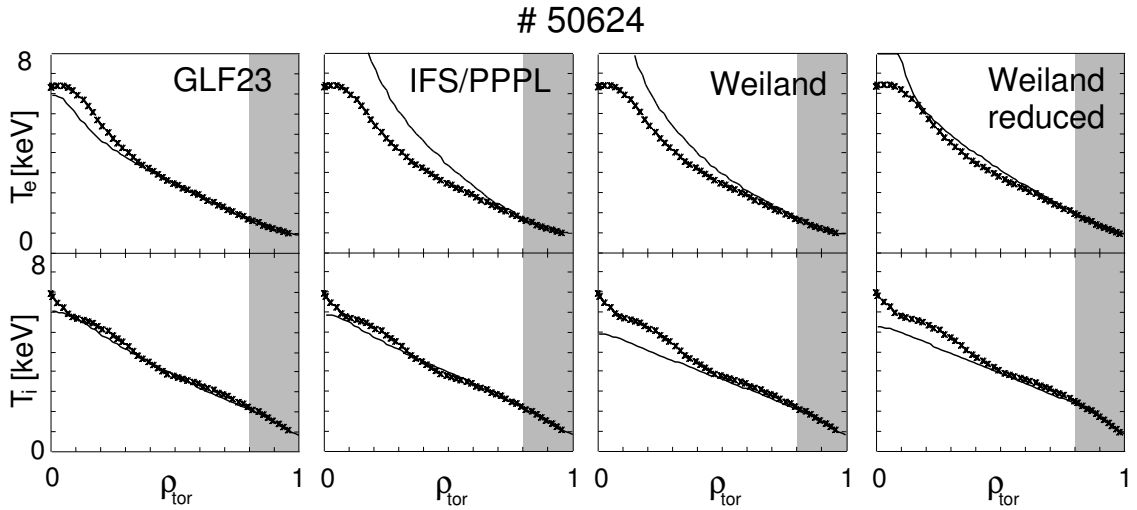

Figure 6.5: Discharge 50624: calculated (solid lines) and measured (points) temperature profiles. No modelling outside $\rho_{tor} = 0.8$.

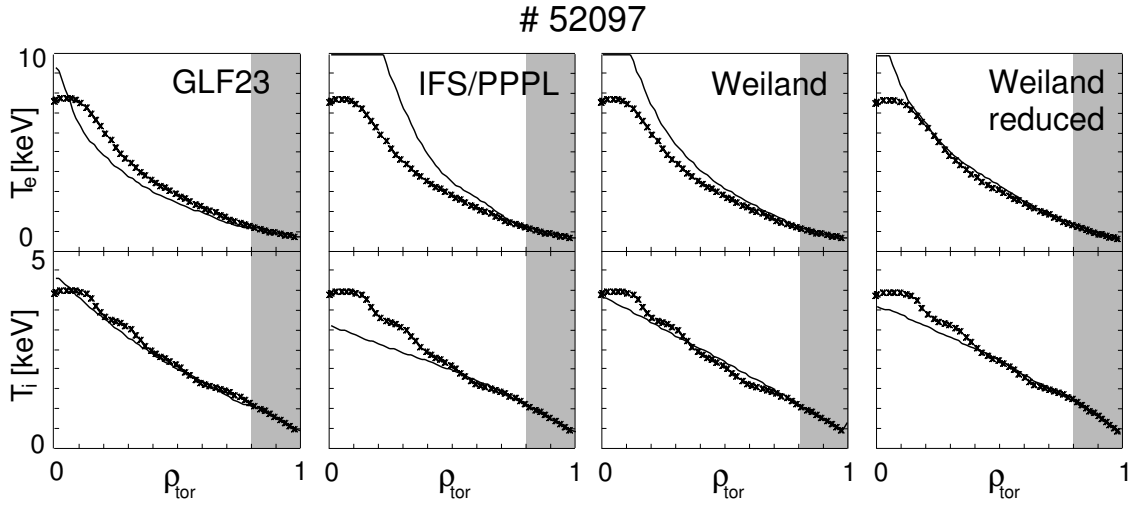

Figure 6.6: Discharge 52097: calculated (solid lines) and measured (points) temperature profiles. No modelling outside $\rho_{tor} = 0.8$.

tal profiles. We observe that GLF23 slightly underpredicts the temperature gradients, Weiland tends to keep above the measured T_e profile. It seems that the GLF23 model works better if the core electron heat flux is significant. Considering the possible errors of the power deposition profiles, both models have to be considered to predict the data correctly. The IFS/PPPL is able to predict the T_e profile when the electron heat flux is low (discharge 50621), but it clearly overpredicts the core temperature as soon as electrons are heated too. This indicates that the assumption $\chi_e \propto \chi_i$ does not hold in general, because for low ion heat fluxes (and therefore low χ_i, due to profile stiffness) electron transport is clearly underestimated by the IFS/PPPL model.

6.4 Summary

An initial database to study transport and profile stiffness issues on JET has been established. The heat deposition location is shifted keeping the edge heat flux constant. To extend the comparison with ASDEX Upgrade results, two similarity shots have been analysed although not yet modelled. The database needs to be increased and the corresponding ASDEX Upgrade discharges of the similarity shots have still to be investigated. Stronger variations of the most relevant plasma parameters are required before any conclusive statement is possible. However, preliminary observations confirm so far the behaviour of ion and electron transport as observed on ASDEX Upgrade:

- Core ion temperature is proportional to the pedestal value, with the ratio $T_i(0.4)/T_i(0.8)$ close to 2.

- For electron temperature this ratio is usually higher and tends to bend to lower values at higher temperatures. Again, stronger heating leads to steeper gradients by given edge T_e, indicating that stiffness should be weak. Experiments in transient state with T_e modulation are expected to provide additional information.

- Ion transport is in general well described by ITG physics: the IFS/PPPL, GLF23 and Weiland models reproduce the ion temperature profiles satisfactorily. An extension of the database with respect to boundary T_i values is highly desirable to check to which extent profiles are stiff.

- The combination of ITG and TEM physics as contained in the Weiland and GLF23 models reproduces JET data within the experimental uncertainties. Further ranges of density gradient, plasma current and average density could be explored to provide information on transport and on the stabilising effect of density peaking observed on ASDEX Upgrade. The assumption $\chi_e \propto \chi_i$ proves to be inadequate to model electron transport.

Chapter 7

Conclusions and outlook

It is easy to obtain confirmations,
or verifications, for nearly every theory -
if we look for confirmations (K. Popper)

7.1 Summary

The fusion power obtained in present tokamak devices and in ITER is strongly related to their energy confinement capability. Understanding and controlling heat losses is a major challenge for fusion research since decades. Inter-machine comparisons provide scaling laws for extrapolations to the larger dimensions of ITER, the first tokamak reactor, but a physical understanding is necessary to have more confidence in the extrapolation, to optimise the design of reactor scenarios and to reliably predict the transport phenomenology limiting the energy confinement. For this purpose, models relying on adjustments by means of *ad hoc* parameters cannot be applied, although they may prove to be useful to group the experimental data and give feedback to experiment and theory. Theory-based models are required which are intrinsically dimensionless and are constructed without any fitting to existing experimental data.
Although there is common agreement that anomalous transport is driven by plasma turbulence caused by micro-instabilities, predictions are far from being univoque, starting from the individuation of the mode which is believed to drive most of the heat losses. Even models based on the same instability mechanisms return quite different responses [31] [54] [51]. It is thus necessary to validate the transport models against the experiments as systematically as possible.

7.2 This thesis' contribution

In this thesis such a systematic comparison is presented. The work has improved our understanding in different areas.

Theory

Although no new theory models are developed within the framework of this thesis, the application of the models has increased our understanding of their main properties. This is no trivial outcome: the models are very complex in their behaviours and depend on many different parameters. It has been possible to identify the key dependences and to understand failures in certain parameter regions due to the lack of essential physics.

Experiment

The modelling provides a "new language" to discuss the experimental results. It allows to order the data and to understand seemingly contradictory experimental evidences. This point should not be underestimated. For decades the description of transport was based on empirical descriptions. Although this kind of modelling helped to identify different phenomenology, this approach is limited by the fact that a completely different empirical *Ansatz* can describe the experiments equally well. Besides, most of the empirical models proved to be very successful on a given tokamak for certain kind of discharges, but had to be adapted or adjusted for other machines or experimental regimes, without any possibility to determine *a priori* a validity range. This allows no confidence in the prediction of a new experiment. Therefore, reliable results can in the end only be obtained through a description that finds its roots in the theory.

Comparison theory versus experiment

Finally, one gets an overview how well the current models describe the experiment. Through the comparison of the models one has some insight which physics is essential to keep, what requires more accurate description and to which feature the experiment is sensitive. In this way, feedback is provided for the theory to improve the physics description where it is necessary; new experimental activity is stimulated to test the theory in the crucial parameter ranges. We discuss in the following the achievements of the present thesis work in detail.

7.2.1 Database

A dedicated extensive database of 91 ASDEX Upgrade discharges has been constructed and translated into ASTRA format; this allows to challenge, distinguish and possibly

falsify the available and future transport models.

- There are single parameter scans over ranges as wide as possible, to test the models dependences and not only the good agreement of the transport coefficients.
- Some discharges feature dominant ion heating, others electron heating.
- In most electron heated discharges, steady state transport analysis as well as the analysis of the transient state is performed.
- The effects of localised electron heating is studied.
- Discharge with constant pedestal T_e and total ECH power provide a direct measure of T_e profile stiffness.
- An initial database of 7 JET discharges is built, including 2 similarity shots linked to ASDEX Upgrade discharges. The inter-machine comparison challenges the models to predict the performances of different sized divertor tokamaks in discharges with identical dimensionless parameters. No free parameters are included in the theoretical models. However, the database needs to be increased and the similarity shots have to be compared.

7.2.2 Development of analysis tools

- The theory based models have been provided by the authors as routines. Interfaces between the routines and the ASTRA code have been adjusted and tested, enabling them to run on the available platforms.
- Routines for the quantitative evaluation of the profiles' prediction have been written according to the criteria by Connor and coworkers [19]. The profile analysis reduces on average the large uncertainties typical for the local analysis, in particularly those arising from the large errors in ∇n_e and from profile stiffness. Fortran programs have been written to handle the statistics.
- Tools for the heat pulse analysis in ASTRA have been implemented.
- Stand-alone versions of the models have been built, allowing to study the parametric dependences of the models and eventually find out an *experimentum crucis* where the predictions deviate. A systematic validation of the models with theoretical transport codes is still to be done.
- A reduced version of the Weiland model, corresponding to the 4 equations version, has been re-derived and implemented.

7.2.3 Overview of modelling results

IFS/PPPL

The IFS/PPPL model proves to predict the ion transport with good accuracy. Profile stiffness is predicted and the energy content is in quantitative agreement with the experimental value. Electron transport is well predicted only in presence of dominant ion heating.
The model fails describing electron transport as soon as the ion heat flux gets smaller and the electron heat flux increases. Due to profile stiffness, low ion heat flux means low χ_i. Since the model assumes $\chi_e \propto \chi_i$, electron transport is reduced too and almost no anomalous transport occurs, unlike in the experiment.
The ITG physics is likely to be the main mechanism governing core ion transport. The general assumption $\chi_e \propto \chi_i$ is contradicted by the experimental observations. The onset for anomalous electron transport in electron heated discharges appears to have a threshold in $\nabla T_e/T_e$ rather than in $\nabla T_i/T_i$.

GLF23

The GLF23 model succeeds when predicting ion transport and T_i profile stiffness. Electron steady state transport is also well predicted for most ASDEX Upgrade discharges, both NBI and ECH heated. For JET discharges the model gives the best predictions.
The dependence on ∇n_e is in disagreement with the experiment: strong density peaking destabilises the trapped electron mode, enhancing transport dramatically. For ASDEX Upgrade ECH discharges, the ratio $\chi_e^{pert}/\chi_e^{PB}$ is below the measured value. The steady and the transient state are never simultaneously well predicted: if the averaged T_e profile is accurate, the heat pulse is slower than in the experiment; if the heat wave is well described, the steady state T_e profile is too flat.
The physics of ITG and TE modes appears to be suited to describe heat transport in the tokamaks ASDEX Upgrade and, according to a preliminary analysis, on JET as well. The model's sensitivity to ∇n_e is in contradiction with the experimental result, where density peaking has not such a dramatic impact on transport and in any case it acts stabilising. This part of the model should be improved, although for ITER the density profile is expected to be quite flat. The ratio $\chi_e^{pert}/\chi_e^{PB}$ indicates that in reality there is some more significant offset for anomalous electron heat transport than in the GLF23 model. This is another evidence that the residual transport driven by density gradients appears to be much larger than in the experiment. This problem is known to the authors and has been explained as the occurrence of an instability, but the reason of the strong anomalous transport driven by this mode is not yet clarified.

Weiland

For H-mode discharges the Weiland model yields quantitative agreement with the experiment. The power and the density scans are reproduced correctly. The model also predicts electron transport with high accuracy, both the time averaged temperature profiles as well as the amplitude and phase of the propagating heat wave. Several harmonics of the fundamental wave frequency are well described and the effect of additional heating is predicted correctly.
However, discharges with low current (400 kA) are predicted to have much higher confinement than the experiments. This indicates that the dependence on q and $\hat{s}$ is not accurate. Indeed, the implementation of the q and $\hat{s}$ dependences in the Weiland model appears to be too simplified. Negative shear is not treated. Therefore, this version of the model should not be applied to scenarios with flat q or negative shear.
This simple model confirms that the combination of ITG and TE modes is likely to govern heat transport on ASDEX Upgrade and possibly on JET. The successful reproduction of ion heated discharges in spite of moderate stiffness clarifies that ASDEX Upgrade experimental results are compatible with a wide range of T_i profile stiffness: from IFS/PPPL (strong) to Weiland (medium), the increase of χ_i beyond R/L_{T_i} is different by an order of magnitude. The q_e versus ∇T_e offset scheme of the model, fitting different constraining experimental situations, provides a realistic estimate for the TEM stability threshold and for profile stiffness. Electron temperature profiles are weakly stiff and the experimental gradients exceed the critical threshold by factors up to 3 in presence of strong central EC heating.

CDBM

The qualitative disagreement with the experiment shows that this model does not contain the physics necessary to describe ion heat transport. In particular, ion profile stiffness is not predicted. The lower transport level observed in stand-alone runs with the background parameters from an electron heated discharge suggests the CDBM model as a possible alternative description of ECH discharges. A systematic comparison between experiment and theory, involving also the heat pulse analysis, is still to be done. However, the difference observed in the experiment between ion and electron heat transport proves that the assumption $\chi_e = \chi_i$ is inadequate.

7.3 A glance beyond

One can do the exercise to check the models' predictions about ITER's energy confinement and gained fusion power [54]. "Stiffer" models get more optimistic with higher pedestal temperatures, but have stronger power degradation (the effort of additional heating is

almost useless). Our study has provided detailed evidence for a threshold behaviour of heat transport, finding weak stiffness for T_e profiles and moderate to strong stiffness for T_i profiles. This result remarks that the confinement performance of ITER depends strongly on the pedestal values of T_i and T_e, with some more freedom for electron heating. As reported in [54], it is premature to make realistic statements for ITER so far, as there is still large uncertainty about the pedestal values of T_i and T_e. The understanding of edge transport is therefore of primary interest.

The influence of Z_{eff} is treated in the models but has not been investigated experimentally so far. Dedicated discharges scheduled for the next ASDEX Upgrade campaign will provide the data to be compared with the theoretical predictions. The inter-machine comparison should be extended. The JET database is too small to draw conclusions. It is necessary to include more discharges and to extend the intervals of the scan parameters like T_e/T_i, I_{pl}, total power and plasma density. An optimal test for the dimensionless character of the models is the simulation of the similarity shots, discharges from different tokamaks where the relevant dimensionless parameter are chosen to be equal. This comparison as well as a general extension of the database are in progress.

A theory model is not successful if it just provides a good guess of the transport level in certain situations: it is expected to approximately reproduce the physics of the experiment. For instance, the IFS/PPPL model matches electron transport for NBI heated discharges, but the anomalous transport is driven by ∇T_i and not by ∇T_e, leading to wrong predictions for ECH discharges (actually the model is not developed for these experiments). For this reason we have checked the models' dependences and performed single parameter scans. However, a complementary approach consists in validating the models against more complete theoretical codes. Such codes do exist in the form of full kinetic calculations or real turbulence descriptions. The more complete models are computer-time demanding and cannot be used for a study as extensive as presented in this thesis. However, they can and should be used to benchmark the simplified models, assessing the limitations of the latter. Such a validation is highly desirable for the ITG/TEM models.

It is commonly believed that $\omega_{E\times B}$ has a beneficial effect in that it stabilises the ITG modes. Since v_{tor} is a major contribution to $\omega_{E\times B}$, the question arises how the angular velocity does propagate radially across the plasma. The development of momentum transport models and the modelling of experimental profiles are expected to bring clarity in the near future.

The IFS/PPPL and Weiland models are not constructed for low and negative magnetic shear plasmas. In general, the models relying on the ballooning approximation (as GLF23, Weiland and IFS/PPPL) are not suited to describe a region with zero or nearly zero magnetic shear [55]. This is the case for discharges with Internal Transport Barriers (ITBs). The development of models based on other approaches can provide a useful benchmark and also complementary information. In particular the Wentzel - Kramers - Brillouin

(WKB) method [55] has been developed for ITG modes and could lead soon to an extensive 1D-modelling of ITBs and reverse shear discharges.
It seems feasible to perform soon experiments with ion heat pulses by heating tangentially with modulated NBI (low power). This powerful analysis tool would provide a further test for the models and a direct measure of T_i profile stiffness, which has been observed but not definitively evaluated. Both the Weiland and the IFS/PPPL models show good agreement with the data although they differ by an order of magnitude in the quantity $\partial\chi_i/\partial\left(R/L_{T_i}\right)$.
An extension of our approach is to model also the density profile self-consistently. This would reduce the large errors on the heat fluxes due to the experimental uncertainties of ∇n_e, particularly for the GLF23 model. Studying the behaviour of the density profiles is a topic of major interest, because particle transport is crucial for energy confinement and for the ignition condition. These studies have already started showing promising results [56] [57].

Bibliography

[1] J. Wesson, *Tokamaks*, Clarendon Press, Oxford, 1987

[2] F. L. Hinton and R. D. Hazeltine, Rev. Mod. Phys. **48** (1976) 239

[3] ITER Physics Basis, Nuclear Fusion **39** (1999) 2175

[4] Y. Koide *et al.*, Physical Review Letter **72** (1994) 3662

[5] A. G. Peeters *et al.*, 18th IAEA Fusion Energy Conference (Sorrento, 2000), IAEA-CN-77-EXP5/06

[6] T. S. Hahm, K. H. Burrell, Physics of Plasmas **2** (1995) 1648

[7] N. J. Lopes Cardozo *et al.*, Plasma Physics and Controlled Fusion 37 (1995) 799

[8] A. Jacchia *et al.*, Physics of Fluids B3 (1991) 3033

[9] S. I. Braginskii, Transport Process in a Plasma, Review of Plasma Physics, M. A. Leontovich (ed.), Consultants Bureau, Vol. 1, pp. 205-311 (1965)

[10] F. Jenko *et al.*, Physics of Plasmas **8** (2001) 4096

[11] W. Dorland *et al.*, Physical Review Letters **85** (2000) 5579

[12] J. Weiland *et al.*, Nuclear Fusion **29** (1989) 1810

[13] R. E. Waltz *et al.*, Physics of Plasmas **4** (1997) 2482

[14] F. Ryter *et al.*, Nuclear Fusion **41** (2001) 537

[15] G. T. Hoang *et al.*, Nuclear Fusion **38** (1998) 117

[16] F. Imbeaux *et al.*, Plasma Physics and Controlled Fusion **43** (2001) 1503

[17] G. D. Conway *et al.*, Plasma Physics and Controlled Fusion **44** (2002) xyz

[18] M. A. Beer, *Gyrofluid models of turbulent transport in tokamaks*, PhD thesis, 1995

[19] J. W. Connor *et al.*, IAEA Conference Montreal (1996) 935

[20] M. Kotschenreuther, W. Dorland *et al.*, Physics of Plasmas **2** (1995) 2381

[21] S.-I. Itoh, K. Itoh *et al.*, Plasma Physics and Controlled Fusion **38** (1996) 1743

[22] G. Bateman *et al.*, Physics of Plasmas **5** (1998) 1793

[23] M. Kotschenreuther *et al.*, Plasma Physics and Controlled Nuclear Fusion Research **2** (1992) 11

[24] R. E. Waltz *et al.*, Physics of Fluids B **4** (1992) 3138

[25] J. Weiland, *Collective Modes in Inhomogeneous Plasmas - Kinetic and Advanced Fluid Theory*, Institute of Physics Publishing, 1999

[26] B. Scott, Low frequency Fluid Drift Turbulence in magnetised Plasmas, IPP Report 5/92, 2001

[27] D. L. Book, NRL Plasma Formulary, NRL Publication (Revised 1987)

[28] S. C. Guo, J. Weiland, Nuclear Fusion, **37** (1997) 1095

[29] J. Stober *et al.*, Plasma Physics and Controlled Fusion, **42** (2000) A211

[30] W. Suttrop *et al.*, Plasma Physics and Controlled Fusion, **39** (1997) 2051

[31] G. Tardini *et al.*, Nuclear Fusion **42** (2002) 258

[32] H. Meister, Report of the Mak Planck Institut für Plasmaphysik IPP 10/16, (Garching Germany, 2000)

[33] W. Suttrop, A. G. Peeters, Report of the Mak Planck Institut für Plasmaphysik IPP 1/306 (Garching Germany, 1998)

[34] J. Schweinzer *et al.*, in Cont. Fusion and Plasma Physics (Proc. 22nd Eur. Conf. Bournemouth, 1995) **19 C** 253 (European Physical Society, Geneva 1995)

[35] E. Poli *et al.*, Computer Physics Communication **136** (2001) 90

[36] F. Ryter *et al.*, Nuclear Fusion **41** (2001) 537

[37] G. Janeschitz *et al.*, Proc. of the 26th EPS Conference, Maastricht, 1999, Europhysics Conference Abstracts, (EPS, Geneva) **23J** (1999) 1445

[38] G. V. Pereverzev, P. N. Yushmanov, *ASTRA Automated System for TRansport Analysis in a Tokamak*, IPP report 5/98, 2002

[39] S. P. Hirshman *et al.*, Nuclear Fusion Letters **17** (1977) 611

[40] Y. B. Kim *et al.*, Physics of Fluids **B3** (1991) 2050

[41] B. B.Kadomtsev, Sov. J. Plasma Phys. Vol.1, No.5, Sept.-Oct. (1975) pp.389-391

[42] C. S. Chang and F. L. Hinton, Physics of Fluids **25** (1982) 1493

[43] C. S. Chang and F. L. Hinton, Physics of Fluids **29** (1986) 3314

[44] A. Bergmann *et al.*, Physics of Plasmas **8** (2001) 5192

[45] A. A. Galeev and R. Z. Sagdeev, Voprosy Teorii Plasmy **7** (1973) 210

[46] R. E. Waltz *et al.*, Physics of Fluids B **4** (1992) 3138

[47] S.-I. Itoh *et al.*, Physical Review Letters **72** (1994) 1200

[48] G. M. Staebler *et al.*, Nuclear Fusion **37** (1997) 287

[49] F. Ryter *et al.*, Physical Review Letters **86** (2001) 2325

[50] G. Tardini *et al.*, Letter for Nuclear Fusion **42** (2002) L11

[51] D. Mikkelsen *et al*, 17th IAEA Fusion Energy Conference (Yokohama, 1998), IAEA-CN-69-ITERP1/08

[52] F. Ryter *et al.*, 29th EPS Conference, Montreaux, 2002, Poster 1.048

[53] L.-G. Eriksson, T. Hellsten, and U. Willén, Nuclear Fusion **33** (1993) 1037

[54] ITER Physics Basis, Nuclear Fusion **39** (1999) 2215

[55] G. V. Pereverzev, Physics of Plasmas **8** (2001) 3664

[56] C. Angioni *et al.*, *Density peaking, anomalous pinch and collisionality oin tokamak plasmas*, submitted to Physical Review Letters (2003)

[57] J. Stober *et al.*, Nuclear Fusion **41** (2001) 1535

Appendix A

List of frequently used abbreviations

	Heating and diagnostics systems
EC(R)H	Electron Cyclotron (Resonance) Heating
MECH	Modulated Electron Cyclotron Heating
NBI	Neutral Beam Injection
ICRH	Ion Cyclotron Resonance Heating
ECE	Electron Cyclotron Emission
CXRS	Charge eXchange Recombination Spectroscopy
	Experimental devices
ITER	International Thermonuclear Experimental Reactor
ASDEX	Axis-Symmetric Divertor EXperiment
JET	Joint European Torus
	Physics abbreviations
MHD	MagnetoHydroDynamics
ITB	Internal Transport Barrier
ITG	Ion Temperature Gradient
ETG	Electron Temperature Gradient
TEM	Trapped Electron Mode
χ^{PB}, χ^{pert}	Heat transport coefficient from Power Balance, perturbative analysis
ρ_{tor}	Toroidal flux coordinate
	Transport code and models
ASTRA	Automated System for TRansport Analysis
IFS/PPPL	Institute for Fusion Studies and Princeton Plasma Physics Laboratory
GLF23	Gyro Landau Fluid (from 2 dimensions and 3 dimensions simulations)
CDBM	Current Diffusive Ballooning Mode

Appendix B

Complements to the derivation of the Weiland model

B.1 Useful relations

In the derivation of the model, some relations are very useful to rewrite the equations in a simpler form. We report the most relevant:

$$\rho_s^2 = \frac{c_s^2}{\Omega_{ci}^2} = 2\rho_i^2\tau \tag{B.1}$$

$$v_{E_r} \approx \frac{E_{pol}B}{B^2} \approx -\frac{ik_y\phi}{B} \approx -i\frac{e\phi}{T_e}\frac{k_yT_e}{eB} = -i\frac{e\phi}{T_e}\omega_{\star e}L_n \tag{B.2}$$

$$\omega_{\star e} = -k_y\frac{T_e}{m_i}\frac{m_i}{eB}\frac{\nabla n_e}{n_e} = -k_y\frac{c_s^2}{\Omega_{ci}}\frac{\nabla n_e}{n_e} = \frac{k_\perp\rho_s c_s}{L_n} \tag{B.3}$$

$$\omega_{De} = 2\frac{k_\perp\rho_s c_s}{L_B} \tag{B.4}$$

$$\omega_{\star e} = -\tau\omega_{\star i} \tag{B.5}$$

$$\omega_{De} = -\tau\omega_{Di} \tag{B.6}$$

$$\frac{\omega_{Dj}}{\omega_{\star j}} = \epsilon_n \tag{B.7}$$

B.2 Estimate of the parallel ion motion

The equation for the parallel ion motion is obtained multiplying equation (3.5) by $\mathbf{e}_\parallel\cdot$:

$$\frac{\partial v_{\parallel i}}{\partial t} + \mathbf{v}_i\cdot\nabla v_{\parallel i} = \frac{e}{m_i}\mathbf{e}_\parallel\cdot\mathbf{E} - \frac{1}{m_in_i}\mathbf{e}_\parallel\cdot\nabla p_i = -\frac{c_s^2}{T_e}\mathbf{e}_\parallel\cdot\nabla\left(e\phi\right) - \frac{c_s^2}{p_e}\mathbf{e}_\parallel\cdot\nabla p_i \tag{B.8}$$

Since the equilibrium ∇T_e and ∇p_e are perpendicular to $\mathbf{e}_\parallel$, T_e and p_e are free to move inside $\mathbf{e}_\parallel\cdot\nabla$ in the first order equation. The linearised and Fourier transformed equation

is:

$$v_{\parallel i} \approx -i\frac{c_s^2}{\omega}\mathbf{e}_\parallel \cdot \nabla\left(\frac{e\phi}{T_e} + \frac{1}{\tau}\frac{\delta p_i}{p_i}\right) \tag{B.9}$$

We are interested in the quantity $\nabla \cdot \left(n\mathbf{v}_\parallel\right)$:

$$\nabla \cdot \left(n_i \mathbf{v}_{\parallel i}\right) = \mathbf{v}_{\parallel i} \cdot \nabla \tilde{n}_i + n_i \nabla \cdot \left(\frac{\mathbf{v}_i \cdot \mathbf{B}}{B^2}\mathbf{B}\right) \approx n_i \mathbf{B} \cdot \nabla\left(\frac{\mathbf{v}_i \cdot \mathbf{B}}{B^2}\right) + n_i \left(\frac{\mathbf{v}_i \cdot \mathbf{B}}{B^2}\right) \nabla \cdot \mathbf{B} \approx$$
$$\approx n_i k_\parallel v_{\parallel i} \approx n_i k_\parallel^2 \frac{c_s^2}{\omega}\left(\frac{e\phi}{T_e} + \frac{1}{\tau}\frac{\delta p_i}{p_i}\right) = -i\omega_{De} n_i \frac{|\hat{s}|}{2q}\left(\frac{e\phi}{T_e} + \frac{1}{\tau}\frac{\delta p_i}{p_i}\right) \tag{B.10}$$

The last passage is due to the strong ballooning approximation; the derivation is not immediate and can be found in [28]. The contribution from the parallel ion motion is not neglected in the Weiland model as it is a first order perturbative term. However, a common simplification treating drift waves is to neglect the parallel ion dynamics, so that "the diamagnetic must take place much faster than sound wave time scale" ([26], pag. 5.4), which means $k_\parallel c_s \ll \omega_\star \sim \omega$.

B.3 The dispersion relation

B.3.1 Curvature relations

To derive the useful relations

$$\nabla \cdot (n_j \mathbf{v}_{\star j}) = \frac{1}{T_j}\mathbf{v}_{Dj} \cdot \nabla \delta p_j \tag{B.11}$$

$$\nabla \cdot \mathbf{v}_E = \frac{2}{eB_0}\frac{q}{T}\mathbf{v}_D \cdot \nabla\phi \tag{B.12}$$

we start rewriting the ideal MHD equation:

$$\mu_0 \nabla p = \mu_0 \mathbf{j} \times \mathbf{B} = (\nabla \times \mathbf{B}) \times \mathbf{B} = -(\nabla \mathbf{B}) \cdot \mathbf{B} + (\mathbf{B} \cdot \nabla)\mathbf{B} = -\nabla\frac{B^2}{2} + (\mathbf{B} \cdot \nabla)\mathbf{B} \tag{B.13}$$

which leads to the pressure balance:

$$\nabla\left(p + \frac{1}{2\mu_0}B^2\right) = \frac{1}{\mu_0}(\mathbf{B} \cdot \nabla)\mathbf{B} \tag{B.14}$$

where $(\mathbf{B} \cdot \nabla)\mathbf{B}$ is the field curvature. Since $\nabla B_0 \approx B_0/R_c$ and $k_\parallel \sim 1/R$ (estimate valid for quasi-flute modes), the perturbation of the curvature term yields:

$$\delta(\mathbf{B} \cdot \nabla)\mathbf{B} \approx B_0 k_\parallel \delta\mathbf{B} + (\delta\mathbf{B} \cdot \nabla)\mathbf{B}_0 \sim k_\parallel B_0 \delta B \tag{B.15}$$

which is much smaller than $\delta\nabla B^2 \sim k_\perp B_0 \delta B$. Therefore,

$$\nabla\left(\delta p + \frac{1}{2\mu_0}\delta B^2\right) = 0 \tag{B.16}$$

But $\delta B^2 = \delta\left(\mathbf{B}_0 + \delta\mathbf{B}\right)^2 \approx 2\mathbf{B}_0 \cdot \delta\mathbf{B} = 2B_0\delta B_\parallel$, and hence

$$\delta B_\parallel = -\frac{\mu_0 \delta p}{B_0} \tag{B.17}$$

Besides, the following identity holds:

$$\mathbf{e}_\parallel \times (\mathbf{v}\times\mathbf{B}) = \Big(\mathbf{e}_\parallel \cdot \mathbf{B}\Big)\mathbf{v} - \Big(\mathbf{e}_\parallel \cdot \mathbf{v}\Big)\mathbf{B} \approx B_\parallel\Big(\mathbf{v} - v_\parallel \mathbf{e}_\parallel\Big) = B_\parallel \mathbf{v}_\perp = B_0\left(1 + \frac{\delta B_\parallel}{B_0}\right)\mathbf{v}_\perp \tag{B.18}$$

where a term $v_\parallel \delta B_\perp$ has been neglected. $\delta B_\perp = 0$ is due to the common approximation that $E_\perp$ is electrostatic. The divergence of $j_\parallel$ is:

$$\begin{aligned}
&\nabla\cdot\left[\left(n_i\mathbf{v}_{\star i} - n_e\mathbf{v}_{\star e}\right)\left(1 - \frac{\delta B_\parallel}{B_0}\right)\right] \approx \nabla\cdot\left[\frac{1}{eB_0}\left(1 - \frac{\delta B_\parallel}{B_0}\right)\Big(\mathbf{e}_\parallel \times \nabla p\Big)\right] = \\
&= \nabla\left[\frac{1}{eB_0}\left(1 - \frac{\delta B_\parallel}{B_0}\right)\right]\cdot\Big(\mathbf{e}_\parallel\times\nabla p\Big) + \frac{1}{eB_0}\left(1 - \frac{\delta B_\parallel}{B_0}\right)\nabla\cdot\Big(\mathbf{e}_\parallel\times\nabla p\Big)
\end{aligned} \tag{B.19}$$

where we have used quasi-neutrality. The linearised right hand side of equation B.19 is:

$$\begin{aligned}
&\nabla\left(\frac{1}{eB_0}\right)\cdot\Big(\mathbf{e}_\parallel\times\nabla\delta p\Big) - \nabla\left(\frac{\delta B_\parallel}{eB_0^2}\right)\cdot\Big(\mathbf{e}_\parallel\times\nabla p_0\Big) + \\
&-\frac{1}{eB_0}\frac{\delta B_\parallel}{B_0}\nabla\cdot\Big(\mathbf{e}_\parallel\times\nabla p_0\Big) + \frac{1}{eB_0}\nabla\cdot\Big(\mathbf{e}_\parallel\times\nabla\delta p\Big)
\end{aligned} \tag{B.20}$$

In the second term, the derivative of the denominator is negligible compared to that of the numerator if we assume with Weiland ([25] pag. 82)

$$\frac{\nabla B_0}{B_0} \ll \frac{\nabla\delta B_\parallel}{\delta B_\parallel} \tag{B.21}$$

The third term is negligible:

$$\begin{aligned}
&\nabla\cdot\Big(\mathbf{e}_\parallel\times\nabla p_0\Big) = \nabla p_0\cdot\Big(\nabla\times\mathbf{e}_\parallel\Big) - \mathbf{e}_\parallel\cdot\nabla\times(\nabla p_0) = \\
&= \nabla p_0\cdot\frac{1}{B_0}(\nabla\times\mathbf{B}_0) + \nabla p_0\cdot\left(\nabla\frac{1}{B_0}\times\mathbf{B}_0\right) = \frac{\mu_0}{B_0}\nabla p_0\cdot\mathbf{j}_0 - \nabla p_0\cdot\left(\frac{\nabla B_0}{B_0^2}\times\mathbf{B}_0\right) = \\
&= -\frac{\nabla B_0}{B_0}\cdot\Big(\mathbf{e}_\parallel\times\nabla p_0\Big)
\end{aligned} \tag{B.22}$$

and according to assumption B.21

$$\frac{\delta B_\parallel}{eB_0^3}\nabla B_0 \cdot \Big(\mathbf{e}_\parallel \times \nabla p_0\Big) \ll \nabla\left(\frac{\delta B_\parallel}{eB_0^2}\right) \cdot \Big(\mathbf{e}_\parallel \times \nabla p_0\Big) \tag{B.23}$$

Then the B.20 is approximately equal to:

$$\frac{1}{eB_0}\left(\mathbf{e}_\parallel \times \frac{\nabla B_0}{B_0}\right) \cdot \nabla\delta p + \frac{1}{eB_0}\Big(\nabla \times \mathbf{e}_\parallel\Big) \cdot \nabla\delta p + \frac{\mu_0}{eB_0^3}\Big(\mathbf{e}_\parallel \times \nabla p_0\Big) \cdot \delta p \tag{B.24}$$

where we have substituted from B.17 and used the vector identities (1), (9) and (15) from [27]. The quantity $\nabla \times \mathbf{e}_\parallel$ can be splitted into perpendicular and parallel component:

$$\Big(\nabla \times \mathbf{e}_\parallel\Big)_\perp = -\mathbf{e}_\parallel \times \Big[\mathbf{e}_\parallel \times \Big(\nabla \times \mathbf{e}_\parallel\Big)\Big] = \mathbf{e}_\parallel \times \Big(\mathbf{e}_\parallel \cdot \nabla\Big)\,\mathbf{e}_\parallel \tag{B.25}$$

$$\mathbf{e}_\parallel \cdot \Big(\nabla \times \mathbf{e}_\parallel\Big) = \frac{1}{B}\mathbf{e}_\parallel \cdot (\nabla \times \mathbf{B}) - \mathbf{e}_\parallel \cdot \left(\frac{\nabla B_0}{B_0^2} \times \mathbf{B}_0\right) = \frac{1}{B}\mathbf{e}_\parallel \cdot (\nabla \times \mathbf{B}) \tag{B.26}$$

The parallel component of $\nabla \times \mathbf{e}_\parallel$ is therefore associated with a background current, and results to be negligible because $k_\parallel$ is assumed to be small. The curvature vector is therefore:

$$\kappa = \Big(\mathbf{e}_\parallel \cdot \nabla\Big)\,\mathbf{e}_\parallel = -\frac{\mathbf{R}_c}{R_c^2} \tag{B.27}$$

From the B.14 applied to the background fields

$$\nabla B_0 = -\mu_0\frac{\nabla p_0}{B_0} + \Big(\mathbf{e}_\parallel \cdot \nabla\Big)\,\mathbf{B}_0 = -\mu_0\frac{\nabla p_0}{B_0} + B_0\Big(\mathbf{e}_\parallel \cdot \nabla\Big)\,\mathbf{e}_\parallel + \Big(\mathbf{e}_\parallel \cdot \nabla B_0\Big)\,\mathbf{e}_\parallel \approx$$

$$\approx -\mu_0\frac{\nabla p_0}{B_0} + B_0\Big(\mathbf{e}_\parallel \cdot \nabla\Big)\,\mathbf{e}_\parallel \tag{B.28}$$

one can substitute in the B.24 to obtain

$$\nabla \cdot \left[(n_i\mathbf{v}_{\star i} - n_e\mathbf{v}_{\star e})\left(1 - \frac{\delta B_\parallel}{B_0}\right)\right] \approx \frac{2}{eB_0}\Big(\mathbf{e}_\parallel \times \kappa\Big) \cdot \nabla\delta p \tag{B.29}$$

We note that:

1. Finite β (∇p_0 terms) terms cancel, justifying a low β treatment.
2. The divergence of the diamagnetic drift flux (diamagnetic current) is a curvature effect.

If we put $\mathbf{v}_E$ instead of $n_i\mathbf{v}_{\star i} - n_e\mathbf{v}_{\star e}$, we have $\nabla\phi/en$ instead of ∇p and we can make use of $\nabla\phi_0 = 0$:

$$\nabla \cdot \left[\mathbf{v}_E\left(1 - \frac{\delta B_\parallel}{B_0}\right)\right] = \frac{2}{eB_0}\frac{q}{T}\mathbf{v}_\kappa \cdot \nabla\phi \tag{B.30}$$

where we have introduced an effective curvature velocity $\mathbf{v}_{\kappa j} = 2\frac{T_j}{q_j B_0}\Big(\mathbf{e}_\parallel \times \kappa\Big)$. The low β approximation B.16 is actually assumed in the Weiland model, so that $\mathbf{v}_{\kappa j}$ reduces to $\mathbf{v}_{Dj}$ and B.29 holds for each species. Since $\delta\beta/B_o$ terms are neglected, B.29 and B.30 reduce to the simpler form B.11 and B.12.

B.3.2 Derivation of the diamagnetic heat flux

The closure of the Weiland model is obtained from the third momentum of the kinetic equation

$$0 = \frac{\partial}{\partial t}\int d^3\mathbf{w} f \frac{m_i}{2} w^2 \mathbf{w} + \nabla \cdot \int d^3\omega f \frac{m_i}{2} w^2 \mathbf{w}\mathbf{w} + \\ + \frac{q_i}{m_i}\int d^3\mathbf{w} \frac{m_i}{2} w^2 \mathbf{w}\mathbf{E} \cdot \frac{\partial f}{\partial \mathbf{w}} + \frac{q_i}{m_i}\int d^3\mathbf{w} \frac{m_i}{2} w^2 \mathbf{w} \left(\mathbf{w} \times \mathbf{B}\right) \cdot \frac{\partial f}{\partial \mathbf{w}} \tag{B.31}$$

neglecting collisions (first term). Besides, we set $\mathbf{E} = 0$ to isolate the diamagnetic part. The fourth term can be integrated by parts, and since $\left(\mathbf{w} \times \mathbf{B}\right)_x$ contains only w_y and w_z, it is not affected by $\partial/\partial w_x$. So we must calculate

$$\int d^3\mathbf{w} \frac{m_i}{2} f \frac{\partial}{\partial \mathbf{w}} \left(w^2 \mathbf{w}\right) \cdot \left(\mathbf{w} \times \mathbf{B}\right) = \\ \int d^3\mathbf{w} \frac{m_i}{2} f \left(w^2 \boldsymbol{I} + 2\mathbf{w}\right) \cdot \left(\mathbf{w} \times \mathbf{B}\right) = \int d^3\mathbf{w} \frac{m_i}{2} f w^2 \boldsymbol{I} \cdot \left(\mathbf{w} \times \mathbf{B}\right) \tag{B.32}$$

The fourth momentum (second term in B.31) is evaluated setting f Maxwellian (see [26], page 2.35). In particular f is isotropic, so that $i \neq j$ yields $\int w^2 w_i w_j f = 0$ and w_i^2 can be replaced by $1/3w^2$:

$$\nabla \cdot \int d^3\mathbf{w} \frac{m_i}{2} w^2 \mathbf{w}\mathbf{w} f = \frac{m_i}{2} \nabla \cdot \left(\frac{1}{3}\boldsymbol{I} \int d^3\omega w^4 f\right) = \frac{\pi m_i}{3} \nabla \int_0^{+\infty} dw w^6 f \tag{B.33}$$

This is a known Gaussian integral:

$$\int_0^{+\infty} dw w^6 \alpha e^{-aw^2} = \alpha \frac{15}{16a^3}\sqrt{\frac{\pi}{a}} \tag{B.34}$$

α can be determined from the definition of the ion density:

$$n_i = \int d^3w f = 2\pi \int_0^{+\infty} dw w^2 \alpha e^{-aw^2} = 2\pi\alpha \left(-\frac{\partial}{\partial a}\frac{1}{2}\sqrt{\frac{\pi}{a}}\right) = \pi\alpha\sqrt{\pi}\frac{1}{2}a^{-3/2} \\ \alpha = 2n_i \left(\frac{a}{\pi}\right)^{3/2} \tag{B.35}$$

In our case, $a = m_i/2T$, so the whole B.33 is

$$\nabla \cdot \int d^3w \frac{m_i}{2} w^2 \mathbf{w}\mathbf{w} f = \nabla \left(\frac{5}{8}\frac{m_i n}{a^2}\right) = \nabla \left(\frac{5}{2}\frac{pT}{m_i}\right) \tag{B.36}$$

Equation B.31 reduces to the form:

$$\nabla \left(\frac{5}{2}\frac{p_i T_i}{m_i}\right) = \frac{q_i}{m_i}\left(\int d^3w \frac{m_i}{2} f w^2 \mathbf{w}\right) \times \mathbf{B} \tag{B.37}$$

The term in round brackets is known to be (see [26], pag. 2.161)

$$\int d^3\omega \frac{m_i}{2} f w^2 \mathbf{w} = \mathbf{q}_i + \left(\frac{3}{2} n_i T_i + p_i + n_i m_i \frac{v_i^2}{2}\right) \mathbf{v}_i \tag{B.38}$$

The fluid velocity reduces to the diamagnetic because we set $\mathbf{E} = 0$. Isotropy ensures $p_i = n_i T_i$ and in addition we assume $m_i \mathbf{v}_{\star i}^2 \ll T_i$, so it remains:

$$\nabla \left(\frac{5}{2} \frac{p_i T_i}{m_i}\right) = \frac{q_i}{m_i} \left(\frac{5}{2} p_i \mathbf{v}_{\star i} + \mathbf{q}_{\star i}\right) \times \mathbf{B} \tag{B.39}$$

which multiplied times $\frac{m_i}{q_i B^2} B\times$ yields:

$$\begin{aligned} \frac{5}{2} p_i \mathbf{v}_{\star i} + \mathbf{q}_{\star i} &= \frac{1}{q_i B^2} \mathbf{B} \times \nabla \left(\frac{5}{2} p_i T_i\right) \\ \mathbf{q}_{\star i} &= \frac{5}{2} \frac{p_i}{q_i B^2} \mathbf{B} \times \nabla T_i \end{aligned} \tag{B.40}$$

B.3.3 The temperature perturbation

We want to calculate $\delta T_i / T_i$. We can rewrite 3.7 as:

$$\frac{3}{2} \left(\frac{\partial}{\partial t} + \mathbf{v}_j \cdot \nabla\right) p_j + \frac{5}{2} p_j \nabla \cdot \mathbf{v}_j + \pi : \nabla \mathbf{v}_j + \nabla \cdot \mathbf{q}_j = Q_j + S_{Ej} - \frac{1}{2} m_j v_j^2 S_{nj} \tag{B.41}$$

Of course there are no external sources which contribute at the first perturbative order, because either they do not vary in time or they do, but much slowlier. Neglecting the Coulombian terms as well as the contribution from the stress tensor, it remains:

$$\frac{3}{2} n_i \left(\frac{\partial}{\partial t} + \mathbf{v}_i \cdot \nabla\right) T_i + P_i \nabla \cdot \mathbf{v}_i = -\nabla \cdot \mathbf{q}_{\star i} \tag{B.42}$$

The Righi-Leduc or diamagnetic flow $\mathbf{q}_{\star i}$ has the form B.40.
In analogy with the equation B.22, assuming $\nabla T_i \perp \mathbf{j}$, it is

$$\frac{P_i}{e} \nabla \cdot \left(\frac{\mathbf{B}}{B^2} \times \nabla T_i\right) = \frac{P_i}{e} \nabla T_i \cdot \left(\nabla \frac{1}{B^2} \times \mathbf{B}\right) = -2 \frac{n_i T_i}{eB} \nabla T_i \cdot \left(\frac{\nabla B}{B^2} \times \mathbf{B}\right) = n_i \nabla T_i \cdot \mathbf{v}_{Di} \tag{B.43}$$

Therefore, the divergence of the diamagnetic heat flux can be rewritten through the vector identities (9), (15) and (1) of Ref. [27] in the form:

$$\begin{aligned} \nabla \cdot \mathbf{q}_{\star i} = \frac{5}{2} \nabla \cdot \left[\frac{P_i}{eB} \left(\mathbf{e}_\parallel \times \nabla T_i\right)\right] = \frac{5}{2eB} \nabla P_i \cdot \left(\mathbf{e}_\parallel \times \nabla T_i\right) + \frac{5}{2} \frac{P_i}{e} \nabla \cdot \left(\frac{\mathbf{B}}{B^2} \times \nabla T_i\right) = \\ \frac{5}{2eB} \nabla T_i \cdot \left(\nabla P_i \times \mathbf{e}_\parallel\right) + \frac{5}{2} n_i \nabla T_i \cdot \mathbf{v}_{Di} = -\frac{5}{2} n \mathbf{v}_{\star i} \cdot \nabla T_i + \frac{5}{2} n \mathbf{v}_{Di} \cdot \nabla T_i \end{aligned} \tag{B.44}$$

Combining it to the 3.6 we have

$$\frac{3}{2}n_i\left(\frac{\partial}{\partial t}+\mathbf{v}_i\cdot\nabla\right)T_i+P_i\nabla\cdot\mathbf{v}_i=\frac{5}{2}n_i\mathbf{v}_{\star i}\cdot\nabla T_i-\frac{5}{2}n_i\mathbf{v}_{Di}\cdot\nabla T_i \tag{B.45}$$

We neglect the terms containing $k^2\rho_s^2$ (that is, $\mathbf{v}_i\approx\mathbf{v}_E+\mathbf{v}_{\star i}$), and use $\nabla\cdot(n_i\mathbf{v}_i)=-\frac{\partial n_i}{\partial t}$ from the continuity equation; furthermore, $\frac{3}{2}n_i\mathbf{v}_{\star i}\cdot\nabla T_i-T_i\mathbf{v}_{\star i}\cdot\nabla n_i$ cancels with $\frac{5}{2}n_i\mathbf{v}_{\star i}\cdot\nabla T_i$ since by definition $\mathbf{v}_{\star i}\cdot\nabla(n_iT_i)=0$. The B.45 becomes:

$$\begin{aligned}-\frac{5}{2}n_i\mathbf{v}_{Di}\cdot\nabla T_i&=\frac{3}{2}n_i\frac{\partial T_i}{\partial t}+\frac{3}{2}n_i\mathbf{v}_E\cdot\nabla T_i+T_i\left[-\nabla\cdot(n_i\mathbf{v}_i)-\mathbf{v}_E\cdot\nabla n_i\right]=\\ &\frac{3}{2}n_i\frac{\partial T_i}{\partial t}+\frac{3}{2}\mathbf{v}_E\cdot\left(n_i\nabla T_i-\frac{2}{3}T_i\nabla n_i\right)-T_i\frac{\partial n_i}{\partial t}\end{aligned} \tag{B.46}$$

The linearised equation, multiplied by $2/(3n_iT_i)$ and Fourier transformed, reads:

$$i\omega\frac{\delta T_i}{T_i}-i\omega_{\star e}\frac{e\phi}{T_e}\cdot\left(\eta_i-\frac{2}{3}\right)-\frac{2}{3}i\omega\frac{\delta n_i}{n_i}=\frac{5}{3}i\omega_{Di}\frac{\delta T_i}{T_i} \tag{B.47}$$

where we evaluated

$$-\nabla n_i\cdot\mathbf{v}_E=-\frac{\nabla n_i ik_y\phi}{B}=-\frac{T_e\nabla n_i ik_y}{eB}\frac{e\phi}{T_e}\approx-i\omega_{\star e}n_i\frac{e\phi}{T_e} \tag{B.48}$$

This delivers the relative temperature perturbation

$$\frac{\delta T_i}{T_i}=\frac{\omega}{\omega-5\omega_{Di}/3}\left[\frac{2}{3}\frac{\delta n_i}{n_i}+\frac{\omega_{\star e}}{\omega}\left(\eta_i-\frac{2}{3}\right)\frac{e\phi}{T_e}\right] \tag{B.49}$$

B.3.4 The contribution from the stress tensor drift

An estimate of the divergence of the pressure anisotropy drift is required. Large mode numbers are assumed, i.e. $k\gg\kappa_p=|\nabla\ ln\ p_0|$. Besides, $\nabla\kappa_p=0$ and the magnetic field is taken to be homogeneous, such that $\hat{z}=\mathbf{B}/B$ is uniform. The stress tensor is defined (see equation (2.21) of [9]):

$$\begin{aligned}\pi_{xy}=\pi_{yx}&=\frac{p}{2\Omega_c}\left(\frac{\partial v_x}{\partial x}-\frac{\partial v_y}{\partial y}\right)+\frac{1}{4\Omega_c}\left(\frac{\partial q_x}{\partial x}-\frac{\partial q_y}{\partial y}\right)\\ \pi_{yy}=-\pi_{xx}&=\frac{p}{2\Omega_c}\left(\frac{\partial v_y}{\partial x}+\frac{\partial v_x}{\partial y}\right)+\frac{1}{4\Omega_c}\left(\frac{\partial q_y}{\partial x}+\frac{\partial q_x}{\partial y}\right)\end{aligned} \tag{B.50}$$

The $\mathbf{q}$ terms are formally identical to the $\mathbf{v}$ ones, so they will be dropped for simplicity and recovered finally. The background density and temperature have no poloidal variation, so in our notation $dn_o/dy=dT_o/dy=0$.

$$(\nabla\cdot\pi)_x=\frac{\partial\pi_{xx}}{\partial x}+\frac{\partial\pi_{xy}}{\partial y}=-\frac{p}{2\Omega_c}\left(\frac{\partial^2 v_y}{\partial x^2}+\frac{\partial^2 v_x}{\partial x\partial y}\right)-\frac{1}{2\Omega_c}\left(\frac{\partial v_y}{\partial x}+\frac{\partial v_x}{\partial y}\right)\frac{dp}{dx}+$$

$$+\frac{p}{2\Omega_c}\left(\frac{\partial^2 v_x}{\partial x\partial y}-\frac{\partial^2 v_y}{\partial y^2}\right)=-\frac{p}{2\Omega_c}\triangle v_y+\frac{p}{2\Omega_c}\kappa_p\left(\frac{\partial v_y}{\partial x}+\frac{\partial v_x}{\partial y}\right)$$
$$(\nabla\cdot\pi)_y=\frac{\partial \pi_{yx}}{\partial x}+\frac{\partial \pi_{yy}}{\partial y}=\frac{p}{2\Omega_c}\left(\frac{\partial^2 v_x}{\partial x^2}-\frac{\partial^2 v_y}{\partial x\partial y}\right)+\frac{1}{2\Omega_c}\left(\frac{\partial v_x}{\partial x}-\frac{\partial v_y}{\partial y}\right)\frac{dp}{dx}+$$
$$+\frac{p}{2\Omega_c}\left(\frac{\partial^2 v_y}{\partial x\partial y}+\frac{\partial^2 v_x}{\partial y^2}\right)=\frac{p}{2\Omega_c}\triangle v_x-\frac{p}{2\Omega_c}\kappa_p\left(\frac{\partial v_x}{\partial x}-\frac{\partial v_y}{\partial y}\right)$$

Writing in a more compact form, and reintroducing $\mathbf{q}$:

$$\nabla\cdot\pi=\frac{p}{2\Omega_c}\left[\hat{z}\times\triangle_\perp\mathbf{v}+\kappa_p\left(\nabla v_y-\hat{z}\times\nabla v_x\right)\right]+\frac{1}{4\Omega_c}\hat{z}\times\triangle_\perp\mathbf{q}_\star^\perp \tag{B.51}$$

where $\mathbf{q}_\star^\perp$ is the part of $\mathbf{q}_\star$ corresponding to a flux of perpendicular energy (reference [2.12] in Weiland's):

$$\mathbf{q}_\star^\perp=2\frac{p_\perp}{m\Omega_c}\left(\hat{z}\times\nabla T_\perp\right) \tag{B.52}$$

Omitting terms containing ρ_i/L_B, the anisotropy drift flux can be written as

$$n\mathbf{v}_\pi=\frac{1}{eB}\hat{z}\times\nabla\cdot\pi=\frac{1}{2m\Omega_c^2}\left[-p\triangle_\perp\mathbf{v}+p\kappa_p\left(\hat{z}\times\nabla v_y+\nabla v_x\right)-\frac{1}{2}\triangle_\perp\mathbf{q}_\star^\perp\right] \tag{B.53}$$

We note that since we have not considered the B-curvature

$$\nabla\cdot\left(\hat{z}\times\nabla v_y\right)=\nabla v_y\cdot\left(\nabla\times\hat{z}\right)-\hat{z}\cdot\left(\nabla\times\nabla v_y\right)=0 \tag{B.54}$$

We neglect terms which are not linear in κ_p, because $\kappa_p\ll k$. B can be taken out of all ∇'s for the low β approximation B.21.

$$\nabla\cdot(n\mathbf{v}_\pi)=\frac{1}{2m\Omega_c^2}\left(-\nabla p\cdot\triangle_\perp\mathbf{v}-p\nabla\cdot\triangle_\perp\mathbf{v}+p\kappa_p\triangle v_x-\frac{1}{2}\nabla\cdot\triangle_\perp\mathbf{q}_\star^\perp\right)=$$
$$=\frac{1}{2m\Omega_c^2}\left(-\nabla p\cdot\triangle_\perp\mathbf{v}-p\triangle_\perp\nabla\cdot\mathbf{v}+p\kappa_p\triangle v_x-\frac{1}{2}\triangle_\perp\nabla\cdot\mathbf{q}_\star^\perp\right) \tag{B.55}$$

In absence of B-curvature, the divergence of the electrostatic drift velocity zero (see B.12); the divergence of the diamagnetic drift velocity and diamagnetic heat flux are of higher order in δ:

$$\nabla\cdot\mathbf{v}_\star=\frac{1}{eB}\nabla\cdot\left(\frac{\hat{z}\times\nabla p}{n}\right)=\frac{1}{eB}\nabla\left(\frac{1}{n}\right)\cdot\left(\hat{z}\times\nabla p\right)=-\frac{\nabla n}{n}\cdot\mathbf{v}_\star\propto\delta n\mathbf{v}_\star\approx 0 \tag{B.56}$$

$$\nabla\cdot\mathbf{q}_\star=\frac{1}{eB}\nabla p\cdot\left(\hat{z}\times\nabla T\right)=-\nabla T\cdot\mathbf{v}_\star\propto\delta T\mathbf{v}_\star\approx 0$$

At order zero ∇p is in the radial direction and therefore $\nabla p/p\cdot=-\kappa_p\partial/\partial x$. Equation B.55 can be simplified:

$$\nabla\cdot(n\mathbf{v}_\pi)=\frac{1}{m\Omega_c^2}\kappa_p\triangle v_x$$

B.3.5 The polarisation drift

The polarisation drift in the simplified geometry is defined as

$$\mathbf{v}_p = \frac{1}{\Omega_c}\left(\frac{\partial}{\partial t} + \mathbf{v}\cdot\nabla\right)(\hat{z}\times\mathbf{v}) \tag{B.57}$$

Due to the large mode number approximation, only perturbed velocities enter the last $\mathbf{v}$. In the linear approximation, the only relevant convective derivative $\mathbf{v}\cdot\nabla$ is the one containing the background $\mathbf{v}$. As usual we set $E = 0$ and we isolate the diamagnetic drift, which results to be the only background velocity. The contributions to $\nabla\cdot(n\mathbf{v}_p)$ are:

$$\frac{1}{\Omega_c}\, n\mathbf{v}_\star^j\, \partial_j\partial_i\left(\hat{z}\times\mathbf{v}\right)^i = \frac{n}{\Omega_c}\left(\mathbf{v}_\star\cdot\nabla\right)\nabla\cdot(\hat{z}\times\mathbf{v}) \tag{B.58}$$

$$\frac{1}{\Omega_c}\,\partial_i\left(n\mathbf{v}_\star^j\right)\,\partial_j\left(\hat{z}\times\mathbf{v}\right)^i = \frac{1}{\Omega_c}\nabla\left(n\mathbf{v}_\star\right):\nabla\left(\hat{z}\times\mathbf{v}\right) \tag{B.59}$$

$$\nabla\cdot\left[\frac{n}{\Omega_c}\frac{\partial}{\partial t}\left(\hat{z}\times\mathbf{v}\right)\right] \tag{B.60}$$

We evaluate the B.58 and the B.59:

$$\frac{n}{\Omega_c}\left(\mathbf{v}_\star\cdot\nabla\right)\nabla\cdot(\hat{z}\times\mathbf{v}) = \frac{n}{\Omega_c}\mathbf{v}_\star\cdot\nabla\left(\frac{\partial v_x}{\partial y} - \frac{\partial v_y}{\partial x}\right) = -\frac{1}{m\Omega_c^2}p\kappa_p\frac{\partial}{\partial y}\left(\frac{\partial v_x}{\partial y} - \frac{\partial v_y}{\partial x}\right) \tag{B.61}$$

$$\frac{1}{\Omega_c}\,\partial_i\left(nv_\star^j\right)\,\partial_j\left(\hat{z}\times\mathbf{v}\right)^i = -\frac{1}{\Omega_c eB}\nabla\left(p\kappa_p\right)\cdot\frac{\partial}{\partial y}\left(\hat{z}\times\mathbf{v}\right) \approx 0 \tag{B.62}$$

Now we put these results together with the divergence of the flux related to the anisotropy drift.

$$\begin{aligned}\nabla\cdot(n\mathbf{v}_\pi) + \frac{n}{\Omega_c}\left(\mathbf{v}_\star\cdot\nabla\right)\nabla\cdot(\hat{z}\times\mathbf{v}) &= \frac{1}{m\Omega_c^2}\left[\kappa_p\triangle v_x - \kappa_p\frac{\partial}{\partial y}\left(\frac{\partial v_x}{\partial y} - \frac{\partial v_y}{\partial x}\right)\right] = \\ = \frac{1}{m\Omega_c^2}\left[\kappa_p\triangle v_x - \kappa_p\left(\triangle v_x - \frac{\partial^2 v_x}{\partial x^2} - \frac{\partial^2 v_y}{\partial x\partial y}\right)\right] &= \frac{1}{m\Omega_c^2}\kappa_p\frac{\partial}{\partial x}\nabla\cdot\mathbf{v} \approx 0\end{aligned} \tag{B.63}$$

To the leading order the last term is zero due to equation B.56 and because $\nabla\cdot\mathbf{v}_E \approx 0$. "The convective diamagnetic contribution to $\nabla\cdot(n\mathbf{v}_p)$ are exactly cancelled by the stress tensor contribution $\nabla\cdot(n\mathbf{v}_\pi)$." ([25], pag. 21). The following relation holds:

$$\nabla\cdot\left[n\left(\mathbf{v}_p + \mathbf{v}_\pi\right)\right] = \nabla\cdot\left[\frac{n}{\Omega_c}\frac{\partial}{\partial t}\left(\hat{z}\times\mathbf{v}\right)\right] \tag{B.64}$$

Substituting the leading orders drifts according to equations B.11 and B.12 gives:

$$\begin{aligned}\frac{n_i}{\Omega_{ci}}\frac{\partial}{\partial t}\nabla\cdot(\hat{z}\times\mathbf{v}_E) &= -\frac{n_i}{\Omega_{ci}}\frac{\partial}{\partial t}\frac{\partial}{\partial x}v_{E,x} = -\frac{n_i T_i}{m\Omega_{ci}^2}\frac{\partial}{\partial t}\triangle\frac{e\phi}{T_i} = -2n_i\rho_i^2\frac{\partial}{\partial t}\triangle\frac{e\phi}{T_i} \\ \frac{n}{\Omega_{ci}}\frac{\partial}{\partial t}\nabla\cdot(\hat{z}\times\mathbf{v}_{\star i}) &= -2n_i\rho_i^2\frac{\partial}{\partial t}\triangle\delta p_i\end{aligned}$$

We choose a particular density response, the simplest leading order of flute modes, that is the convective contribution, so that the pressure perturbation results to be:

$$\frac{\delta p_i}{p_i} = -\frac{\omega_{\star iT}}{\omega}\frac{e\phi}{T_i} \tag{B.65}$$

Remembering that $\rho_s^2 = T_e/m_i\Omega_{ci}^2 = 2\rho_i^2\tau$, we obtain the useful relation

$$\nabla\cdot\left[n\left(\mathbf{v}_{pi}+\mathbf{v}_{\pi i}\right)\right] \approx -2n\rho_i^2\left(ik^2\frac{e\phi}{T_i} - ik^2\omega_{\star iT}\frac{e\phi}{T_i}\right) = -ink^2\rho_s^2\frac{e\phi}{T_e}\left(\omega-\omega_{\star iT}\right) \tag{B.66}$$

B.3.6 The density perturbations

We need to evaluate the four remaining contributions to equation 3.12:

$$\begin{aligned}
&(I)\ \ -\nabla n_i\cdot\mathbf{v}_E \approx -i\omega_{\star e}n_i\frac{e\phi}{T_e}\\
&(II)\ \ -n_i\nabla\cdot\mathbf{v}_E = -n_i\frac{e}{T_i}\mathbf{v}_{Di}\cdot\nabla\phi = -i\frac{\omega_{Di}}{T_i}n_ie\phi \approx -i\omega_{De}n_e\frac{e\phi}{T_e}\\
&(III)\ \ -\nabla\cdot\left[n_i\left(\mathbf{v}_{pi}+\mathbf{v}_{\pi i}\right)\right] = in_ik^2\rho_s^2\left(\omega-\omega_{\star iT}\right)\frac{e\phi}{T_e}\\
&(IV)\ \ -\nabla\cdot\left(n_i\mathbf{v}_{\star i}\right) = -\frac{1}{T_i}\mathbf{v}_{Di}\cdot\nabla\delta P_i = -\frac{1}{T_i}\mathbf{v}_{Di}\cdot\nabla\left(T_i\delta n_i + n_i\delta T_i\right) =\\
&= -i\omega_{Di}\left\{\delta n_i + n_i\frac{\omega}{\omega-5\omega_{Di}/3}\left[\frac{2}{3}\frac{\delta n_i}{n_i}+\frac{\omega_{\star e}}{\omega}\left(\eta_i-\frac{2}{3}\right)\frac{e\phi}{T_e}\right]\right\}
\end{aligned}$$

We have made use of the equation B.48 for (I), B.12 for (II), B.66 for (III) and finally equations B.11 and B.49 for the relation (IV). We note that the term $k^2\rho_s^2$ is stabilising and quadratic in k, so that too short wavelengths are not accessible. The ion density perturbation, given by $-i\omega\ \delta n_i = I\ +\ II\ +\ III\ +\ IV$, times i/n_i is therefore

$$\begin{aligned}
&\frac{\delta n_i}{n_i}\left(\omega-\omega_{Di}-\frac{2}{3}\frac{\omega\omega_{Di}}{\omega-5\omega_{Di}/3}\right) =\\
&= \frac{e\phi}{T_e}\left[-k^2\rho_s^2\left(\omega-\omega_{\star iT}\right)+\frac{\omega_{Di}\omega_{\star e}}{\omega-5\omega_{Di}/3}\left(\eta_i-\frac{2}{3}\right)+\omega_{\star e}-\omega_{De}\right]
\end{aligned} \tag{B.67}$$

We multiply the B.67 times $\omega-5\omega_{Di}/3$ and then divide by $N_i = \omega^2-\omega_{Di}5/3+\omega_{Di}^2 10/3$:

$$\begin{aligned}
&\frac{\delta n_i}{n_i} = \frac{e\phi}{T_e}\frac{1}{N_i}\frac{1}{\epsilon_n}\omega_{De}^2\left[-\hat{\omega}^2k^2\rho_s^2\epsilon_n+\hat{\omega}\left(1-\epsilon_n-\frac{5}{3}k^2\rho_s^2\frac{\epsilon_n}{\tau}-k^2\rho_s^2\frac{1+\eta_i}{\tau}\right)+\right.\\
&\left.-\frac{1}{\tau}\left(\eta_i-\frac{7}{3}+\frac{5}{3}\epsilon_n\right)-k^2\rho_s^2\frac{5}{3\tau^2}\left(1+\eta_i\right)\right]
\end{aligned} \tag{B.68}$$

A similar equation holds for trapped electrons:

$$\frac{\delta n_{et}}{n_{et}} = \frac{e\phi}{T_e}\frac{1}{N_e}\frac{\omega_{\star e}}{\omega_{De}}\left[\omega\omega_{De}\left(1-\epsilon_n\right)+\omega_{De}^2\left(\eta_e-\frac{7}{3}+\frac{5}{3}\epsilon_n\right)\right]=$$
$$=\frac{e\phi}{T_e}\frac{1}{\hat{N}_e}\frac{1}{\epsilon_n}\left[\hat{\omega}\left(1-\epsilon_n\right)+\left(\eta_e-\frac{7}{3}+\frac{5}{3}\epsilon_n\right)\right]=\frac{e\phi}{T_e}A_e \tag{B.69}$$

where the definition of A_e 3.26 is used.

B.4 Quasi-linear diffusion

We already know the temperature perturbation B.49, now we substitute there $\delta n_i/n_i$ from B.69 and 3.2 via quasi-neutrality. This allows to close the system of equations and to estimate the ion heat flux 3.25 and therefore the quasi linear ion heat diffusivity:

$$\chi_i = -\frac{\Gamma_{T_i}}{\nabla T_i} = -Re\left\{i\frac{\gamma}{k_x}\frac{1}{\omega-\frac{5}{3}\omega_{Di}}\frac{T_i}{\nabla T_i}\frac{\gamma}{k_x L_n}\left[\frac{2}{3}\frac{\omega}{\omega_{\star e}}\left(1-f_t+f_t A_e\right)+\eta_i-\frac{2}{3}\right]\right\}=$$
$$=Re\left\{i\frac{\gamma^2}{k_x^2}\frac{1}{\eta_i}\frac{\bar{\omega}-5\omega_{Di}/3}{\left(\omega_r-5\omega_{Di}/3\right)^2+\gamma^2}\left[\frac{2}{3}\frac{\omega}{\omega_{\star e}}\left(1-f_t+f_t A_e\right)+\eta_i-\frac{2}{3}\right]\right\}$$

We normalise frequencies as usual to ω_{De} and define $\bar{\omega}^\star = \bar{\omega}/\omega_{De}$.

$$\chi_i = \frac{\hat{\gamma}^2}{k_x^2}\frac{\omega_{De}}{\eta_i}\frac{1}{\left(\hat{\omega}_r+5/3\tau\right)^2+\hat{\gamma}^2}$$
$$\left\{-Im\left[\frac{2}{3}\epsilon_n\left(|\hat{\omega}|^2+\frac{5\hat{\omega}}{3\tau}\right)\left(1-f_t+f_t A_e\right)+\left(\bar{\omega}^\star+\frac{5}{3\tau}\right)\left(\eta_i-\frac{2}{3}\right)\right]\right\} \tag{B.70}$$

Let's focus on $-Im\left[\ \right]$:

$$-Im\left[\ \right] = -\frac{2}{3}\epsilon_n f_t|\hat{\omega}|^2 Im\left(A_e\right)-\frac{10}{9}\hat{\gamma}\frac{\epsilon_n}{\tau}\left(1-f_t\right)-\frac{10}{9}\frac{\epsilon_n}{\tau}f_t Im\left(\bar{\omega}^\star A_e\right)+\hat{\gamma}\left(\eta_i-\frac{2}{3}\right)=$$
$$=\hat{\gamma}\left[\eta_i-\frac{2}{3}-\left(1-f_t\right)\frac{10}{9}\frac{\epsilon_n}{\tau}-\frac{2}{3}f_t\Delta_i\right] \tag{B.71}$$

where

$$\Delta_i = \frac{1}{\hat{\gamma}}\left(|\hat{\omega}|^2+\frac{5}{3\tau}\hat{\omega}_r\right)Im\left(\epsilon_n A_e\right)+\frac{5}{3\tau}Re\left(\epsilon_n A_e\right) \tag{B.72}$$

So we have for χ_i exactly the expression 3.27, provided we derive the correspondent expression 3.28 for Δ_i. We remind that

$$\epsilon_n A_e = \frac{1}{\hat{N}_e}\left[\hat{\omega}\left(1-\epsilon_n\right)+\left(\eta_e-\frac{7}{3}+\frac{5}{3}\epsilon_n\right)\right] \tag{B.73}$$

Let's rationalise $1/\hat{N}_e$:

$$\frac{1}{\hat{N}_e} = \frac{\bar{\omega}^{\star 2}-\bar{\omega}^\star 10/3+5/3}{\hat{N}} = \frac{\hat{\omega}_r^2-\hat{\gamma}^2-\hat{\omega}_r 10/3+5/3+i\hat{\gamma}\left(-2\hat{\omega}_r+10/3\right)}{\hat{N}} \tag{B.74}$$

We want to evaluate Re and Im:

$$\hat{N}\ Re\left(\epsilon_n A_e\right) = \left(\hat{\omega}_r^2 - \hat{\gamma}^2 - \frac{10}{3}\hat{\omega}_r + \frac{5}{3}\right)\left[\hat{\omega}_r\left(1-\epsilon_n\right) + \left(\eta_e - \frac{7}{3} + \frac{5}{3}\epsilon_n\right)\right] +$$
$$-\hat{\gamma}^2\left(1-\epsilon_n\right)\left(-2\hat{\omega}_r + \frac{10}{3}\right) = \left(1-\epsilon_n\right)\left(\hat{\omega}_r^3 + \hat{\omega}_r\hat{\gamma}^2 - \frac{10}{3}\hat{\omega}_r^2 - \frac{10}{3}\hat{\gamma}^2 + \frac{5}{3}\hat{\omega}_r\right) +$$
$$+\left(\hat{\omega}_r^2 - \hat{\gamma}^2 - \frac{10}{3}\hat{\omega}_r + \frac{5}{3}\right)\left(\eta_e - \frac{7}{3} + \frac{5}{3}\epsilon_n\right) \tag{B.75}$$

$$\hat{N}\ Im\left(\epsilon_n A_e\right) = \left(\hat{\omega}_r^2 - \hat{\gamma}^2 - \frac{10}{3}\hat{\omega}_r + \frac{5}{3}\right)\hat{\gamma}\left(1-\epsilon_n\right) +$$
$$+\hat{\gamma}\left(-2\hat{\omega}_r + \frac{10}{3}\right)\left[\hat{\omega}_r\left(1-\epsilon_n\right) + \left(\eta_e - \frac{7}{3} + \frac{5}{3}\epsilon_n\right)\right] =$$
$$= \hat{\gamma}\left(1-\epsilon_n\right)\left(-\hat{\omega}_r^2 - \hat{\gamma}^2 + \frac{5}{3}\right) + \hat{\gamma}\left(-2\hat{\omega}_r + \frac{10}{3}\right)\left(\eta_e - \frac{7}{3} + \frac{5}{3}\epsilon_n\right) \tag{B.76}$$

So substituting in B.72 after some algebra we obtain the expression for Δ_i contained in equation 3.28:

$$\Delta_i = \frac{1}{\hat{N}}\left\{|\hat{\omega}|^2\left[-|\hat{\omega}|^2\left(1-\epsilon_n\right) + \frac{5}{3}\left(1-\epsilon_n\right) + 2\left(-\hat{\omega}_r + \frac{5}{3}\right)\left(\eta_e - \frac{7}{3} + \frac{5}{3}\epsilon_n\right)\right] +\right.$$
$$+\frac{5}{3\tau}\left[-|\hat{\omega}|^2\hat{\omega}_r\left(1-\epsilon_n\right) + \frac{5}{3}\hat{\omega}_r\left(1-\epsilon_n\right) - 2\hat{\omega}_r^2\left(\eta_e - \frac{7}{3} + \frac{5}{3}\epsilon_n\right) + \frac{10}{3}\hat{\omega}_r\left(\eta_e - \frac{7}{3} + \frac{5}{3}\epsilon_n\right) +\right.$$
$$\left.\left. + \left(1-\epsilon_n\right)\left(|\hat{\omega}|^2\hat{\omega}_r - \frac{10}{3}|\hat{\omega}|^2 + \frac{5}{3}\hat{\omega}_r\right) + \left(\hat{\omega}_r^2 - \hat{\gamma}^2 - \frac{10}{3}\hat{\omega}_r + \frac{5}{3}\right)\left(\eta_e - \frac{7}{3} + \frac{5}{3}\epsilon_n\right)\right]\right\} =$$
$$= \frac{1}{\hat{N}}\left\{|\hat{\omega}|^2\left[|\hat{\omega}|^2\left(\epsilon_n - 1\right) - 2\hat{\omega}_r\left(\eta_e - \frac{7}{3} + \frac{5}{3}\epsilon_n\right) + \frac{5}{3}\left(2\eta_e - \frac{11}{3} + \frac{7}{3}\epsilon_n\right) +\right.\right.$$
$$\left.\left. +\frac{5}{3\tau}\left(-\eta_e + 1 + \frac{5}{3}\epsilon_n\right)\right] + \frac{50}{9\tau}\left(1-\epsilon_n\right) + \frac{25}{9\tau}\left(\eta_e - \frac{7}{3} + \frac{5}{3}\epsilon_n\right)\right\} \tag{B.77}$$

B.4.1 Transport matrix

We can split the pre-factor of χ_i as given in 3.28 in order to isolate the contributions of the different driving gradients:

$$1 - \frac{2}{3\eta_i} - \left(1-f_t\right)\frac{10}{9\tau}\frac{\epsilon_n}{\eta_i} - \frac{2f_t}{3\eta_i}\frac{1}{\hat{N}}\left\{|\hat{\omega}|^2\left[|\hat{\omega}|^2\left(\epsilon_n - 1\right) + \hat{\omega}_r\left(\frac{14}{3} - 2\eta_e - \frac{10}{3}\epsilon_n\right) +\right.\right.$$
$$\left.\left. +\frac{5}{3}\left(-\frac{11}{3} + 2\eta_e + \frac{7}{3}\epsilon_n\right) - \frac{5}{3\tau}\left(1 + \eta_e - \frac{5}{3}\epsilon_n\right)\right] + \frac{50}{9\tau}\left(1-\epsilon_n\right)\hat{\omega}_r - \frac{25}{9\tau}\left(\frac{7}{3} - \eta_e - \frac{5}{3}\epsilon_n\right)\right\} =$$
$$= 1 - \frac{2}{3\eta_i}\left[1 + \frac{f_t}{\hat{N}}|\hat{\omega}|^2\left(-|\hat{\omega}|^2 + \frac{14}{3}\hat{\omega}_r - \frac{55}{9} - \frac{5}{3\tau}\right) + \frac{f_t}{\hat{N}}\left(\frac{50}{9\tau}\hat{\omega}_r - \frac{175}{27\tau}\right)\right] +$$
$$-\frac{2\epsilon_n}{3\eta_i}\left[\frac{5}{3\tau}\left(1-f_t\right) + \frac{f_t}{\hat{N}}|\hat{\omega}|^2\left(|\hat{\omega}|^2 - \frac{10}{3}\hat{\omega}_r + \frac{35}{9} + \frac{25}{9\tau}\right) + \frac{f_t}{\hat{N}}\left(-\frac{50}{9\tau}\hat{\omega}_r + \frac{125}{27\tau}\right)\right] +$$
$$-\frac{2}{3}\frac{f_t}{\hat{N}}\frac{\eta_e}{\eta_i}\left[|\hat{\omega}|^2\left(-2\hat{\omega}_r + \frac{10}{3} - \frac{5}{3\tau}\right) + \frac{25}{9\tau}\right] =$$

$$
\begin{aligned}
&= 1 + \\
&-\frac{T_i}{\nabla T_i}\frac{\nabla n_i}{n_i}\frac{2}{3}\left[1+\frac{f_t}{\hat{N}}|\hat{\omega}|^2\left(-|\hat{\omega}|^2+\frac{14}{3}\hat{\omega}_r-\frac{55}{9}-\frac{5}{3\tau}\right)+\frac{f_t}{\hat{N}}\frac{1}{\tau}\left(\frac{50}{9}\hat{\omega}_r-\frac{175}{27}\right)\right]+ \\
&+\frac{T_i}{\nabla T_i}\frac{4}{3R}\left[\frac{5}{3\tau}(1-f_t)+\frac{f_t}{\hat{N}}|\hat{\omega}|^2\left(|\hat{\omega}|^2-\frac{10}{3}\hat{\omega}_r+\frac{35}{9}+\frac{25}{9\tau}\right)+\frac{f_t}{\hat{N}}\frac{1}{\tau}\left(-\frac{50}{9}\hat{\omega}_r+\frac{125}{27}\right)\right]+ \\
&-\frac{T_i}{\nabla T_i}\frac{\nabla T_e}{T_e}\frac{2}{3}\frac{f_t}{\hat{N}}\left[|\hat{\omega}|^2\left(-2\hat{\omega}_r+\frac{10}{3}-\frac{5}{3\tau}\right)+\frac{25}{9\tau}\right]
\end{aligned}
\tag{B.78}
$$

We recognise the diffusive contribution, the convective part of the flux driven by ∇n_i, the pinch term and the off-diagonal term proportional to ∇T_e.
We do the same for electron heat transport, reminding equation 3.32:

$$
\begin{aligned}
&1-\frac{2}{3\hat{N}}\left[|\hat{\omega}|^2(-2\hat{\omega}_r+5)-\frac{25}{9}\right]+ \\
&-\frac{T_e}{\nabla T_e}\frac{\nabla n_e}{n_e}\frac{2}{3}\left[1-\frac{|\hat{\omega}|^2}{\hat{N}}\left(-|\hat{\omega}|^2+\frac{14}{3}\hat{\omega}_r-\frac{40}{9}\right)+\frac{1}{\hat{N}}\left(-\frac{50}{9}\hat{\omega}_r+\frac{175}{27}\right)\right]+ \\
&+\frac{T_e}{\nabla T_e}\frac{4}{3R}\frac{1}{\hat{N}}\left[|\hat{\omega}|^2\left(|\hat{\omega}|^2-\frac{10}{3}\hat{\omega}_r+\frac{10}{9}\right)+\frac{50}{9}\hat{\omega}_r-\frac{125}{27}\right]
\end{aligned}
\tag{B.79}
$$

There is a diffusive contribution, a convective flux driven by ∇n_e and a pinch term; no contribution comes from ∇T_i.
The particle transport is also built up of several contributions. From equation 3.36:

$$
\begin{aligned}
&|\hat{\omega}|^2(\epsilon_n-1)+\hat{\omega}_r\left(\frac{14}{3}-2\eta_e-\frac{10}{3}\epsilon_n\right)+\frac{5}{3}\left(-\frac{11}{3}+2\eta_e+\frac{7}{3}\epsilon_n\right)= \\
&=-|\hat{\omega}|^2+\frac{14}{3}\hat{\omega}_r-\frac{55}{9}+ \\
&-\frac{n_e}{\nabla n_e}\frac{2}{R}\left(|\hat{\omega}|^2-\frac{10}{3}\hat{\omega}_r+\frac{35}{9}\right)+ \\
&+\frac{\nabla T_e}{T_e}\frac{n_e}{\nabla n_e}\left(-2\hat{\omega}_r+\frac{10}{3}\right)
\end{aligned}
\tag{B.80}
$$

If we write the transport equations for particles and heat fluxes in the matrix form 3.37, equations B.78, B.79 and B.80 immediately lead to the transport coefficients 3.38, 3.39 and 3.40.